공학박사 학위논문

Understanding the Twinning Behavior and Deformation Mechanisms of Mg Single Crystals during Erichsen Test Using Crystal Plasticity FEM

CPFEM을 이용한 에릭슨 시험 시 마그네슘 단결정의 쌍정 거동 및 변형 기구의 이해

2018년 2월

서울대학교 대학원

재료공학부

玄 哲 昇

Understanding the Twinning Behavior and Deformation Mechanisms of Mg Single Crystals during Erichsen Test Using Crystal Plasticity FEM

지도 교수 신 광 선

이 논문을 공학박사 학위논문으로 제출함

2018년 2월

서울대학교 대학원

재료공학부

玄 哲 昇

玄 哲 昇의 박사 학위논문을 인준함

2018년 2월

위 원 장	한 흥 남	(인)
부위원장	신 광 선	(인)
위 원	김 낙 준	(인)
위 원	최 시 훈	(인)
위 원	이 경 훈	(인)

Abstract

Understanding the Twinning Behavior and Deformation Mechanisms of Mg Single Crystals during Erichsen Test Using Crystal Plasticity FEM

Cheol-Seung Hyun
School of Materials Science and Engineering
The Graduate School
Seoul National University

Magnesium (Mg) alloys with a density of 1.74 g/cm^3 are the lightweight structural materials and their superior mechanical properties make Mg alloys more attractive for various applications. Mg alloys have become the key materials especially in the automotive industry for improvement in the fuel efficiency due to their low density, excellent specific strength and stiffness, exceptional dimensional stability and high damping capacity.

In recent years, the cast Mg alloys have widely been used to produce the majority of Mg alloy products. However, the cast Mg alloys fail to meet most of the current requirements and the wrought Mg alloys showing both better strength and toughness are newly expected to be utilized. However, there are still several technical issues to achieve high performance of wrought Mg alloys. Mg usually develops strong basal texture during plastic deformation, resulting in anisotropic mechanical properties and poor formability. Additionally, fundamental observations such as orientation

dependency on the slip and twinning modes as well as interactions between deformation modes are still rarely reported.

Thus, in the present study, the twinning behavior and deformation mechanisms of pure Mg single crystals were investigated via Erichsen test at room temperature (RT). In order to establish the unique twinning behaviors according to the position of a deformed specimen, microtexture analyses were performed on two cross-sections of a deformed specimen via the electron backscatter diffraction (EBSD) technique. The EBSD results revealed that thin twin bands with different types of twin variants were developed throughout the deformed specimen. The crystal plasticity finite element method (CPFEM), in relation to both the crystallographic slip and deformation twinning, was used to explain the heterogeneous evolution of the twin bands throughout the deformed specimen during Erichsen test at RT. CPFEM results such as strain components, relative activity of deformation modes, and accumulated volume fraction of twin variants can effectively explain the experimentally observed heterogeneity of the twin bands.

Keywords: Single crystal, Erichsen test, Crystal plasticity, Magnesium, Twin band

Student Number: 2008-20698

Contents

List of Tables

List of Figures

Chapter 1. Introduction

1.1 Deformation modes in Mg

1.1.1 Slip modes

Figure 1.1 illustrated slip systems in Mg. The colored surfaces represent each slip planes and the arrows indicate slip direction Burgers vectors. It is known that five independent slips are necessary for homogeneous plastic deformation in a material which is called the von Mises criterion. In Mg, the (0002) basal slip which has only two independent slip systems is preferentially operative because the CRSS for basal slip is much lower than those for non-basal slips at room temperature. The activation of $\langle \boldsymbol{c}+\boldsymbol{a} \rangle$ Burgers vector rarely occurs at room temperature, therefore, it is important to activate pyramidal slips during plastic deformation. One possible source mechanism for $\langle \boldsymbol{c}+\boldsymbol{a} \rangle$ dislocations of a pyramidal slip system is introduced in Figure 1.2 [1]. Figure 1.2(a) shows the cross slip of $\langle \boldsymbol{a} \rangle$ dislocation from the basal plane to a $(1\bar{1}00)$ prismatic plane. Figure 1.2(b) illustrates a $\langle \boldsymbol{c}+\boldsymbol{a} \rangle$ dislocation junction, along its near-screw orientation, formed when an active prismatic slip dislocation interacts with a sessile $\langle \boldsymbol{c} \rangle$ dislocation. Here, $\langle \boldsymbol{c} \rangle$ dislocations are assumed to exist in the grain matrix as a part of the initial microstructure. The subsequent cross slip of the $\langle \boldsymbol{c}+\boldsymbol{a} \rangle$ screw dislocation from the $(1\bar{1}00)$ prismatic plane to the $(11\bar{2}2)$ pyramidal plane is depicted in Figure 1.2(c).

Table 1.1 summarizes the vector energies for the possible dislocation types in Mg. The basal slip was observed to be the prevalent deformation

mode as it was found to be uniformly distributed all over the crystal surface in case of Mg single crystal. Traces of slip on the prismatic planes have been observed only in parts of the grain which may have been subjected to higher stresses such as near corners [2]. Since the basal slip has the lowest CRSS value, some works have performed tensile tests with a basal plane parallel with the loading direction. This orientation is favorable for the non-basal slip and suppressed the basal slip based upon geometric conditions. The results showed the prismatic $\langle \boldsymbol{a} \rangle$ glide to be the deformation mode at room temperature in these conditions with [10 $\bar{1}$ 1]. Plastic deformation characteristics of Mg and Mg-Li single crystals deformed in the hard orientation were reported by Stohr and Poirier, Obara, and Ando et al. [3–5]. The information obtained from these investigations was the stress-strain curves, slip-trace and slip-step height analyses on the surface, and post-mortem transmission electron microscopy (TEM) characterization of dislocation structures. A possible source mechanism for the non-basal $\langle \boldsymbol{c}+\boldsymbol{a} \rangle$ slip dislocations is proposed by M.H. Yoo based on the formation of an attractive junction between glissile $\langle \boldsymbol{a} \rangle$ and sessile $\langle \boldsymbol{c} \rangle$ dislocations from the prismatic plane into a pyramidal plane [1].

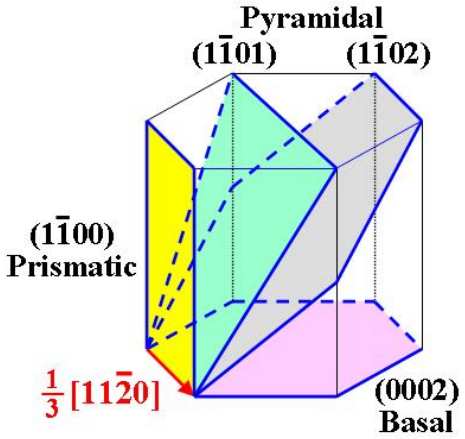

(a)

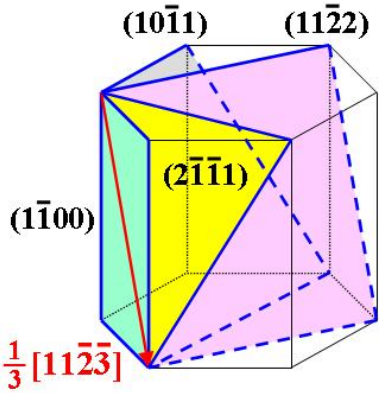

(b)

Figure 1.1 Slip systems in Mg; (a) basal, prismatic and pyramidal slip systems with $\langle \boldsymbol{a} \rangle$ Burgers vector and (b) four possible pyramidal slip systems with $\langle \boldsymbol{c}+\boldsymbol{a} \rangle$ Burgers vector.

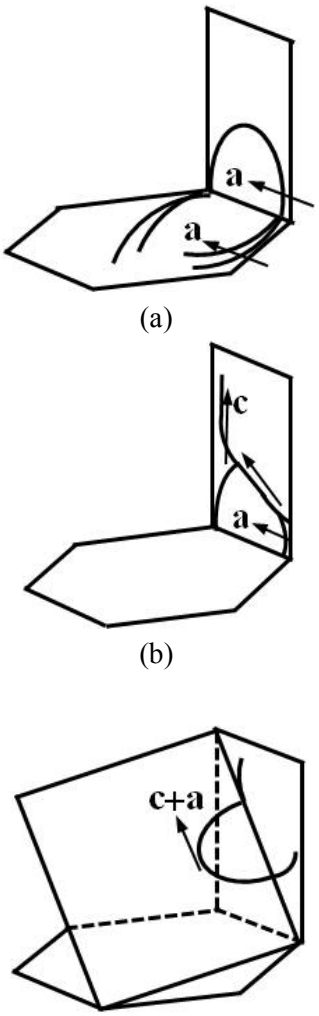

Figure 1.2 Evolution of the dislocation source for a $\langle \boldsymbol{c}+\boldsymbol{a} \rangle$ pyramidal slip system; (a) cross slip of $\langle \boldsymbol{a} \rangle$ dislocation, (b) formation of $\langle \boldsymbol{c}+\boldsymbol{a} \rangle$ dislocation junction and (c) cross slip of $\langle \boldsymbol{c}+\boldsymbol{a} \rangle$ dislocation [1].

Table 1.1 Possible dislocation types in Mg.

Type of dislocations	Number of systems	Burgers vector	Slip system	
a	3 (2)	1/3<11$\bar{2}$0>	Basal	{0001}<11$\bar{2}$0>
	3 (2)		Prism-I	{10$\bar{1}$0}<11$\bar{2}$0>
	6 (4)		Pyramidal-I	{10$\bar{1}$1}<11$\bar{2}$0>
c	3 (2)	<0001>	Prism-I	{10$\bar{1}$0}<0001>
	3 (2)		Prism-II	{11$\bar{2}$0}<0001>
$c+a$	3 (2)	1/3<11$\bar{2}$3>	Pyramidal-II	{11$\bar{2}$2}<11$\bar{2}$3>

1.1.2 Twinning modes

Figure 1.3 shows variation of twinning shear with c/a ratio in HCP metals [6]. A filled symbol indicates that the twin mode is an active mode. In the crystallographic point of view, the twinned lattice is oriented to a mirror image of the untwined lattice. The invariant plane of this shear is called K_1 and the shear direction η_1; the second undistorted plane is K_2, the plane containing η_1 and the normal to K_1 and K_2 is the plane of shear. In addition, a positive slope represents contraction along the c-axis, while a negative slope represents extension. Since c/a ratio of Mg is less than $\sqrt{3}$, the $\{10\bar{1}2\}$ tensile twining is formed by extending the crystal along the c-axis, while the $\{10\bar{1}1\}$ compressive twinning is formed by shortening the crystal along c-axis.

Twinning is usually employed to explain deformation with c components and frequently occurs to support limited possible slip modes in HCP metals. Mg has the limited number of independent slip systems; a minimum of five independent slip modes is required for an arbitrary shape change, and twinning modes play an important role in plastic deformation since twinning can accommodate c-axis strain. Therefore, slip and twinning are competitive and interdependent deformation modes especially at low temperature.

Table 1.2 summarizes twin type and the corresponding misorientation angles/axis in Mg. Among the various types of twins, the $\{10\bar{1}2\}$ tensile twin and $\{10\bar{1}1\}$ compressive twin modes are mostly observed in Mg. Figure 1.4 shows unit cells with the base vectors η_1 and η_2 for the $\{10\bar{1}2\}$ tensile twin and $\{10\bar{1}1\}$ compressive twin modes. d is the interspacing of the twin habit planes K_1, $\emptyset$ is the acute angle between η_1 and η_2, e is a numerical factors, and q is the number of K_1 lattice planes intersected by η_2. It was reported that

the $\{10\bar{1}2\}$ tensile twining only requires the CRSS value of 2 ~ 3 MPa, while the $\{10\bar{1}1\}$ compressive twinning requires the much larger CRSS value in the range of 70 ~ 140 MPa [7]. Reed–Hill and Robertson reported the onset of twinning at a tensile stress of 4 MPa, which corresponds to the resolved shear stress of 2 MPa, i.e. reversal of the η_1 direction will not produce a twin [8]. This means that for a single crystal of given orientation with respect to a uni-axially applied stress, some variants of particular twin mode should operate only in tension, whereas others should operate only in compression. It is generally known that the $\{10\bar{1}2\}$ tensile twin is most commonly observed in Mg and easily activated by compression direction perpendicular to, or tension parallel to the c-axis from the geometric reason, as shown in Figure 1.5 [9]. In the opposite case, when contraction along the c-axis is accommodated by the formation of contraction twins on the $\{10\bar{1}1\}$ planes, the basal planes are reoriented by 56° around a $<11\bar{2}0>$ axis.

The most important feature of $\{10\bar{1}2\}$ tensile twinning is that it gives rise to a crystallographic lattice rotation of 86.3° in twinned regions. This leads to a change in the microstructural characteristics of the material, such as texture and grain size (twins and residual parent grains coexist in an original grain), and finally influences the deformation behavior by affecting the activities of various slip and twinning modes. The influence of $\{10\bar{1}2\}$ tensile twinning on the deformation can be understood by following three main mechanisms [10]: (1) the twin boundaries that have formed can act as barriers to dislocation motion, as do grain boundaries, leading to an increase in the work-hardening rate (i.e.,Hall-Petch hardening). In addition, they transform glissile dislocations into sessile dislocations within the twin interiors, and thus contribute to strengthening via the Basinski mechanism (i.e., the trapping of sessile dislocations inside twins); (2) the accommodation of strain along the c-

axis can give rise to a decrease of work hardening rate; (3) the crystallographic lattice reorientation in twinned regions, caused by $\{10\bar{1}2\}$ tensile twinning, can enhance or weaken the activities of slip systems by affecting their Schmid factor.

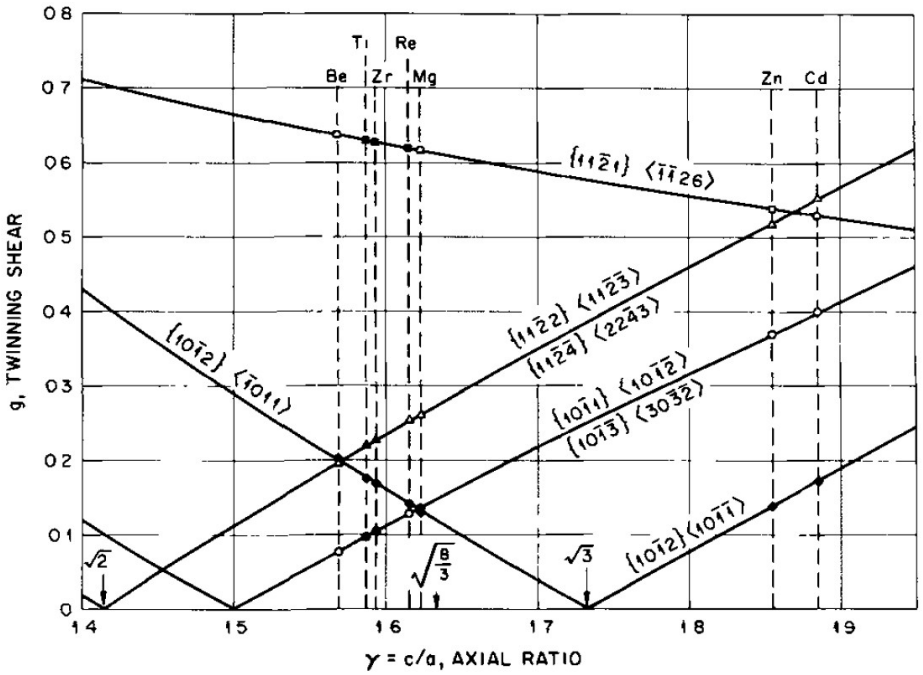

Figure 1.3 Variation of twinning shear with the c/a ratio in HCP metals [6].

Table 1.2 Twin type and the corresponding misorientation angle/axis in Mg.

Twin type	Misorientation angle/axis
$\{10\bar{1}1\}$	56.2° $<1\bar{2}10>$
$\{10\bar{1}2\}$	86.3° $<1\bar{2}10>$
$\{10\bar{1}3\}$	64.0° $<1\bar{2}10>$
$\{10\bar{1}5\}$	41.0° $<1\bar{2}10>$
$\{30\bar{3}2\}$	39.2° $<1\bar{2}10>$
$\{30\bar{3}4\}$	70.8° $<1\bar{2}10>$
$\{10\bar{1}1\}$-$\{10\bar{1}2\}$	37.5° $<1\bar{2}10>$
$\{10\bar{1}1\}$-$\{10\bar{1}2\}$	30.1° $<1\bar{2}10>$
$\{10\bar{1}1\}$-$\{10\bar{1}2\}$	66.5° $<5\bar{9}43>$
$\{10\bar{1}1\}$-$\{10\bar{1}2\}$	69.9° $<2\bar{4}21>$
$\{10\bar{1}2\}$-$\{10\bar{1}2\}$	7.40° $<1\bar{2}10>$
$\{10\bar{1}2\}$-$\{10\bar{1}2\}$	60.0° $<10\bar{1}0>$[a]
$\{10\bar{1}2\}$-$\{10\bar{1}2\}$	60.4° $<\bar{8}170>$[b]
$\{10\bar{1}3\}$-$\{10\bar{1}2\}$	22.2° $<1\bar{2}10>$

[a]Actual axis is 3.7° off $<10\bar{1}0>$

[b]Actual axis is 3.7° off $<\bar{8}170>$

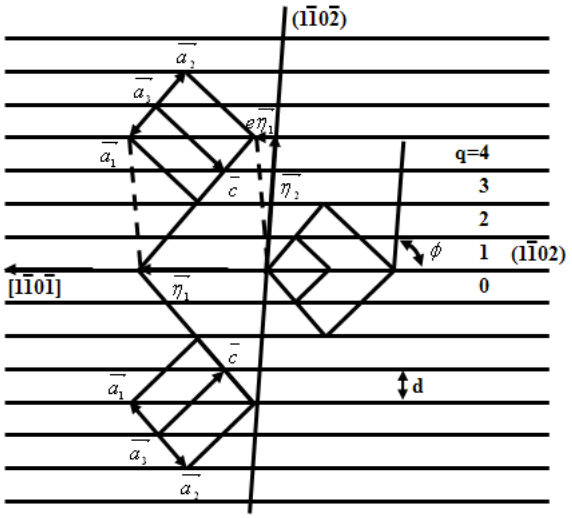

K1=(1$\bar{1}$02) $\overline{\eta_1}$ =[1$\bar{1}$0$\bar{1}$]

K1=(1$\bar{1}$0$\bar{2}$) $\overline{\eta_2}$ =[$\bar{1}$10$\bar{1}$]

(a)

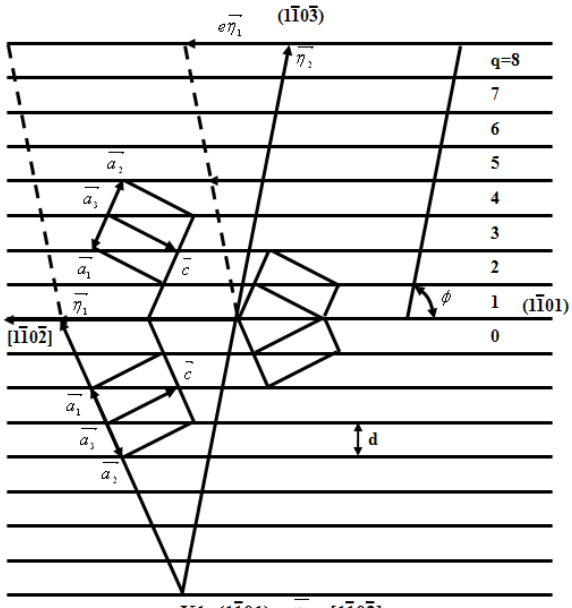

K1=(1$\bar{1}$01) $\overline{\eta_1}$ =[1$\bar{1}$0$\bar{2}$]

K1=(1$\bar{1}$03) $\overline{\eta_2}$ =[$\bar{3}$30$\bar{2}$]

(b)

Figure 1.4 Crystallographic relations of (a) {10$\bar{1}$2} tensile twin and (b) {10$\bar{1}$1} compressive twin modes in HCP structure.

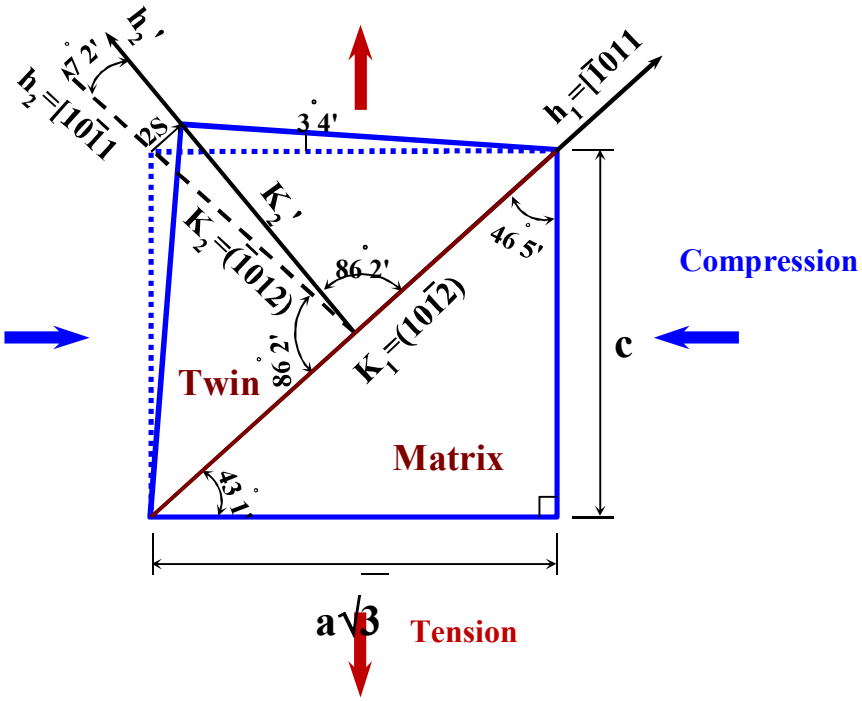

Figure 1.5 Shape changes produced by {10$\bar{1}$2} tensile twin in Mg [9].

1.2 Motivation

Magnesium (Mg) is a promising structural materials that is particularly applicable to the automobile industry because it reduces CO_2 emissions by improving fuel efficiency [11–16]. Despite its high specific strength and stiffness, however, the formability in Mg is quite low among lightweight commercially available candidates due to a crystallographic anisotropy induced by a hexagonal close packed (HCP) structure [13,17,18]. Wrought Mg and its alloys generally exhibit a strong basal texture caused by a limited number of deformation modes. Therefore, the mechanical properties of these materials show strong anisotropic characteristics, which results in poor formability, particularly at room temperature (RT) [11,14,15,18–25].

In recent years, considerable effort has been extended in the development of new Mg alloys with better stretch formability at RT via control of the strong basal texture. Unique plastic deformation processes such as equal channel angular rolling, asymmetric rolling, and high temperature rolling are known to weaken the basal texture effectively [19,21,23,25–27]. Alloy design is also regarded as an alternative method to essentially improve formability at RT via the addition of alloying elements such as rear earth and Ca, which substantially contributed to reducing the basal texture intensity [14–16,20,22,24,25,28–31].

The critical resolved shear stresses (CRSSs) of prismatic and pyramidal slips in Mg are known to decrease with increasing the temperature because non-basal slip modes are more easily activated at elevated temperatures [11,12,19,32,33]. This suggests that because the main deformation modes that occur at elevated temperature different from those that occur at RT, and, therefore, a systematic examination on the deformation mechanism of

deformation modes that occur at RT is needed to improve the RT formability. Basically, the ideally randomized texture of Mg is expected to activate basal slip in all the possible directions, which indicates that significantly enhanced stretch formability at RT can be achieved only by activating the basal slip. Due to their low CRSS values, basal slip and $\{10\bar{1}2\}$ tensile twin (TTW) play important roles in plastic deformation at RT [15,17,28,32,34], and various methods have recently been investigated to create a more favorable texture for the activation of basal slip and/or TTW in order to enhance the stretch formability at RT. In other words, the development of a texture favorable for the crystallographic reorientation by TTW under a biaxial stress state would then allow the activation of additional basal slip in various directions [13,20,35]. Macroscopic twinning events have accommodated significant levels of strain, whereby the twinned areas were reoriented into soft orientations amenable to basal slip. In terms of formability, one very important characteristic of deformation twinning is that grains unfavorably oriented for basal slip can be reoriented into a more favorable position.

Pioneering researches performed almost 60 years ago on Mg single crystal failed to give a clear explanation of the operating slip and twinning mechanisms. Studies employing single crystals continue to be a valuable asset in uncovering the underlying mechanisms of deformation. Based on the Schmid factor criterion, the orientation condition with a c-axis inclined at 45° to the loading direction (LD) under uniaxial tension/compression is known to be favorable for the basal slip activation [11–14,19,20,31]. Figure 1.6 shows the effect of strain path on twinning behavior for Mg single crystal in plane strain compression at RT [36–38]. Molodov *et al*. [36–40] recently conducted plane strain compression (PSC) tests on Mg single crystals with various initial crystallographic orientations. They reported that Mg single crystal with a 45°

orientation relationship between LD and c-axis exhibited the enhanced ductility at RT that could be enhanced by as much as 100 % without failure, which was attributed to anomalous TTW combined with basal slip. Specimens with the c-axis aligned at an angle of 45° with respect to the compression direction were favorably orientated for basal slip and initially were deformed at a very low levels of flow stress. In addition to operating the deformation mode by dislocation slip, anomalous TTW is activated as an auxiliary deformation mode to compensate for deformation heterogeneity. That result suggests that although the initial crystallographic orientation is geometrically unfavorable for activating TTW, the anomalous TTW could occur throughout a deformed specimen. Therefore, it is expected that an initial texture with a 45° orientation relationship between LD and c-axis can improve the stretch formability at RT.

Formability evaluation methodologies of Mg sheet alloys include the Erichsen test, the V-bending test [18,41–44], and the forming limit diagram (FLD) [45–50]. The stress states in an Erichsen test differ across an entire dome, from the center to the edge as well as through the thickness direction [16,20]. In other words, the heterogeneous stress states are applied throughout the specimen, meaning that a hard orientation along one direction, e.g., in the transverse direction, could be soft in another direction, e.g., in the longitudinal direction. In the Erichsen test, the deformation behavior of Mg single crystals, including twinning, is expected to be much different from that of in-plane tension/compression and it is impossible to explain using the existing Schmid factor criterion because the stress (or strain) state is very uneven depending on the position of the specimen.

Figure 1.7 shows the theoretical study of Erichsen test on Mg poly crystal at RT. To date, no detailed experiments or theoretical studies have

been focused on the deformation behavior of Mg single crystals during an Erichsen test. Single crystal study could provide a valuable insight into the fundamental mechanisms of the stretch formability that is induced by a strong anisotropic nature. On the other hand, the crystal plasticity finite element method (CPFEM) was developed to simulate heterogeneous plastic deformation of HCP polycrystalline materials [18]. CPFEM is well suited to the theoretical modeling of processes that undergo uneven deformation throughout single crystal specimens such as those observed during an Erichsen test.

Thus, the present work was a combination study of single crystal experimentation and plasticity modeling to examine the twinning behavior and deformation mechanisms occurring in Mg single crystal during an Erichsen test at RT. EBSD technique combined with TTW traces was used to examine the twinning behavior throughout a deformed Mg single crystal. CPFEM was conducted to simulate the spatial distribution of strain components, the relative activities of deformation modes, and the twin behaviors developed in a deformed Mg single crystal during an Erichsen test at RT.

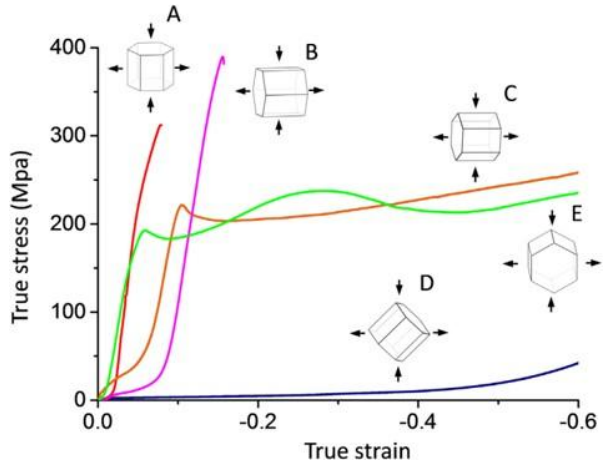

(a)

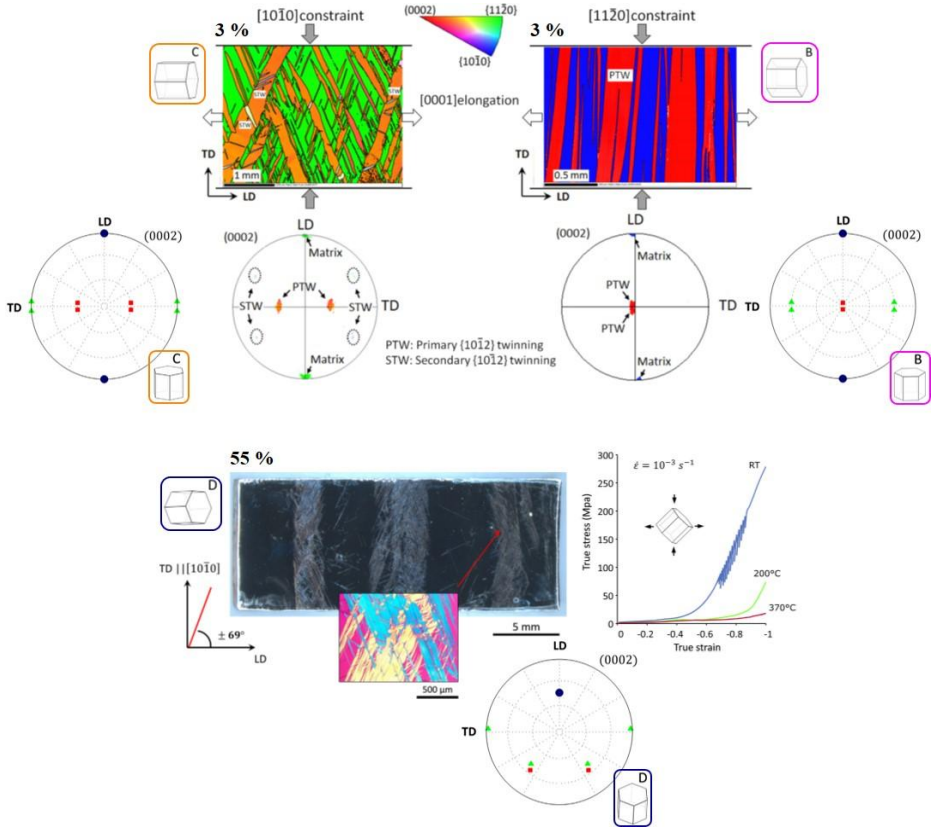

(b)

Figure 1.6 Effect of strain path on twinning behavior for Mg single crystal in plane strain compression at RT [36–38].

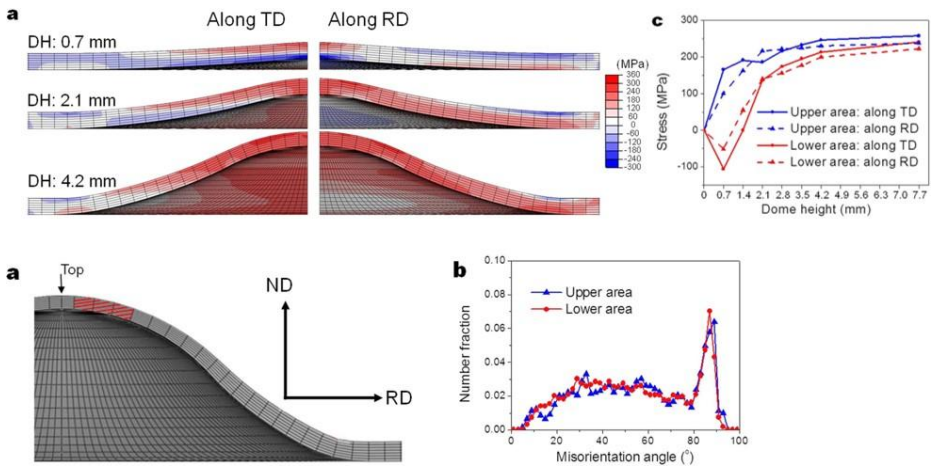

Figure 1.7 Theoretical study of Erichsen test on Mg poly crystal at RT [20].

Chapter 2. Experimental procedure

2.1 Characterization of Mg single crystal

A pure Mg ingot (> 99.95 wt.% purity) was melted into a graphite mold, and the crystal growth progressed at the speed of 2.1 mm/hr under the protection of argon gas. A single crystal of pure Mg with a diameter of 58 mm was successfully grown via the vertical Bridgman method, as shown in Figure 2.1. As far as we could ascertain, this could have been the world-largest pure Mg single crystal. Figure 2.2 shows the pattern acquisition and indexing of a pure Mg single crystal. The crystallographic orientation of the as-grown single crystal was determined via Laue back reflection method. A 1 mm-thick sheet with the desired crystallographic orientation was cut from the as-grown single crystal using electric discharge machining (EDM) and was mechanically polished with sand papers up to # 2000. The crystallographic orientation of the cut sheet was determined via Laue back reflection to confirm the correct orientation for subsequent processes.

Prior to Erichsen test, the initial crystallographic orientation of the undeformed Mg single crystal is defined based on the global coordinate system (GCS) of X-Y-Z, with the Z-axis parallel to the punching direction (PD) during the Erichsen test. The strain components of the deformed specimens obtained from the CPFEM results are expressed based on the local sample coordinate system (LSCS) of x-y-z.

An Erichsen test was carried out with a punch speed of 5 mm/min at RT, as depicted in Figure 2.3. The diameter of the hemispherical punch was

20 mm, and silicone lubricant was used. The Erichsen test was conducted until a fracture occurred. The depth in mm of a punch required to obtain a fracture is defined generally as the Erichsen index (IE).

EBSD analysis was performed on cross-sections of Y-Z and X-Z to systematically investigate the behavior of deformation twins that occurs in the deformed Mg single crystal during an Erichsen test. The deformed specimens were cut carefully using EDM in the X and Y directions to inhibit the generation of additional deformation twins at the time of cutting. At a steady state, the EDM speed was about 3.5 mm/min. The microtextures of the Y-Z and X-Z half-sections were examined via EBSD using a SU70 (FE-SEM, HITACHI) fitted with a TSL EBSD camera operated at 15 kV (Figure 2.4). An automated EBSD scan was obtained in the stage-control mode using TSL data acquisition software at a step size of 2.5 μm, and the data with a confidence index > 0.1 were used for the texture analysis.

Bridgman method

Pure Mg single crystal

150 mm (L) × 58 mm (Dia.)

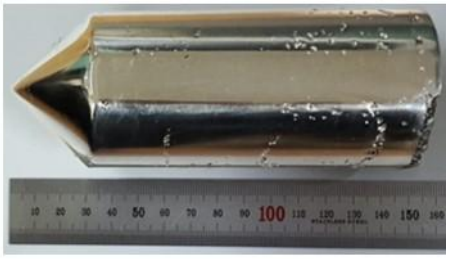

Experimental condition:
Furnace temperature, speed,
Ar atmosphere, water supply, etc.

Figure 2.1 Single crystal growth.

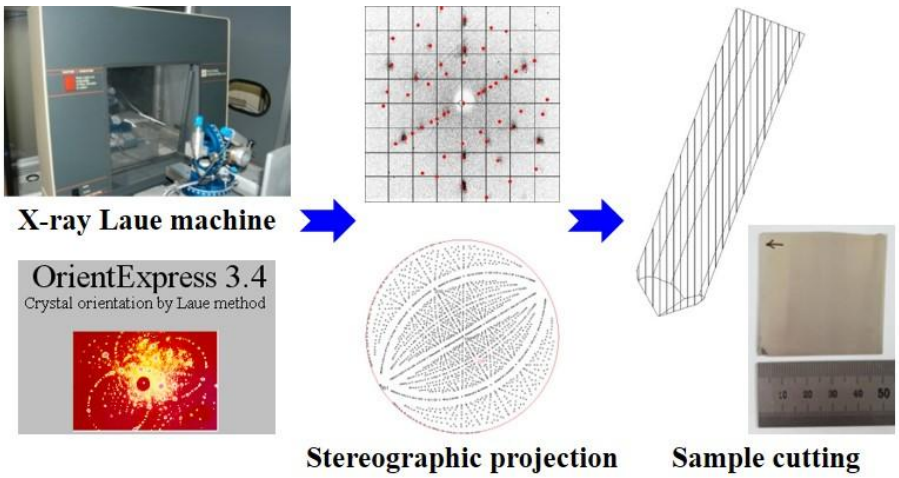

Figure 2.2 Pattern acquisition and indexing of a pure Mg single crystal.

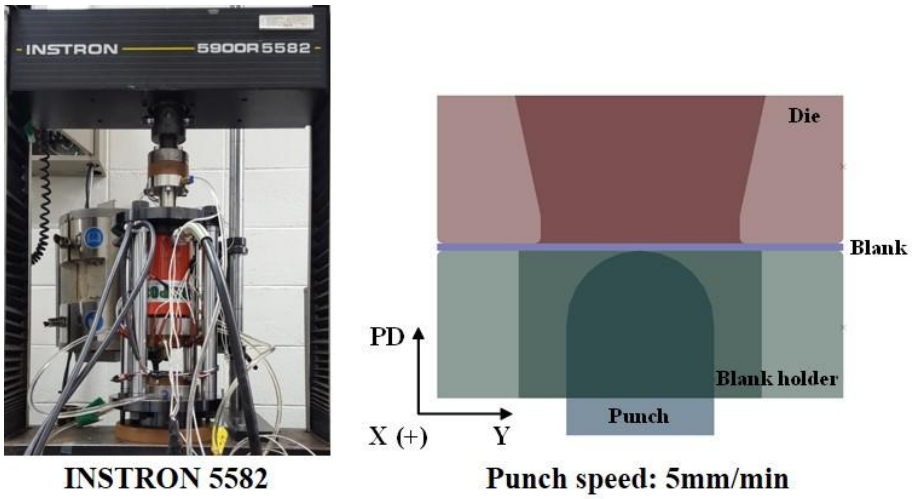

Figure 2.3 Erichsen test of a pure Mg single crystal.

Figure 2.4 Texture measurement after Erichsen test.

2.2 Simulation

In this study, the micromechanical behaviors of Mg single crystal were simulated using the crystal plasticity finite element method (CPFEM). In this section, a brief description of CPFEM is given. For a detailed description, readers are referred to previous papers [51–53]. For materials with hexagonal crystal symmetry, five independent elastic constants for pure Mg were used in the present work:

$$C_{11} = 58 \text{ GPa}, C_{12} = 25 \text{ GPa}, C_{13} = 20.8 \text{ GPa},$$
$$C_{33} = 61.2 \text{ GPa}, C_{55} = 16.6 \text{ GPa}.$$

For rate-dependent materials, the shear rates were given explicitly in terms of the resolved shear stress on the active slip/twin systems and the resistance of the active slip/twin systems to shear. For these simulations, the relationship is given by the following:

$$\dot{\gamma}^{\alpha} = \dot{\gamma}_0^{\alpha} \left| \frac{\tau^{\alpha}}{\tau_0^{\alpha}} \right|^{1/m} \text{sign}(\tau^{\alpha}) \quad ---------- (1)$$

Self- and latent-hardening are readily accounted for by a suitable evolution of the reference τ_0^{α} values in the constitutive law expressed by Eq. (1). The present work employed a microscopic hardening law [54,55] for this purpose, as follows:

$$\dot{\tau}_0^{\alpha} = \sum_{\beta}^{n} H^{\alpha\beta} \left| \dot{\gamma}^{\beta} \right| \ \alpha, \beta = 1 \ldots n \quad H^{\alpha\beta} = q^{\alpha\beta} h_0 \left(1 - \frac{\tau_0^{\alpha}}{\tau_{\text{sat}}} \right)^{a} \quad --- (2)$$

where $H^{\alpha\beta}$ is a hardening matrix that was introduced to account for the interaction between the slip and twin systems, and $q^{\alpha\beta}$ accounts for the hardening rate of the slip/twin system, α, due to the slip/twin activity of the system, β. Here, it was assumed that the self-hardening term (diagonal term

of $q^{\alpha\beta}$) equaled the latent-hardening term (off-diagonal term of $q^{\alpha\beta}$) i.e., ($q^{\alpha\beta} = 1$). The fitting simulation was performed by varying the CRSS value (τ_0) and the microscopic hardening parameters ($\tau_{\text{sat}}, h_0, a$). In this study, four slip systems and one twin system were considered: basal $\langle \boldsymbol{a} \rangle$ slip ($\{0001\}\langle 11\bar{2}0\rangle$); prismatic $\langle \boldsymbol{a} \rangle$ slip ($\{1\bar{1}00\}\langle 11\bar{2}0\rangle$); pyramidal $\langle \boldsymbol{a} \rangle$ slip ($\{1\bar{1}01\}\langle 11\bar{2}0\rangle$) and pyramidal $\langle \boldsymbol{c}+\boldsymbol{a} \rangle$ slip ($\{11\bar{2}\bar{2}\}\langle 11\bar{2}3\rangle$); and, TTW ($\{10\bar{1}2\}\langle 10\bar{1}\bar{1}\rangle$)). Six variants of TTW were considered as follows: TT1— $(10\bar{1}2)[\bar{1}011]$, TT2 — $(01\bar{1}2)[0\bar{1}11]$, TT3 — $(\bar{1}102)[1\bar{1}01]$, TT4 — $(\bar{1}012)[10\bar{1}1]$, TT5— $(0\bar{1}12)[01\bar{1}1]$, and TT6— $(1\bar{1}02)[\bar{1}101]$.

The relative contribution of deformation modes as a function of true strain provided information that was useful in the analysis of plastic deformation. The relative activity (R.A.$^{\alpha}$) of each deformation mode, α, among slip/twin systems ($N = N_s + N_t$), was determined by the summation of shear strain in the elements (e), as follows:

$$\text{R.A.}^{\alpha,e} = \frac{\gamma^{\alpha,e}}{\sum_{\beta=1}^{N} \gamma^{\beta,e}} \quad (3)$$

To consider the effect of deformation twinning on the evolution of macroscopic flow curves under in-plane tension and compression, the original predominant twin reorientation (PTR) scheme [56] was modified and implemented in the CPFEM. This required tracking of both the shear strain, $\gamma^{tw,e}$, contributed by each twin system, tw, and the associated volume fraction $V^{tw,e} = \gamma^{tw,e}/S^{tw}$ ($S^{tw}_{ten.}$= 0.129 is the characteristic twin shear) within each element, e. By summation of all twin systems in each element, the accumulated twin fraction, V^{acc}, in each orientation was determined, as follows:

$$V^{acc} = \int_o^t \left(\frac{\sum_{tw} \dot{\gamma}^{tw,e}}{S^{tw}} \right) dt \quad ---------- (5)$$

At each incremental step, the fractions accumulated in the individual twinning systems of each orientation were compared against a threshold fraction, V^{th}, defined as follows:

$$V^{th} = C^{th1} + C^{th2}.V^{acc} \quad ---------- (6)$$

After each deformation increment, the twin system with the highest accumulated volume fraction was identified. If the total accumulated volume fraction was greater than the threshold fraction, V^{th}, the orientation was allowed to reorient. The threshold fraction, V^{th}, increased gradually and further reorientation by twinning was inhibited by large deformations. The algorithm prevented reorientation by twinning until a threshold value, which was mostly determined by C^{th1}, was attained. The threshold value, C^{th2}, determined the evolution of the twin volume fraction during plastic deformation. To consider the effect of microstructure heterogeneities on twinning, however, we additionally employed a random constant (R) in the twin nucleation (C^{th1}) and twin propagation (C^{th2}) parameters, as shown in Table 2.1.

In the present work, the fitting simulation was carried out using the hardening parameters and twinning parameters until consistency was reached between the two stress-strain curves from the uniaxial loading testing and simulation. To predict the deformation behavior of a Mg single crystal, a simple 3-D mesh (20 × 20 × 10 = 4000 elements) was used. More detailed fitting methods have been covered in detail in previously published papers [52,53]. The set of fitted microscopic hardening parameters for a Mg single crystal are listed in Table 2.1.

We only considered the PTR scheme to determine the microscopic

hardening parameters of the deformation modes in a Mg single crystal. However, since the nucleation and growth of twins during the deformation of a Mg single crystal is sensitive to the surface conditions, CPFEM based on the PTR scheme has limitations in simulating the nucleation and growth of accurate twin bands (TBs). In the present study, V^{acc} was considered as a driving force for twinning at the grain level instead of directly simulating the nucleation and growth of thin TBs occurring in the deformed matrix during the Erichsen test.

Figure 2.5 shows the initial mesh and boundary conditions used in the finite element analysis (FEA) for the Erichsen test. Due to the triclinic sample symmetry, an entire blank was used to simulate the Erichsen process. The Erichsen simulation based on CPFEM was performed using 65,844 elements with 3-dimensional 8-node brick elements referred to as C3D8R. The friction coefficient between the blank and the tools was prescribed as $\mu = 0.05$.

Table 2.1 Microscopic hardening parameters used in the CPFEM simulation.

Material	Mode	τ_0	h_0	τ_{sat}	a	Latent hardening
Pure Mg	Basal $\langle a \rangle$	1	40	5	1.1	4
	Pyramidal $\langle a \rangle$	52	175	200	0.8	
	Prismatic $\langle a \rangle$	52	175	200	0.8	
	Pyramidal $\langle c + a \rangle$	55	183	300	0.8	
	Tensile twin	2	25	10	1.1	

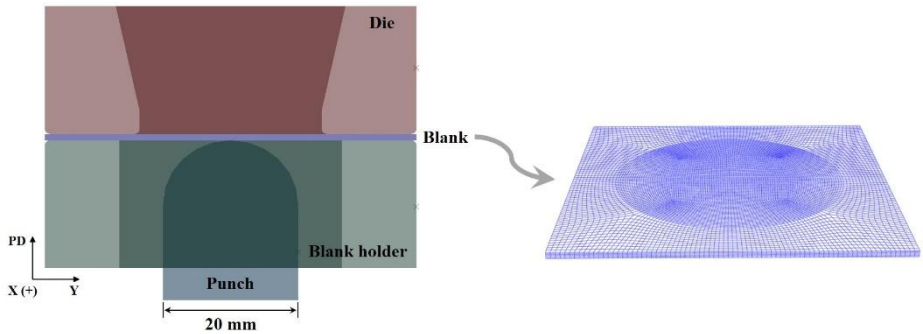

Figure 2.5 Initial mesh and boundary conditions used in the finite element analysis (FEA) for the Erichsen test.

Chapter 3. Effect of strain path on twinning behavior in Mg single crystal during Erichsen test

3.1 Results and discussion (Orientation A)

3.1.1. Erichsen test simulation using CPFEM

In the case of the Erichsen test, the specimen is subjected to a non-uniform deformation history in the plane and thickness directions of the specimen. Furthermore, since the anisotropy of single crystal specimens is so strong, the non-uniformity of deformation in a deformed specimen becomes much more intense, which necessitates an understanding of the non-uniformity of deformation using simulation techniques such as CPFEM. When the PD is parallel to the [777 0 $\overline{777}$ 829] direction, the initial crystallographic orientation of a Mg single crystal during the Erichsen test has the orientation relationship of 45° between PD and c-axis, which can be expressed as (ϕ_1, Φ, ϕ_2) = (90°, 45°, 60°) in Euler space, as described in Figure 3.1(a). The results of the Erichsen test at RT in Figure 3.1(b) show that plastic anisotropy induced an asymmetrically deformed dome shape with respect to the center of both the top and bottom of the deformed specimen. As a consequence, fracture occurred near the dome center parallel to the X-axis under a punch stroke with an IE of 2.5 mm. Furthermore, in order to systematically investigate the twinning behavior and deformation mechanisms during the Erichsen test, the deformed specimen was equally divided into three distinct regions ($L_A = L_B = L_C$). The three distinct regions are defined as follows. Region A (RA) is the area near the center of the deformed specimen,

and is the point at which severe biaxial strain (or stress) occurs during an Erichsen test. Region B (RB) is the intermediate area between the center and the circumference of the deformed specimen. Region C (RC) is the area of the circumference of the deformed specimen, and it the point at which an upper die imposes normal pressure during an Erichsen test.

CPFEM simulation can identify the spatial distribution of strain components, the relative activities of deformation modes and the V^{acc} of the twin variants developed in the three distinct regions during the Erichsen test. Figure 3.2 shows the spatial distribution of the strain components, the relative activities of the deformation modes and the V^{acc} of the twin variants that developed on the top-surface of the deformed specimen. The strain components generated in the Mg single crystal specimen were asymmetrically distributed with respect to the center of the specimen, as shown in Figure 3.2(a). In particular, ε_{xx} exhibited a considerable strain gradient in the X direction. It was interesting to note the large difference between maximum ε_{xx} (= 0.108) and maximum ε_{yy} (= 0.017) components at the center of the deformed Mg single crystal. The deformation behavior in this region deviates significantly from equi-biaxial deformation. As shown in Figure 3.2(b), the primary deformation mode in the RA and RB is basal $\langle \boldsymbol{a} \rangle$ slip, and the primary deformation mode in the RC is TTW. It is interesting to note that the V^{acc} of twin variants on the top-surface corresponded mostly to the region of negative ε_{yy}. Among the six twin variants, TT2, TT3, TT5 and TT6 were mainly activated on the circumferential area of the top-surface (Figure 3.2(b)).

Figure 3.3 shows the spatial distribution of strain components, the relative activities of deformation modes, and the V^{acc} of twin variants that had developed on the bottom-surface. The strain components at the bottom-surface of the deformed Mg single crystal were also asymmetrically

distributed with respect to the center of the specimen, where ε_{xx} and ε_{yy} had positive and negative values, respectively, as shown in Figure 3.3(a). As shown in Figure 3.3(b), the basal $\langle \boldsymbol{a} \rangle$ slip acted as the primary deformation mode, except for one side from the specimen center parallel to the X-axis, for which the primary deformation mode was TTW. The non-basal slip systems were weakly activated only at the edge of the specimen in the RC parallel to the Y-axis. Figures 3.4 and 3.5 show the CPFEM results for strain components, the relative activity of deformation modes, and the V^{acc} of twin variants that developed on the Y-Z and X-Z sections, respectively. It is recently reported that, due to the orthotropic texture, the stress state through the thickness direction in polycrystalline Mg is also inhomogeneous during the Erichsen test at RT [20]. The spatial distributions of ε_{xx} and ε_{yy} in the RA indicates that biaxial tensile strain is applied along both x and y directions in the upper portion, while tensile and compressive strains are applied in the x and y directions in the lower portion. The spatial distribution of ε_{yy} that developed on the Y-Z section (Figure 3.4(a)) indicated that tensile strain was applied to the upper portion of RA and to the lower portion of RC, while compressive strain was applied to the lower portion of RA and to the upper portion of RC. On the other hand, the spatial distribution of ε_{yy} that developed on the X-Z section (Figure 3.5(a)) indicates that tensile strain was applied to the upper portion of RA while compressive strain was applied to the lower portions of both RA and RB. It is noteworthy that the ε_{yy} that had developed on the X-Z section was almost zero through the thickness direction at the dome edge of RC, meaning that this geometrically approximated plain-strain conditions. On the other hand, considering the strain components observed with the Y-Z section at the dome edge of the RC, the deformation

behavior of this region seemed similar to that obtained in the V-bending test [18]. In other words, the outer and inner portions of RC are considered as tension and compression zones, respectively. Interestingly, the RB in the Y-Z section did not effectively contribute to the deformation, which indicated that it was difficult to deform the specimen in the y direction during the Erichsen test, and the V-bending effect that occurred in the RC enabled the dome to deform. Figures 3.4(b) and 3.5(b) show the V^{acc} of the TTW variants in the Y-Z and X-Z sections, respectively. In the RA, regardless of section, the values for V^{acc} of the TT1 and TT4 in the upper portion were relatively higher than those in the lower portion, while the values for V^{acc} of the TT2, TT3, TT5 and TT6 in the lower portion were relatively higher than those in the upper portion. This behavior can be attributed to tensile deformation in the y direction in this portion during the Erichsen test. Based on the experimental results, this will be discussed in more detail in Section 3.2.2. In the RB, the V^{acc} of all twin variants was negligible in the Y-Z section, and the V^{acc} of the TT3 and TT5 at the bottom of the specimen in the X-Z section was relatively higher than that of the other twin variants. This behavior seemed due to the tensile strain in the x direction and to the compressive strain in the y direction in the lower portion of the X-Z section. In RC, the V^{acc} at the upper portion of the specimen in the Y-Z section was relatively higher than that at the lower portion because the strain was small in the x direction but compressive strain was acting in the y direction in this portion. On the other hand, the value for V^{acc} was low at the center of the specimen in the X-Z section despite a high relative activity of twin, which can be attributed to a relatively low level of deformation in RC during the Erichsen test compared with that in both RA and RB.

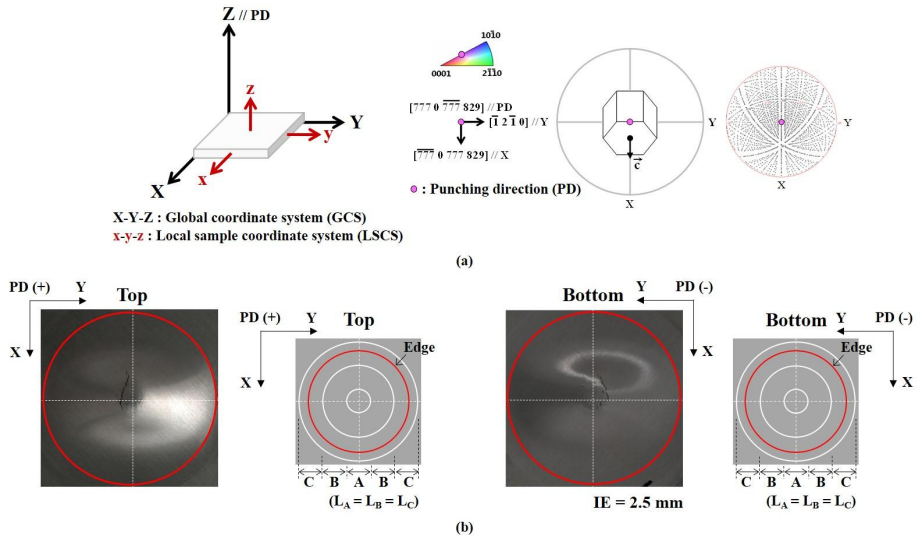

Figure 3.1 (a) Initial crystallographic orientation and (b) Erichsen test results of orientation A (IE = 2.5 mm).

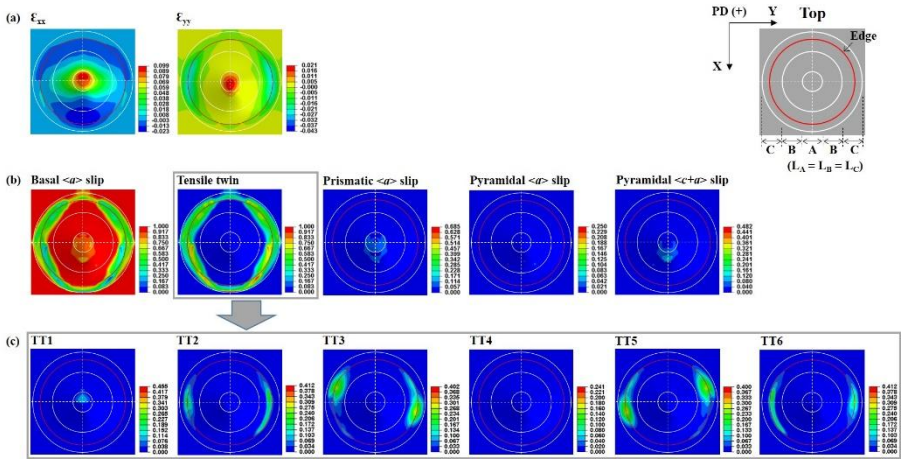

Figure 3.2 CPFEM results for the top-surface of orientation A (IE = 2.5 mm) after the Erichsen simulation: spatial distribution of (a) strain components, (b) relative activities of deformation modes, and (c) accumulated volume fraction of TTW variants.

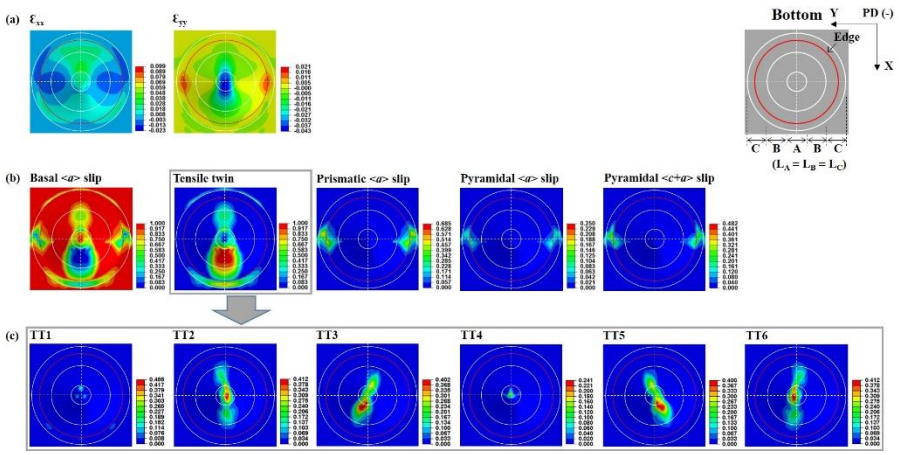

Figure 3.3 CPFEM results for the bottom-surface of orientation A (IE = 2.5 mm) after the Erichsen simulation: spatial distribution of (a) strain components, (b) relative activities of deformation modes, and (b) accumulated volume fraction of TTW variants.

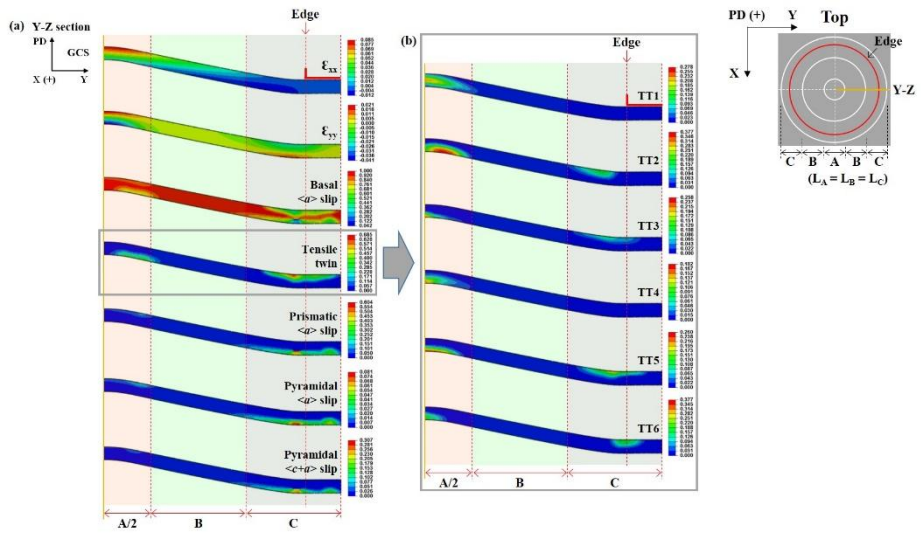

Figure 3.4 CPFEM results for the Y-Z section of orientation A (IE = 2.5 mm) after the Erichsen simulation: spatial distribution of (a) strain components, relative activities of deformation modes, and (b) accumulated volume fraction of TTW variants.

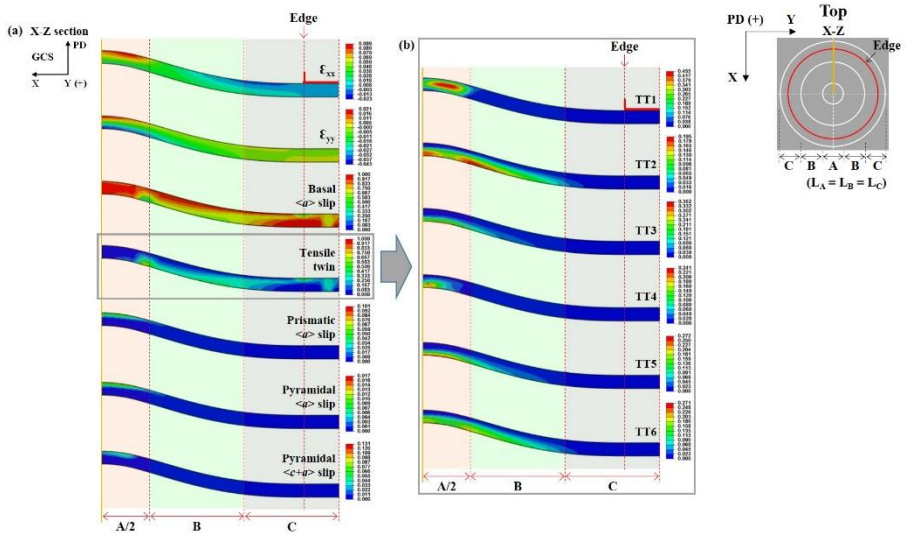

Figure 3.5 CPFEM results for the X-Z section of orientation A (IE = 2.5 mm) after the Erichsen simulation: spatial distribution of (a) strain components, relative activities of deformation modes and (b) accumulated volume fraction of TTW variants.

3.1.2. Characterization of TBs using EBSD analysis

Figure 3.6(a) is a schematic representation of the Y-Z and X-Z sections after the Erichsen test. Analysis of the microtexture evolutions in RB was divided into two portions: RB1 adjacent to RA and RB2 adjacent to RC. The microtexture evolution in RC were also analyzed in two portions: RC1 adjacent to RB and RC2 adjacent to the dome edge. The PD(//Z)-inverse pole figure (PD-IPF) maps of the two cross-sections appear in Figure 3.6(b), and corresponds to the right-half of the schematic representation in Figure 3.6(a). The crystal orientation of the deformed specimen was corrected by rotation, which was based on the GCS to ease analysis. Microtexture analysis of the cross-sections revealed that the heterogeneous evolution of deformation twinning was developed in a heterogeneous manner throughout the deformed specimen, exhibiting the differences in surface slopes along X and Y directions.

Figure 3.7(a) demonstrates the TTW and compression twin (CTW) variants that can be activated from the initial crystallographic orientation of Mg single crystal during the Erichsen test. In some areas, CTW was experimentally observed and thus considered together in the twin orientation analysis. Six variants of CTW were additionally considered as follows: CT1— $(10\bar{1}1)[10\bar{1}\bar{2}]$, CT2— $(\bar{1}011)[\bar{1}01\bar{2}]$, CT3— $(01\bar{1}1)[01\bar{1}\bar{2}]$, CT4— $(0\bar{1}01)[0\bar{1}1\bar{2}]$, CT5— $(1\bar{1}01)[1\bar{1}0\bar{2}]$, and CT6— $(\bar{1}\bar{1}01)[\bar{1}10\bar{2}]$. Figure 3.7(b) depicts the geometrical calculation of TTW traces that had occurred in the Y-Z and X-Z sections during the Erichsen test. Interestingly, TT1 and TT4 were almost parallel to the horizontal and vertical directions, whereas TT2, TT3, TT5 and TT6 were analyzed to grow in a state of being inclined across the thickness of the specimen. In the Y-Z section, TT2 and

TT3 were tilted 65° clockwise (cw) and 65° counterclockwise (ccw), respectively, with respect to the y-axis. TT3 and TT5 were inclined by 38° ccw and 38° cw, respectively, with respect to the y-axis. In the X-Z section, TT1 and TT4 were almost parallel to the z-axis and the x-axis, respectively, while TT2/TT3 and TT5/TT6 were inclined by 70° ccw and 20° ccw, respectively, with respect to the x-axis.

Microtexture analysis combined with the TTW traces effectively explained the twinning behavior occurring in a deformed Mg single crystal during the Erichsen test. LSCS was used to describe the spatial morphology and variant type of TBs developed in the Y-Z and X-Z sections. Moreover, the thickness of the observation area was equally divided into five portions to explain the twinning behavior based on LSCS: upper (U), upper-middle (UM), middle (M), lower-middle (LM), and lower (L). The color used to draw the TTW traces was also applied to the TBs to more easily identify the corresponding variants.

Figure 3.8 shows the results of the twin analysis for RA. In the Y-Z section, five variants of TTW (TT1, TT2, TT3, TT5 and TT6) occurred unevenly through the thickness direction of the deformed specimen with a total twin area fraction of 0.039. TT1 was formed along the y-axis in both the U and LM portions. TT2 and TT3 were formed in the L portion in an inclining state at a specific tilt angle (~ 65°) with respect to the y-axis. TT3 had a very small amount of twin area fraction (< 0.001) that was formed in the L portion. TT5 was formed in both the L portion and the LM portion, as well as in the U portion in an inclining state at a specific tilt angle (~ 38°) with respect to the y-axis. In the X-Z section, three variants of TTW (TT1, TT3 and TT4) were activated unevenly through the thickness direction of the specimen with a total twin area fraction of 0.048. TT1 had the largest amount of twin area

fraction formed through the z-axis. TT3 was formed at the L part in an inclining state at a specific tilt angle (~ 70°) with respect to x-axis. TT4 was formed in the LM portion along the x-axis.

Figure 3.9 shows the results of the twin analysis for RB1. It is found that the deformed specimen observed on the Y-Z section is placed in a state with a ~ 7° surface slope relative to the Y-axis, whereas the deformed specimen on the X-Z section has a surface slope of ~ 21° with respect to the X-axis, which represents the largest difference in the surface slopes of the two cross-sections among five observation regions. The Y-Z section displayed no evidence of twin variants. In the X-Z section, it was analyzed that four variants of TTW (TT3, TT4, TT5 and TT6) were activated unevenly in the thickness direction of the specimen with a total twin area fraction of 0.049. TT3 was formed from in the L and M portions in an inclining state at a specific tilt angle (~ 70°) with respect to the x-axis. TT4 was formed in the M portion along the x-axis. TT5 was formed in the L and LM portions, as well as in the U portion in an inclining state at a specific tilt angle (~ 20°) with respect to the x-axis. TT6 was formed in the L portion in an inclining state at a specific tilt angle (~ 20°) with respect to the x-axis.

Figure 3.10 shows the results of the twin analysis for RB2. In the Y-Z section, three variants of TTW (TT1, TT4 and TT5) occurred unevenly through the thickness direction of the specimen with a total twin area fraction of 0.020. TT1 and TT4 were formed mainly in the U portion and also were scattered throughout the specimen along the y-axis. TT5 had a very small fraction of twin area (< 0.001) that was formed in the U portion. In the X-Z section, four variants of TTW (TT2, TT3, TT5 and TT6) were activated unevenly through the thickness direction of the specimen with a total twin area fraction of 0.061. TT2 was formed through the z-axis in an inclining state

at a specific tilt angle (~ 70°) with respect to the x-axis. TT3 had a very small fraction of twin area (~ 0.001) that was formed in the L portion and maintained a specific tilt angle (~ 70°) with respect to the x-axis. TT5 was formed in a very small region that extended from the L portion to the UM portion and maintained a specific tilt angle (~ 20°) with respect to the x-axis. TT6 had the largest fraction of twin area that was formed throughout the specimen in an inclining state at a specific tilt angle (~ 20°) with respect to the x-axis. In X-Z section of RB2, secondary TTW (STT) was also observed within the TBs of TT2 and TT5, which were nucleated and grew from the L portion. This indicated that the orientation could be changed to favor the activation of STT due to the complex stress states that occurred on a grain scale during the Erichsen test.

Figure 3.11 shows the results of the twin analysis for RC1. The Y-Z section exhibited a surface slope of ~ 10° based on the Y-axis, whereas the X-Z section has a surface slope that was almost parallel to the X-axis. In the Y-Z section, four variants of TTW (TT1, TT3, TT4 and TT5) occurred unevenly through the thickness direction of the deformed specimens with a total twin area fraction of 0.023. TT1 and TT4 were formed mainly in the U portion and were scattered throughout the specimen along the y-axis. TT3 and TT5 were formed in a very small region that extended from the U portion to the UM portion while maintaining specific tilt angles (~ 65° and ~ 38°) with respect to the y-axis. In the X-Z section four variants of TTW (TT2, TT3, TT5 and TT6) were activated unevenly through the thickness direction of the deformed specimen with a total twin area fraction of 0.049. TT2 and TT3 had a very small fraction of twin area (≤ 0.001) that were formed in the U portion in an inclining state at a specific tilt angle (~ 70°) with respect to the x-axis. TT5 was formed in a very small region that extended from the LM portion to the

M portion in an inclining state at a specific tilt angle (~ 20°) with respect to the x-axis. TT6 had the largest fraction of total twin area that was formed at the L, LM, UM and U portions in an inclining state at a specific tilt angle (~ 20°) with respect to the x-axis. The twin variants most commonly observed in the Y-Z and X-Z sections of RC1 included TT3 and TT5.

Figure 3.12 shows the results of twin analysis for RC2. In the Y-Z section, it was analyzed that all six variants of TTW occurred unevenly through the thickness direction of the specimen with a total twin area fraction of 0.075. TT1 and TT4 were formed mainly from the U portion to the M portion and were also scattered throughout the deformed specimen along the y-axis. TT2 had a very small fraction of twin area (< 0.001) that was formed from the UM portion to the M portion in an inclining state at a specific tilt angle (~ 65°) with respect to the y-axis. TT3 had the largest fraction of twin area that was formed from the U portion to the M portion in an inclining state at a specific tilt angle (~ 65°) with respect to the y-axis. TT5 was formed at the U portion in an inclining state at a specific tilt angle (~ 38°) with respect to the y-axis. TT6 had a very small fraction of twin area (~ 0.001) that was formed from the UM portion to the M portion in an inclining state at a specific tilt angle (~ 38°) with respect to the y-axis. Furthermore, two double twins (DTs), $\{10\bar{1}1\} - \{10\bar{1}2\}$, were observed within the TBs of CT5 which was nucleated and grew from the L portion to the M portion. The difference in the stress state of the L portion was responsible for the activation of CT5 and the subsequent DTs under the deformation similar to that of V-bending that is induced by an upper die. The development of DTs correlates with immediate cracking that causes premature failure in Mg [57]. The spatial distribution of the relative activity near DTs reveals that pyramidal $\langle \boldsymbol{c} + \boldsymbol{a} \rangle$ slip as well as prismatic $\langle \boldsymbol{a} \rangle$ slip is mainly observed despite a substantially high CRSS

value in the plastic deformation at RT. This result indicates that pyramidal $\langle \boldsymbol{c}+\boldsymbol{a} \rangle$ slip releases the localized stress concentration that occurs at the boundaries of DTs, which delays the formation of cracks.

In the X-Z section, four variants of TTW (TT2, TT3, TT5 and TT6) were activated unevenly through the thickness direction of the deformed specimen with a total twin area fraction of 0.035. TT2 was formed from the U portion to the M portion in an inclining state at a specific tilt angle (~ 70°) with respect to the x-axis. TT3 was formed in a very small region extending from the L portion to the LM portion in an inclining state at a specific tilt angle (~ 70°) with respect to the x-axis. TT5 had the largest fraction of twin area that was formed from the M portion to the U portion in an inclining state at a specific tilt angle (~ 20°) with respect to the x-axis. TT6 had a very small fraction of twin area (~ 0.001) that was formed from the LM portion to the M portion in an inclining state at a specific tilt angle (~ 20°) with respect to the x-axis. The twin variants commonly observed in the Y-Z and X-Z sections of RC2 were TT2, TT3, TT5, and TT6.

Figure 3.13 compares the twinning behaviors that occurred in the five subdivided regions of the (a) Y-Z and (b) X-Z sections. A majority of the TTW variants in the Y-Z section existed in the L and LM portions of RA, and in the U and UM portions of RC2. This result seemed due to the opposite strain gradient through the thickness direction. In other words, the TTWs were concentrated in the regions where the ε_{xx} component was positive and the ε_{yy} component was negative. The most important observation here is that most TBs were nucleated at the free surface of deformed specimen and tended to propagate into the matrix. In order to accommodate the initial external strain of the Erichsen test, shear deformation occurred in the basal $\langle \boldsymbol{a} \rangle$ slip system as well as in the TTW system. Accumulation of shear deformation

tended to create small irregularities in the free surface of deformed specimen. As a result, it is believed that the stress concentration occurring at these small irregularities during deformation provided the nucleation site for the TBs.

Analysis of the TTW behavior in the X-Z section quantitatively shows that the TBs in RA, RB, and RC1 developed mainly in the lower portion of the deformed specimen and the TBs in RC2 developed mainly in the upper portion of the deformed specimen. This result can be explained by the distribution of the strain components, as demonstrated in the Y-Z section. The ε_{yy} component in a region where TBs are observed has a positive value that is favorable for the nucleation of TBs, while the ε_{xx} component has a very low value in the same region of a deformed specimen. The spatial distribution of the relative activity of the TTW provided a good explanation for the location of the TTW that is observed experimentally in the deformed specimen. However, the CPFEM simulation results have limitations in accurately describing the behavior of the thin TBs generated within a deformed specimen. In particular, the occurrence of TBs in the upper portions of RA and RC1 in a deformed specimen cannot be explained by the CPFEM results. Figure 3.14 depicts a possibility of twin evolution for TT1 and TT4 in the X-Z section of RA. It was unclear whether the nucleation site of the TBs of TT1 in the upper portion of RA was near the U portion or the M portion of the deformed specimen. Here, due to the bulky size of the single crystal, which was more complicated than an ideal single crystal without any pre-existing defects on a nanoscale, other factors had to be considered. If the U portion was closest, it can be thought that TBs were created by the stress concentration at the free surface of the deformed specimen, and some of them are cut on the Y-Z section and only partially revealed. On the other hand, if the M part was closest, it indicated the presence of microstructural

heterogeneities such as impurities, voids or inclusions in the deformed specimen that induced a concentration of stress that favored the nucleation of TBs. Another possibility is the generation of TBs by the concentration of stress at the boundary of the TBs of TT4, which were generated parallel to the x-axis in the LM portion of the deformed specimen. The nucleation mechanism of the TBs of TT4 in the LM of the deformed specimen RA is also unclear. Twin nuclei may form in a particular region of a near-perfect crystal under the applied stress or when a suitable defect configuration is present [58]. The results of atomic unit modeling using the recent molecular dynamics of pure Mg have shown that the characteristics of fine pores and the character of grain boundaries influence the formation of TBs [59–62]. The nucleation site of twins is associated with the stress field of twinning dislocations and the grain boundary, as a defect site with high density of dislocation, can induce the twin nucleation [63]. In addition, when minute pores are present inside a specimen, stress concentration may occur at the boundaries between the pores and the base during the Erichsen test, which greatly increases the possibilities for the nucleation of the TBs. At this point, no experimental evidence is available to explain this phenomenon, and further in-depth research will be conducted.

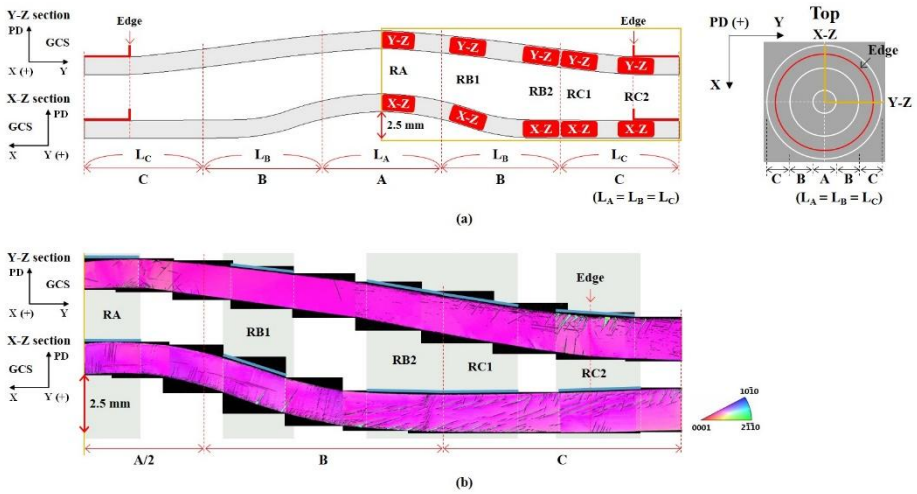

Figure 3.6 (a) Schematic diagram and (b) the PD(//Z)-inverse pole figure (PD-IPF) maps in the Y-Z and X-Z sections (corresponding to the right half of the schematic diagram) of orientation A (IE = 2.5 mm).

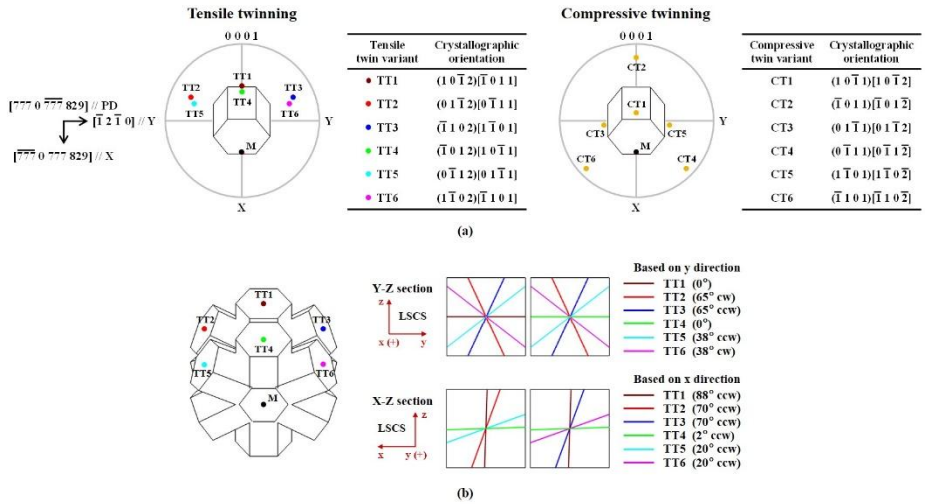

Tensile twin variant	Crystallographic orientation
TT1	$(1\,0\,\bar{1}\,2)[\bar{1}\,0\,1\,1]$
TT2	$(0\,1\,\bar{1}\,2)[0\,\bar{1}\,1\,1]$
TT3	$(\bar{1}\,1\,0\,2)[1\,\bar{1}\,0\,1]$
TT4	$(\bar{1}\,0\,1\,2)[1\,0\,\bar{1}\,1]$
TT5	$(0\,\bar{1}\,1\,2)[0\,1\,\bar{1}\,1]$
TT6	$(1\,\bar{1}\,0\,2)[\bar{1}\,1\,0\,1]$

Compressive twin variant	Crystallographic orientation
CT1	$(1\,0\,\bar{1}\,1)[1\,0\,\bar{1}\,2]$
CT2	$(\bar{1}\,0\,1\,1)[\bar{1}\,0\,1\,\bar{2}]$
CT3	$(0\,1\,\bar{1}\,1)[0\,1\,\bar{1}\,2]$
CT4	$(0\,\bar{1}\,1\,1)[0\,\bar{1}\,1\,\bar{2}]$
CT5	$(1\,\bar{1}\,0\,1)[1\,\bar{1}\,0\,\bar{2}]$
CT6	$(\bar{1}\,1\,0\,1)[\bar{1}\,1\,0\,\bar{2}]$

Figure 3.7 (a) TTW and CTW variants with their corresponding Miller indices for the initial crystallographic orientation and (b) geometrical calculation of TTW traces occurring in the Y-Z and X-Z sections of orientation A (IE = 2.5 mm).

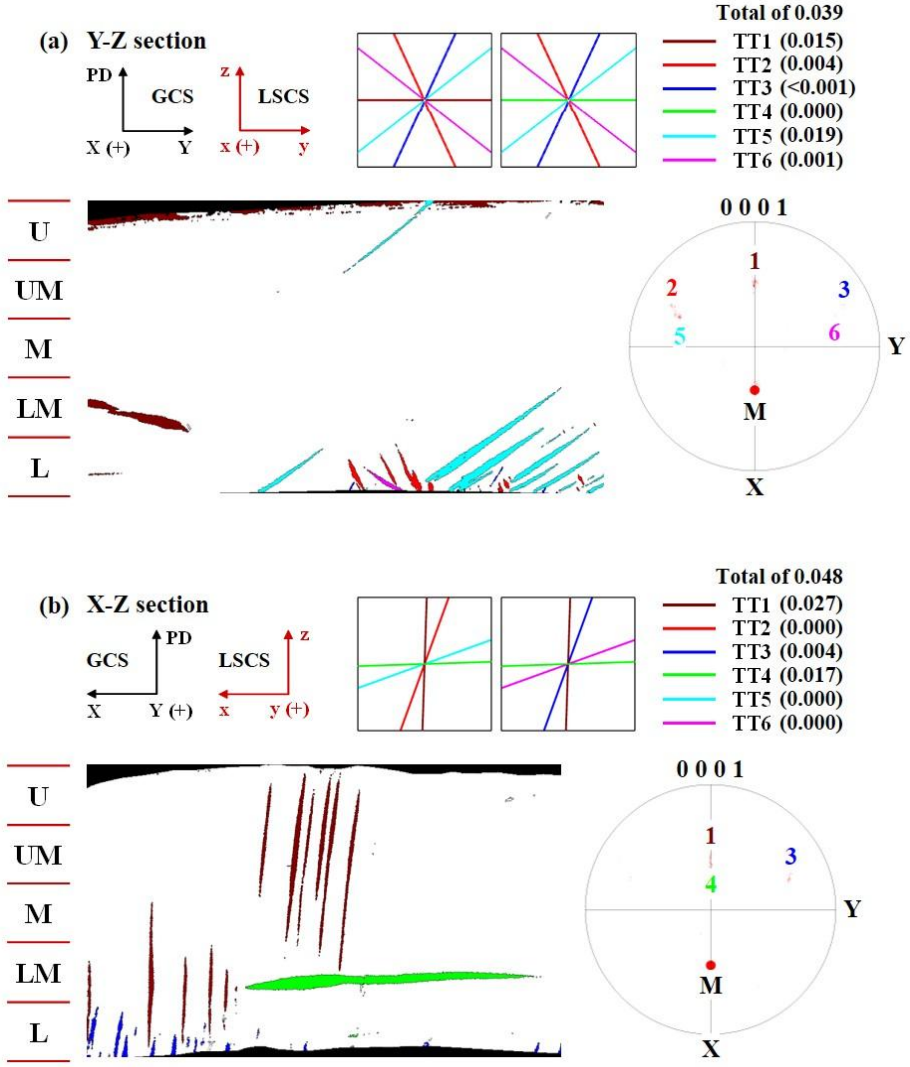

Figure 3.8 Twin analysis of RA in the (a) Y-Z and (b) X-Z sections of orientation A (IE = 2.5 mm).

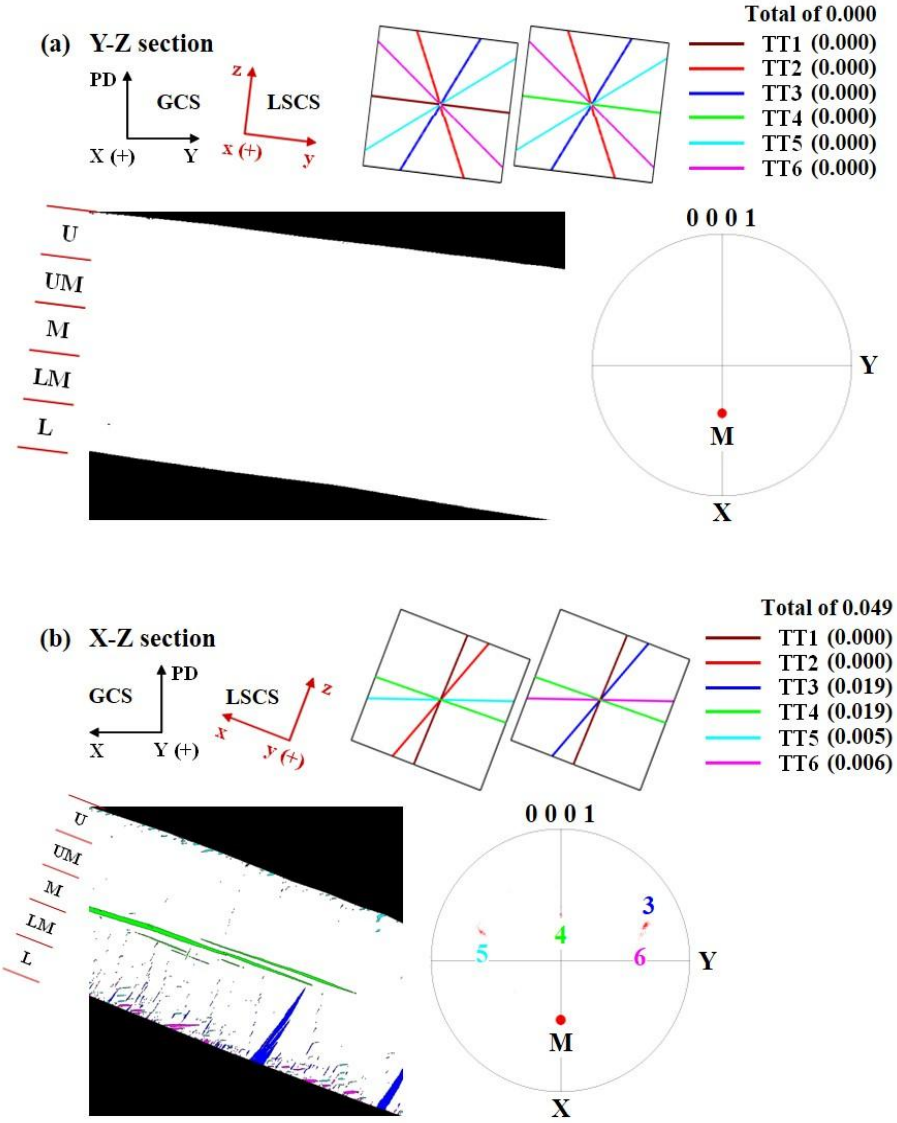

Figure 3.9 Twin analysis of RB1 in the (a) Y-Z and (b) X-Z sections of orientation A (IE = 2.5 mm).

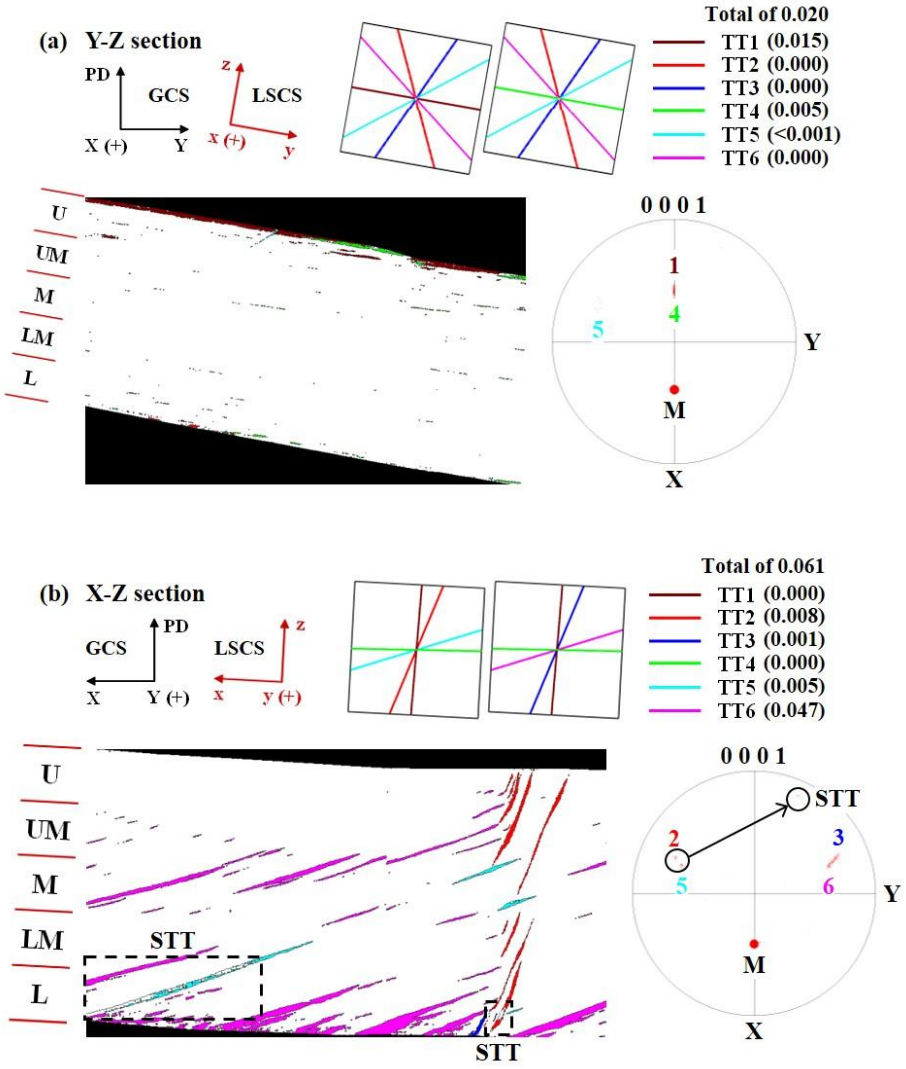

Figure 3.10 Twin analysis of RB2 in the (a) Y-Z and (b) X-Z sections of orientation A (IE = 2.5 mm).

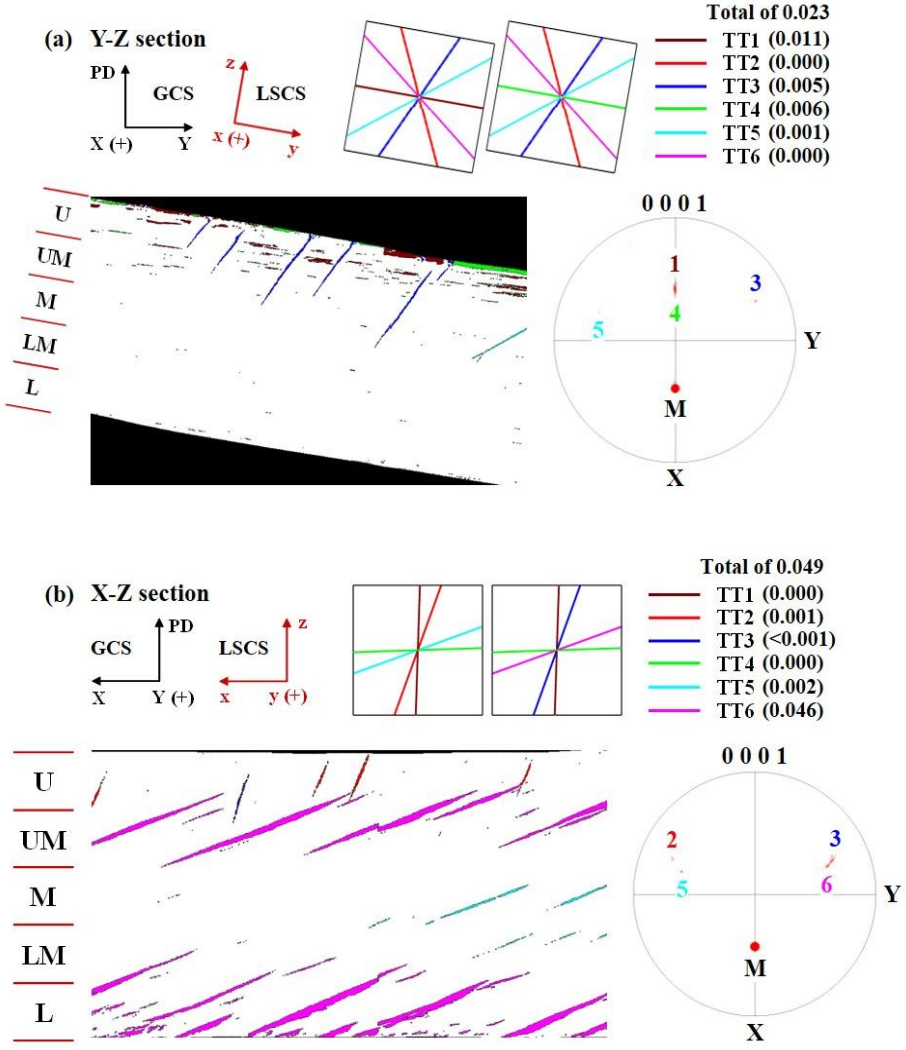

Figure 3.11 Twin analysis of RC1 in the (a) Y-Z and (b) X-Z sections of orientation A (IE = 2.5 mm).

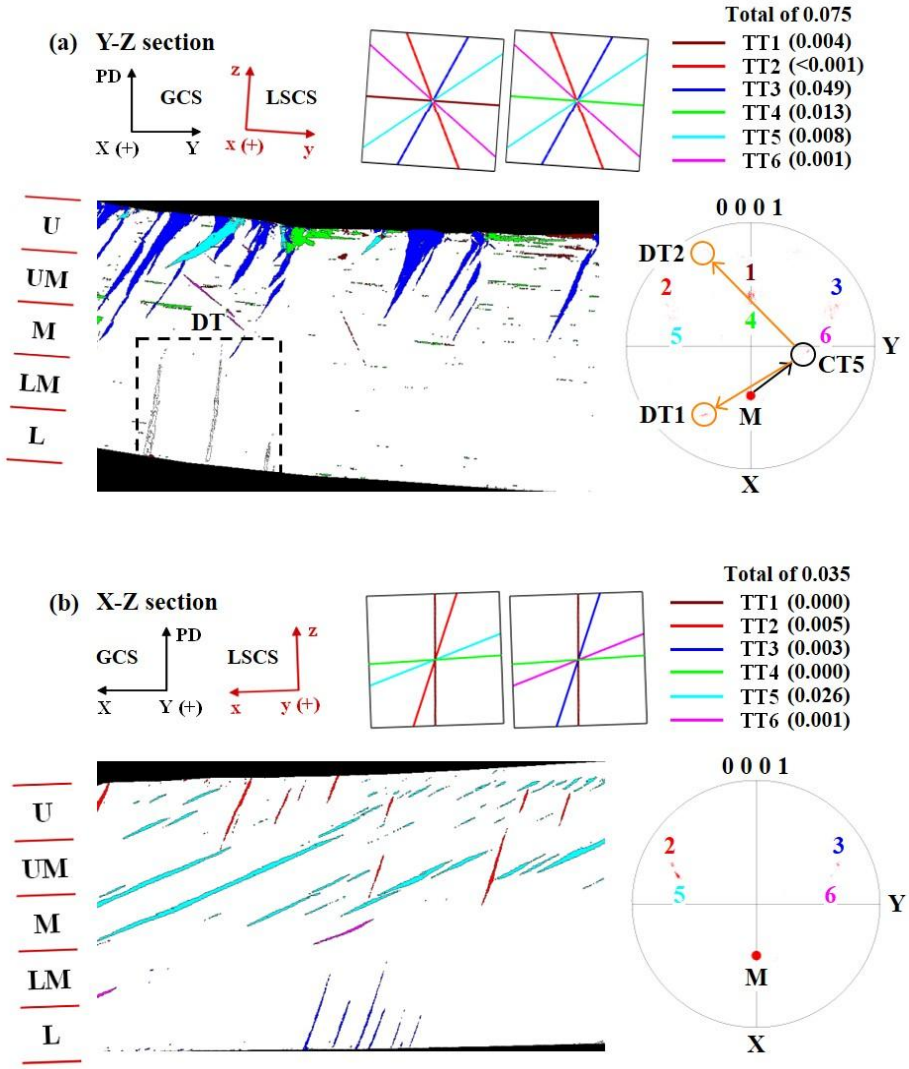

Figure 3.12 Twin analysis of RC2 in the (a) Y-Z and (b) X-Z sections of orientation A (IE = 2.5 mm).

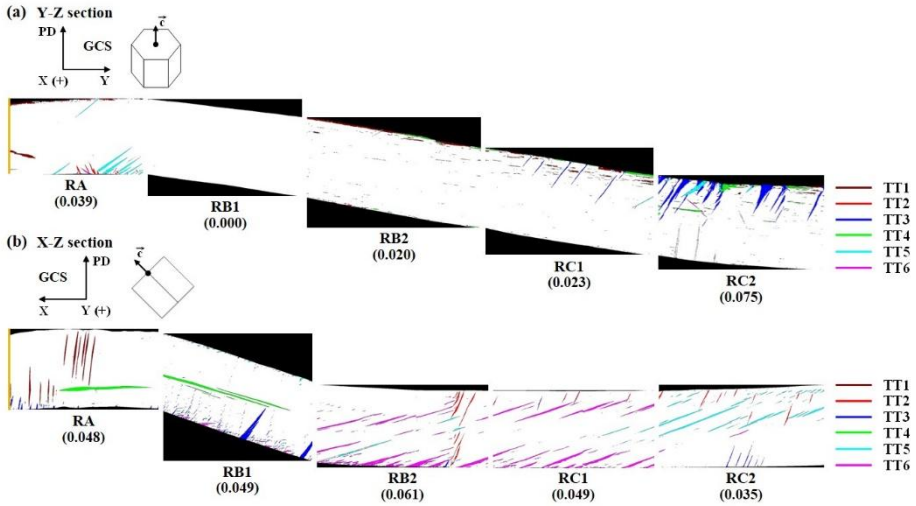

Figure 3.13 A comparison of the five subdivided regions in the (a) Y-Z and (b) X-Z sections of orientation A (IE = 2.5 mm).

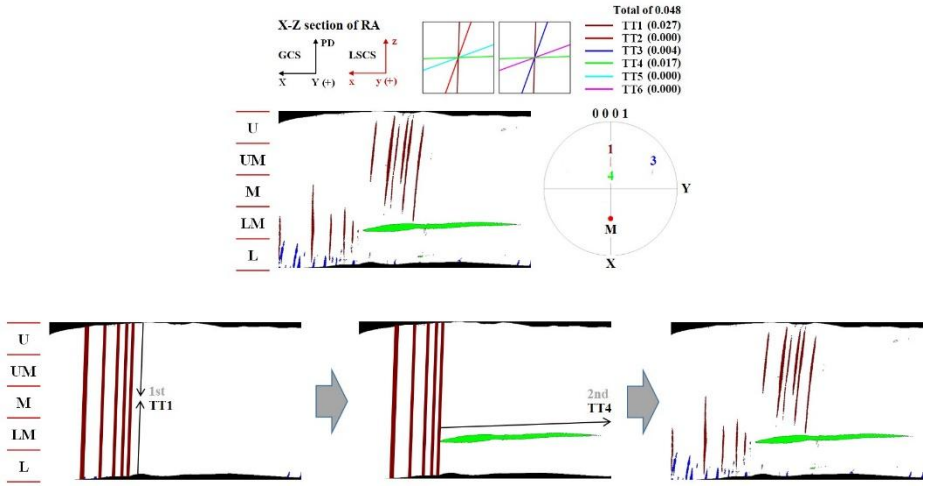

Figure 3.14 A possibility of twin evolution for TT1 and TT4 in the X-Z section of RA.

3.2 Conclusion

The twinning behavior and deformation mechanisms that occur in a deformed Mg single crystal during the Erichsen test at RT were investigated via experimental and theoretical approaches.

Microtexture analysis combined with the TTW traces of the cross-sections of a deformed Mg single crystal revealed heterogeneous twinning behavior during an Erichsen test at RT. The thin TBs with different types of variants were produced with non-uniform area fraction throughout the specimen and showed a tendency to propagate in an inclining state at a specific tilt angle depending on the type of twin variants. Most TBs were generated on the free surface of the deformed specimen and some TBs were generated and propagated inside the deformed specimen.

CPFEM results revealed that the in-plane strain components (ε_{xx} and ε_{yy}) generated in the deformed Mg single crystal specimen were asymmetrically distributed with respect to the center of the specimen, and the deformation behavior in the center region showed a significant deviation from equi-biaxial deformation. A region with a positive ε_{xx} and a negative ε_{yy} was more favorable to the nucleation of TBs during the Erichsen test at RT. The spatial distribution of TTW activity obtained from the CPFEM results successfully accounted for most of the twinning evolution observed experimentally in deformed specimens. However, the CPFEM simulation results failed to explain the behavior of some TBs nucleated within the deformed specimen.

Chapter 4. Effect of initial crystallographic orientation on room temperature stretch formability in Mg single crystal

4.1 Results and discussion (Orientation B (IE = 6.8 mm))

4.1.1 Erichsen test simulation using CPFEM

In the case of the Erichsen test, the specimen is subjected to a non-uniform deformation history in the plane and thickness directions of the specimen. Furthermore, since the anisotropy of single crystal specimens is so strong, the non-uniformity of deformation in a deformed specimen becomes much more intense, which necessitates an understanding of the non-uniformity of deformation using simulation techniques such as CPFEM. When the PD is parallel to the $[1\ 0\ \bar{1}\ 0]$ direction, the initial crystallographic orientation of a Mg single crystal during the Erichsen test has the orientation relationship of 90° between PD and c-axis, which can be expressed as (ϕ_1, Φ, ϕ_2) = (-90°, 90°, 60°) in Euler space, as described in Figure 4.1(a). The results of the Erichsen test at RT in Figure 4.1(b) show that plastic anisotropy induced an asymmetrically deformed dome shape with respect to the center of both the top and bottom of the deformed specimen under a punch stroke with an IE of 6.8 mm. Furthermore, in order to systematically investigate the twinning behavior and deformation mechanisms during the Erichsen test, the deformed specimen was equally divided into three distinct regions ($L_A = L_B = L_C$). The three distinct regions are defined as follows. Region A (RA) is the

area near the center of the deformed specimen, and is the point at which severe biaxial strain (or stress) occurs during an Erichsen test. Region B (RB) is the intermediate area between the center and the circumference of the deformed specimen. Region C (RC) is the area of the circumference of the deformed specimen, and it the point at which an upper die imposes normal pressure during an Erichsen test.

CPFEM simulation can identify the spatial distribution of strain components, the relative activities of deformation modes and the V^{acc} of the twin variants developed in the three distinct regions during the Erichsen test. Figure 4.2 shows the spatial distribution of the strain components, the relative activities of the deformation modes and the V^{acc} of the twin variants that developed on the top-surface of the deformed specimen. The strain components generated in the Mg single crystal specimen were symmetrically distributed with respect to the center of the specimen, as shown in Figure 4.2(a). In particular, ε_{xx} exhibited a considerable strain gradient in the X direction. It was interesting to note the large difference between maximum ε_{xx} (= 0.239) and maximum ε_{yy} (= 0.055) components at the center of the deformed Mg single crystal. The deformation behavior in this region deviates significantly from equi-biaxial deformation. As shown in Figure 4.2(b), the primary deformation mode in the RA and RB is TTW, and the primary deformation mode in the RC is basal $\langle \boldsymbol{a} \rangle$ slip. It is interesting to note that the V^{acc} of twin variants on the top-surface corresponded mostly to the region of negative ε_{yy}. Among the six twin variants, TT2, TT3, TT5 and TT6 were mainly activated on the circumferential area of the top-surface (Figure 4.2(b)).

Figure 4.3 shows the spatial distribution of strain components, the relative activities of deformation modes, and the V^{acc} of twin variants that had developed on the bottom-surface. The strain components at the bottom-

surface of the deformed Mg single crystal were also symmetrically distributed with respect to the center of the specimen, where ε_{xx} and ε_{yy} had positive and negative values, respectively, as shown in Figure 4.3(a). As shown in Figure 4.3(b), the basal $\langle \boldsymbol{a} \rangle$ slip acted as the primary deformation mode, except for one side from the specimen center parallel to the X-axis, for which the primary deformation mode was TTW. The non-basal slip systems were weakly activated only at the edge of the specimen in the RC parallel to the Y-axis. Figures 4.4 and 4.5 show the CPFEM results for strain components, the relative activity of deformation modes, and the V^{acc} of twin variants that developed on the Y-Z and X-Z sections, respectively. It is recently reported that, due to the orthotropic texture, the stress state through the thickness direction in polycrystalline Mg is also inhomogeneous during the Erichsen test at RT [20]. The spatial distributions of ε_{xx} and ε_{yy} in the RA indicates that biaxial tensile strain is applied along both x and y directions in the upper portion, while tensile and compressive strains are applied in the x and y directions in the lower portion. The spatial distribution of ε_{yy} that developed on the Y-Z section (Figure 4.4(a)) indicated that tensile strain was applied to the upper portion of RA and to the lower portion of RC, while compressive strain was applied to the lower portion of RA and to the upper portion of RC. On the other hand, the spatial distribution of ε_{yy} that developed on the X-Z section (Figure 4.5(a)) indicates that tensile strain was applied to the upper portion of RA while compressive strain was mostly applied to the lower portions of both RA and RB. It is noteworthy that the ε_{yy} that had developed on the X-Z section was almost zero through the thickness direction at the dome edge of RC, meaning that this geometrically approximated plain-strain conditions. On the other hand, considering the strain components observed

with the Y-Z section at the dome edge of the RC, the deformation behavior of this region seemed similar to that obtained in the V-bending test [18]. In other words, the outer and inner portions of RC are considered as tension and compression zones, respectively. Figures 4.4(b) and 4.5(b) show the V^{acc} of the TTW variants in the Y-Z and X-Z sections, respectively. In the RA, regardless of section, the values for V^{acc} of the TT1 and TT4 in the upper portion were relatively higher than those in the lower portion, while the values for V^{acc} of the TT2, TT3, TT5 and TT6 in the lower portion were relatively higher than those in the upper portion. This behavior can be attributed to tensile deformation in the y direction in this portion during the Erichsen test. Based on the experimental results, this will be discussed in more detail in Section 4.1.2. In the RB, the V^{acc} of the TT2 and TT5 was negligible in the Y-Z section, and the V^{acc} of the TT2, TT3, TT5 and TT6 at the bottom of the specimen in the X-Z section was relatively higher than that of the other twin variants. This behavior seemed due to the tensile strain in the x direction and to the compressive strain in the y direction in the lower portion of the X-Z section. In the RC, the V^{acc} at the upper portion of the specimen in the Y-Z section was relatively higher than that at the lower portion because the strain was small in the x direction but compressive strain was acting in the y direction in this portion. On the other hand, the value for V^{acc} was low at the center of the specimen in the X-Z section despite a high relative activity of twin, which can be attributed to a relatively low level of deformation in RC during the Erichsen test compared with that in both RA and RB.

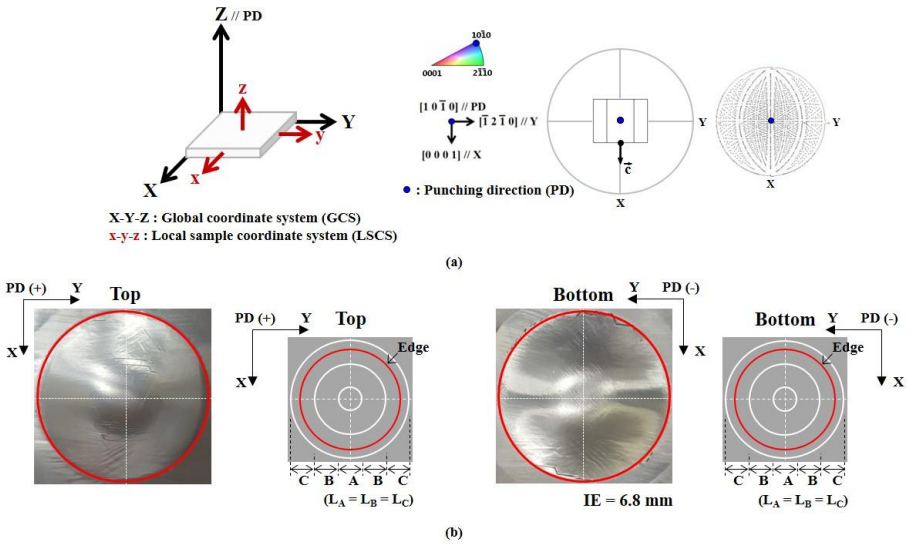

Figure 4.1 (a) Initial crystallographic orientation and (b) Erichsen test results of orientation B (IE = 6.8 mm).

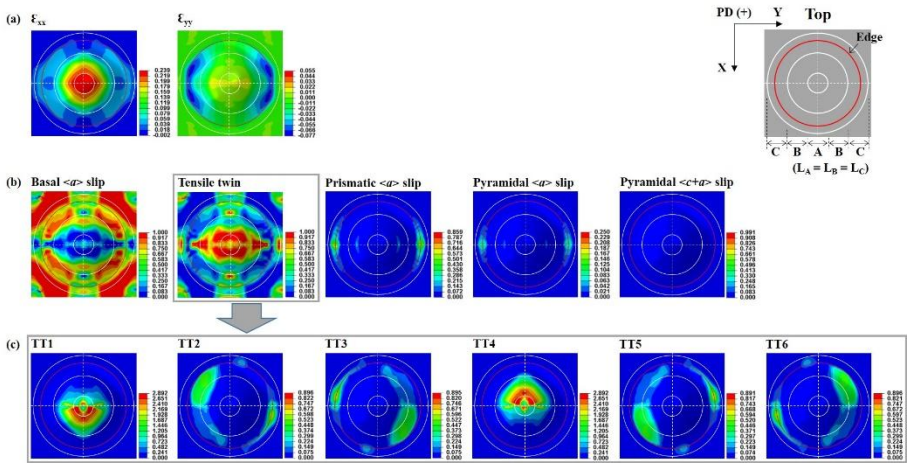

Figure 4.2 CPFEM results for the top-surface of orientation B (IE = 6.8 mm) after the Erichsen simulation: spatial distribution of (a) strain components, (b) relative activities of deformation modes, and (c) accumulated volume fraction of TTW variants.

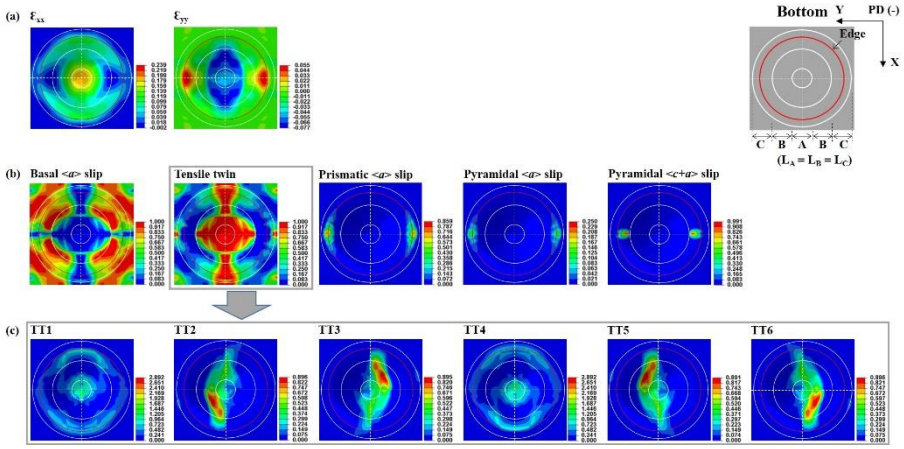

Figure 4.3 CPFEM results for the bottom-surface of orientation B (IE = 6.8 mm) after the Erichsen simulation: spatial distribution of (a) strain components, (b) relative activities of deformation modes, and (b) accumulated volume fraction of TTW variants.

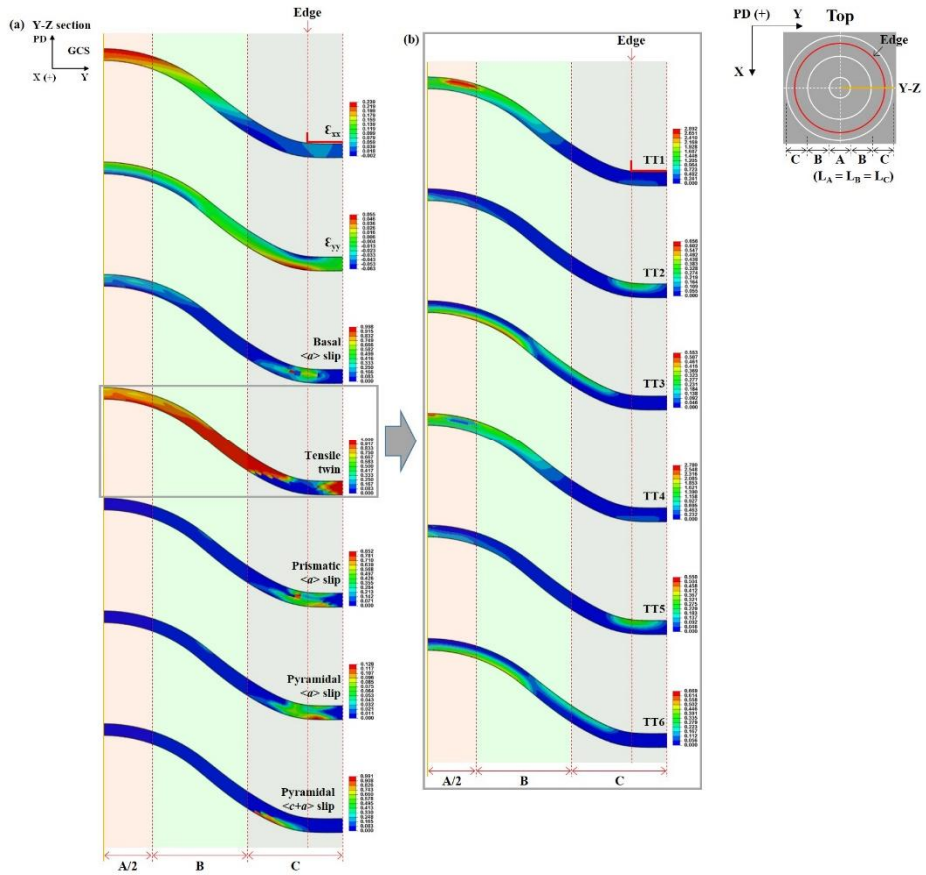

Figure 4.4 CPFEM results for the Y-Z section of orientation B (IE = 6.8 mm) after the Erichsen simulation: spatial distribution of (a) strain components, relative activities of deformation modes, and (b) accumulated volume fraction of TTW variants.

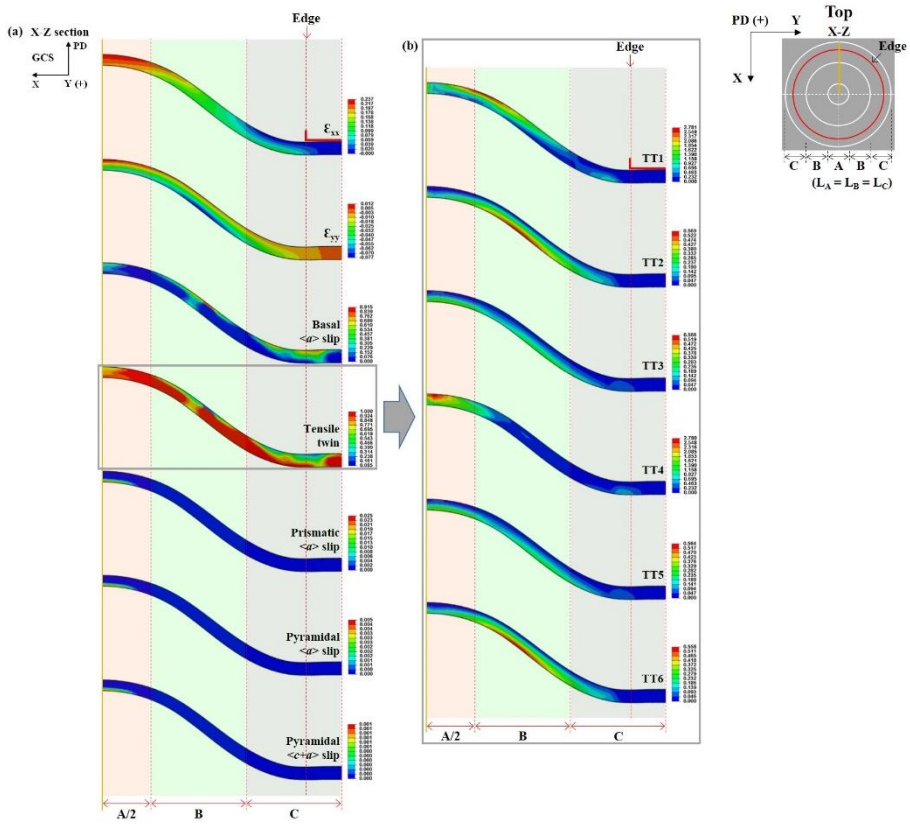

Figure 4.5 CPFEM results for the X-Z section of orientation B (IE = 6.8 mm) after the Erichsen simulation: spatial distribution of (a) strain components, relative activities of deformation modes and (b) accumulated volume fraction of TTW variants.

4.1.2 Characterization of TBs using EBSD analysis

Figure 4.6(a) demonstrates the TTW and compression twin (CTW) variants that can be activated from the initial crystallographic orientation of Mg single crystal during the Erichsen test. In some areas, CTW was experimentally observed and thus considered together in the twin orientation analysis. Six variants of CTW were additionally considered as follows: CT1— $(10\bar{1}1)[10\bar{1}\bar{2}]$, CT2— $(\bar{1}011)[\bar{1}01\bar{2}]$, CT3— $(01\bar{1}1)[01\bar{1}\bar{2}]$, CT4— $(0\bar{1}01)[0\bar{1}1\bar{2}]$, CT5— $(1\bar{1}01)[1\bar{1}0\bar{2}]$, and CT6— $(\bar{1}\bar{1}01)[\bar{1}10\bar{2}]$. Figure 4.6(b) depicts the geometrical calculation of TTW traces that had occurred in the Y-Z and X-Z sections during the Erichsen test. In the Y-Z section, TT1 and TT4 were parallel to the horizontal direction, whereas TT2/TT3 and TT5/TT6 were tilted 60° clockwise (cw) and 60° counterclockwise (ccw) respectively based on the y-axis. In the X-Z section, TT1 and TT4 were tilted 47° cw and 47° ccw respectively based on the x-axis. Likewise, TT2/TT3 and TT5/TT6 were inclined by 65° cw and 65° ccw respectively based on the x-axis.

Figure 4.7(a) is a schematic representation of the Y-Z and X-Z sections after the Erichsen test. Analysis of the microtexture evolutions in RB was divided into two portions: RB1 adjacent to RA and RB2 adjacent to RC. The microtexture evolution in RC were also analyzed in two portions: RC1 adjacent to RB and RC2 adjacent to the dome edge. The PD(//Z)-inverse pole figure (PD-IPF) maps of the two cross-sections appear in Figure 4.7(b), and corresponds to the right-half of the schematic representation in Figure 4.7(a). The crystal orientation of the deformed specimen was corrected by rotation, which was based on the GCS to ease analysis. Microtexture analysis of the cross-sections revealed that the heterogeneous evolution of deformation

twinning was developed in a heterogeneous manner throughout the deformed specimen, exhibiting the differences in surface slopes along X and Y directions.

Microtexture analysis combined with the TTW traces effectively explained the twinning behavior occurring in a deformed Mg single crystal during the Erichsen test. LSCS was used to describe the spatial morphology and variant type of TBs developed in the Y-Z and X-Z sections. Moreover, the thickness of the observation area was equally divided into five portions to explain the twinning behavior based on LSCS: upper (U), upper-middle (UM), middle (M), lower-middle (LM), and lower (L). The color used to draw the TTW traces was also applied to the TBs to more easily identify the corresponding variants.

Figure 4.8 shows the results of the twin analysis for RA. In the Y-Z section, four variants of TTW (TT1, TT3, TT4 and TT5) occurred unevenly through the thickness direction of the deformed specimen with a total twin area fraction of 0.890. TT1 with the largest fraction of twinned area (0.601) was formed throughout the specimen (from the U portion to the L portion) along the y-axis. TT3 was formed from the L portion to the UM portion in an inclining state at a specific tilt angle (~ 60° cw) with respect to the y-axis. TT4 was formed from the UM portion to the L portion along the y-axis. TT5 was formed from the L portion to the UM portion in an inclining state at a specific tilt angle (~ 60° ccw) with respect to the y-axis. In the X-Z section, four variants of TTW (TT1, TT2, TT4 and TT6) were activated unevenly through the thickness direction of the specimen with a total twin area fraction of 0.921. TT1 with the largest fraction of twinned area (0.653) was formed throughout the specimen (from the U portion to the L portion) in an inclining state at a specific tilt angle (~ 47° cw) with respect to the x-axis. TT2 was

formed from the L portion to the M portion in an inclining state at a specific tilt angle (~ 65° cw) with respect to the x-axis. TT4 was formed throughout the specimen (from the U portion to the L portion), mostly in the M portion, in an inclining state at a specific tilt angle (~ 47° ccw) with respect to the x-axis. TT6 was formed from the L portion to the UM portion in an inclining state at a specific tilt angle (~ 65° ccw) with respect to the x-axis. The commonly observed twin variants in the Y-Z and X-Z sections of RA were TT1 and TT4.

Figure 4.9 shows the results of the twin analysis for RB1. It is found that the deformed specimen observed on the Y-Z section is placed in a state with a ~ 28° surface slope relative to the Y-axis, whereas the deformed specimen on the X-Z section has a surface slope of ~ 25° with respect to the X-axis. In the Y-Z section, four variants of TTW (TT1, TT3, TT4 and TT5) occurred unevenly through the thickness direction of the deformed specimen with a total twin area fraction of 0.368. TT1 was formed from the U portion to the LM portion along the y-axis. TT3 with the largest fraction of twinned area (0.130) was formed from the L portion to the M portion in an inclining state at a specific tilt angle (~ 60° cw) with respect to the y-axis. TT4 was formed from the U portion to the M portion along the y-axis. TT5 was formed from the L portion to the LM portion in an inclining state at a specific tilt angle (~ 60° ccw) with respect to the y-axis. In the X-Z section, four variants of TTW (TT1, TT2, TT4 and TT6) were activated unevenly through the thickness direction of the specimen with a total twin area fraction of 0.867. TT1 was formed throughout the specimen (from the U portion to the L portion) in an inclining state at a specific tilt angle (~ 47° cw) with respect to the x-axis. TT2 with the largest fraction of twinned area (0.482) was formed throughout the specimen (from the L portion to the U portion) in an inclining state at a

specific tilt angle (~ 65° cw) with respect to the x-axis. TT4 with a very small fraction of twinned area (< 0.001) was formed in both the L and LM portion as well as in the UM portion in an inclining state at a specific tilt angle (~ 47° ccw) with respect to the x-axis. TT6 was formed throughout the specimen (from the L portion to the U portion) in an inclining state at a specific tilt angle (~ 65° ccw) with respect to the x-axis. The commonly observed twin variants in the Y-Z and X-Z sections of RB1 were TT1 and TT4.

Figure 4.10 shows the results of the twin analysis for RB2. Both the Y-Z and X-Z sections exhibited a surface slope of ~ 32° based on the Y- and X-axes respectively. In the Y-Z section, four variants of TTW (TT1, TT3, TT4 and TT5) occurred unevenly through the thickness direction of the deformed specimen with a total twin area fraction of 0.102. TT1 with the largest fraction of twinned area (0.058) was formed from the U portion to the LM portion along the y-axis. TT3 was formed from the U portion to the M portion as well as in the L portion in an inclining state at a specific tilt angle (~ 60° cw) with respect to the y-axis. TT4 was formed from the UM portion to the M portion along the y-axis. TT5 was formed from the U portion to the UM portion in an inclining state at a specific tilt angle (~ 60° ccw) with respect to the y-axis. In the X-Z section, all the six variants of TTW were activated unevenly through the thickness direction of the specimen with a total twin area fraction of 0.895. TT1 was formed throughout the specimen (from the U portion to the L portion) in an inclining state at a specific tilt angle (~ 47° cw) with respect to the x-axis. TT2 and TT5 with the largest fraction of twinned area (0.664) were formed throughout the specimen (from the L portion to the U portion) in an inclining state at a specific tilt angle (~ 65° cw and ~ 65° ccw respectively) with respect to the x-axis. TT3 was formed from the L portion to the M portion in an inclining state at a specific tilt angle (~ 65° cw) with respect to

the x-axis. TT4 was formed throughout the specimen (from the U portion to the L portion) in an inclining state at a specific tilt angle (~ 47° ccw) with respect to the x-axis. TT6 was formed from the L portion to the UM portion in an inclining state at a specific tilt angle (~ 65° ccw) with respect to the x-axis. The commonly observed twin variants in the Y-Z and X-Z sections of RB2 were TT1, TT3, TT4 and TT5.

Figure 4.11 shows the results of the twin analysis for RC1. Both the Y-Z and X-Z sections exhibited a surface slope of ~ 29° based on the Y- and X-axes respectively. In the Y-Z section, three variants of TTW (TT1, TT3 and TT5) occurred unevenly through the thickness direction of the deformed specimens with a total twin area fraction of 0.059. TT1 was formed from the U portion to the UM portion as well as in the L portion along the y-axis. TT3 with the largest fraction of twinned area (0.048) was formed from the U portion to the LM portion in an inclining state at a specific tilt angle (~ 60° cw) with respect to the y-axis. TT5 was formed from the U portion to the M portion in an inclining state at a specific tilt angle (~ 60° ccw) with respect to the y-axis. In the X-Z section, all the six variants of TTW were activated unevenly through the thickness direction of the specimen with a total twin area fraction of 0.818. TT1 with the largest fraction of twinned area (0.286) was formed throughout the specimen (from the U portion to the L portion) in an inclining state at a specific tilt angle (~ 47° cw) with respect to the x-axis. TT2 was formed from the L portion to the UM portion in an inclining state at a specific tilt angle (~ 65° cw) with respect to the x-axis. TT3 was formed from the LM portion to the UM portion in an inclining state at a specific tilt angle (~ 65° cw) with respect to the x-axis. TT4 was formed throughout the specimen (from the U portion to the L portion) in an inclining state at a specific tilt angle (~ 47° ccw) with respect to the x-axis. TT5 was formed

throughout the specimen (from the L portion to the U portion) in an inclining state at a specific tilt angle (~ 65° ccw) with respect to the x-axis. TT6 was also formed throughout the specimen (from the L portion to the U portion) in an inclining state at a specific tilt angle (~ 65° ccw) with respect to the x-axis. The commonly observed twin variants in the Y-Z and X-Z sections of RC1 were TT1, TT3 and TT5.

Figure 4.12 shows the results of twin analysis for RC2. In the Y-Z section, it was analyzed that four variants of TTW (TT1, TT3, TT4 and TT5) occurred unevenly through the thickness direction of the specimen with a total twin area fraction of 0.194. TT1 with the largest fraction of twinned area (0.095) was formed from the L portion to the M portion along the y-axis. TT3 was formed from the U portion to the M portion in an inclining state at a specific tilt angle (~ 60° cw) with respect to the y-axis. TT4 with a very small fraction of twinned area (< 0.001) was formed in the M portion along the y-axis. TT5 was formed from the U portion to the LM portion in an inclining state at a specific tilt angle (~ 60° ccw) with respect to the y-axis.

Furthermore, two double twins (DTs), $\{10\bar{1}1\}-\{10\bar{1}2\}$, were observed within the TBs of CT5 which was nucleated and grew from the L portion to the M portion. The difference in the stress state of the L portion was responsible for the activation of CT5 and the subsequent DTs under the deformation similar to that of V-bending that is induced by an upper die. The development of DTs correlates with immediate cracking that causes premature failure in Mg [57]. The spatial distribution of the relative activity near DTs reveals that pyramidal $\langle \boldsymbol{c}+\boldsymbol{a} \rangle$ slip as well as prismatic $\langle \boldsymbol{a} \rangle$ slip is mainly observed despite a substantially high CRSS value in the plastic deformation at RT. This result indicates that pyramidal $\langle \boldsymbol{c}+\boldsymbol{a} \rangle$ slip releases the localized stress concentration that occurs at the boundaries of DTs, which

delays the formation of cracks.

In the X-Z section, three variants of TTW (TT4, TT5 and TT6) were activated unevenly through the thickness direction of the specimen with a total twin area fraction of 0.825. TT4 with the largest fraction of twinned area (0.810) was formed throughout the specimen (from the L portion to the U portion) in an inclining state at a specific tilt angle (~ 47° ccw) with respect to the x-axis. TT5 was formed throughout the specimen (from the L portion to the U portion) in an inclining state at a specific tilt angle (~ 65° ccw) with respect to the x-axis. TT6 was also formed throughout the specimen (from the L portion to the U portion) in an inclining state at a specific tilt angle (~ 65° ccw) with respect to the x-axis. The commonly observed twin variants in the Y-Z and X-Z sections of RC2 were TT4 and TT5. It is interesting to note that fractures occurred during the Erichsen test due to the geometric shape of the test equipment in the X-Z section of RC2 (Figure 4.13).

Figure 4.14 compares the twinning behaviors that occurred in the five subdivided regions of the (a) Y-Z and (b) X-Z sections for orientation B (IE = 6.8 mm). A majority of the TTW variants in the Y-Z section existed throughout RA, RB1 and RC2. This result seemed due to the opposite strain gradient through the thickness direction. In other words, the TTWs were concentrated in the regions where the ε_{xx} component was positive and the ε_{yy} component was negative. The most important observation here is that most TBs were nucleated at the free surface of deformed specimen and tended to propagate into the matrix. In order to accommodate the initial external strain of the Erichsen test, shear deformation occurred in the basal $\langle \boldsymbol{a} \rangle$ slip system as well as in the TTW system. Accumulation of shear deformation tended to create small irregularities in the free surface of deformed specimen. As a result, it is believed that the stress concentration occurring at these small

irregularities during deformation provided the nucleation site for the TBs. Analysis of the TTW behavior in the X-Z section quantitatively shows that the TBs in RA, RB, and RC1 developed mainly in the lower portion of the deformed specimen and the TBs in RC2 developed mainly in the upper portion of the deformed specimen. This result can be explained by the distribution of the strain components, as demonstrated in the Y-Z section. The ε_{yy} component in a region where TBs are observed has a positive value that is favorable for the nucleation of TBs, while the ε_{xx} component has a very low value in the same region of a deformed specimen. The spatial distribution of the relative activity of the TTW provided a good explanation for the location of the TTW that is observed experimentally in the deformed specimen.

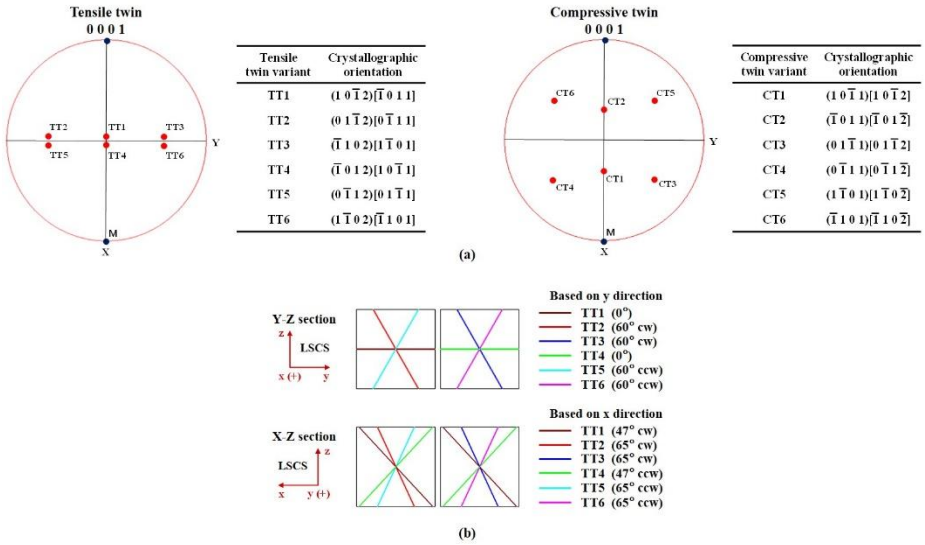

Figure 4.6 (a) TTW and CTW variants with their corresponding Miller indices for the initial crystallographic orientation and (b) geometrical calculation of TTW traces occurring in the Y-Z and X-Z sections of orientation B (IE = 2.0, 4.0 and 6.8 mm).

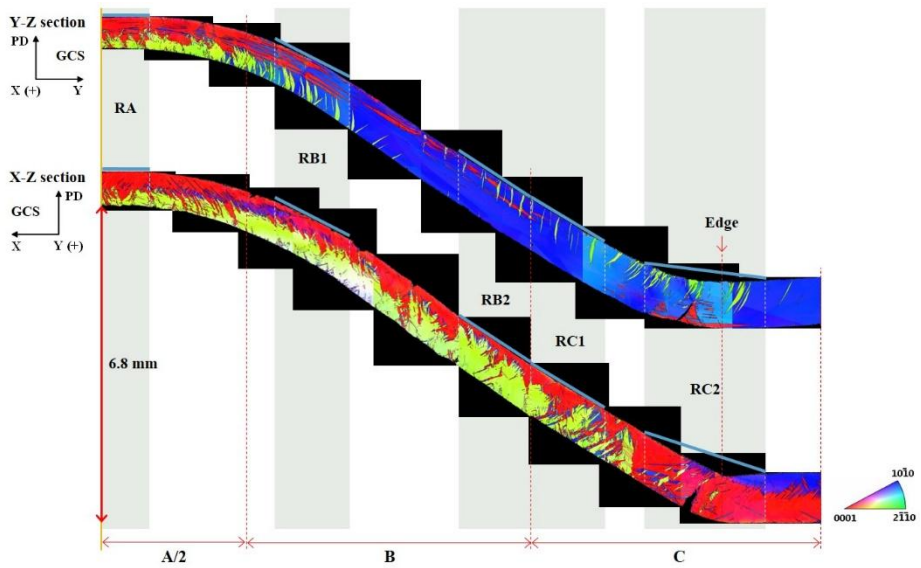

Figure 4.7 The PD(//Z)-inverse pole figure (PD-IPF) maps in the Y-Z and X-Z sections (corresponding to the right half of the schematic diagram) of orientation B (IE = 6.8 mm).

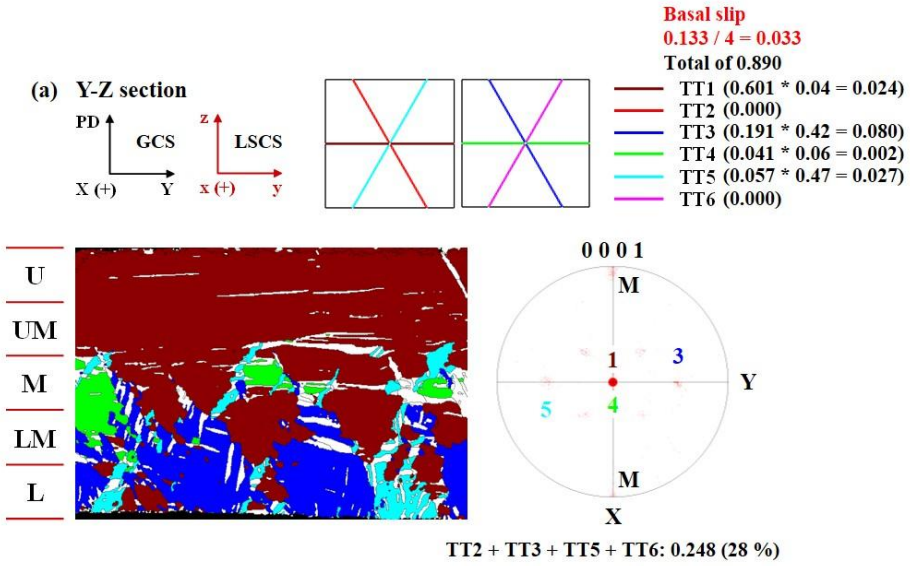

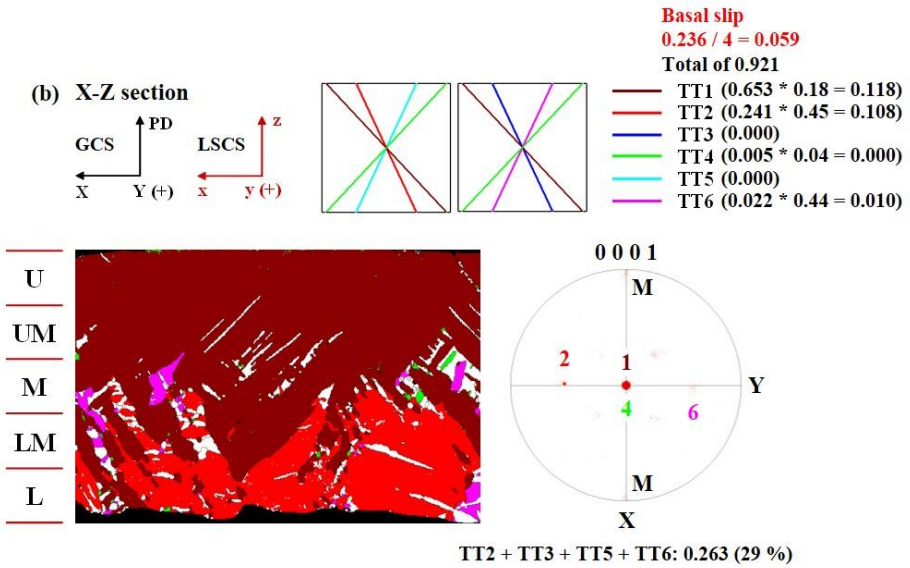

Figure 4.8 Twin analysis of RA in the (a) Y-Z and (b) X-Z sections of orientation B (IE = 6.8 mm).

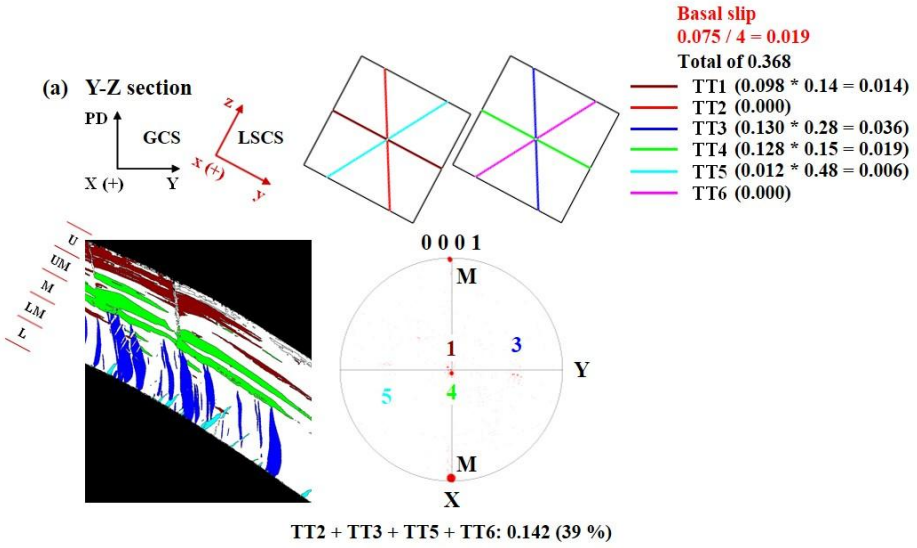

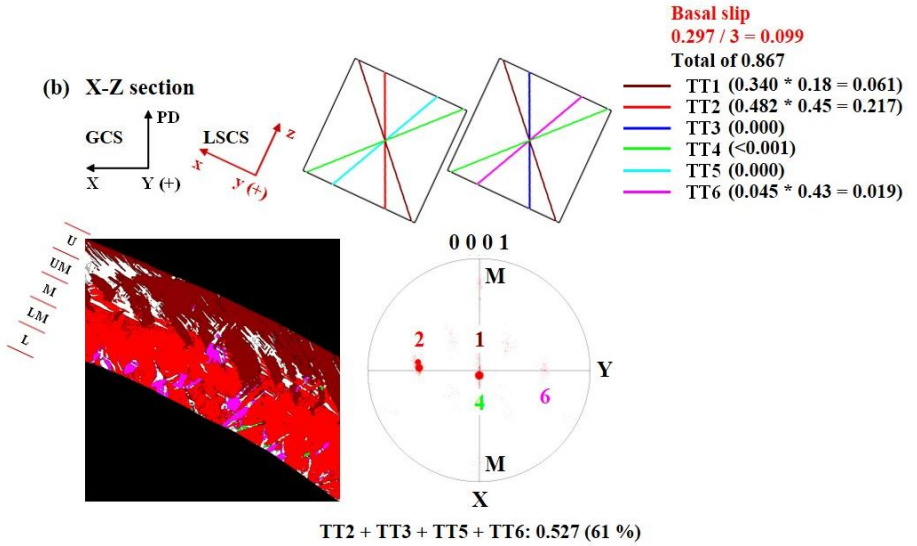

Figure 4.9 Twin analysis of RB1 in the (a) Y-Z and (b) X-Z sections of orientation B (IE = 6.8 mm).

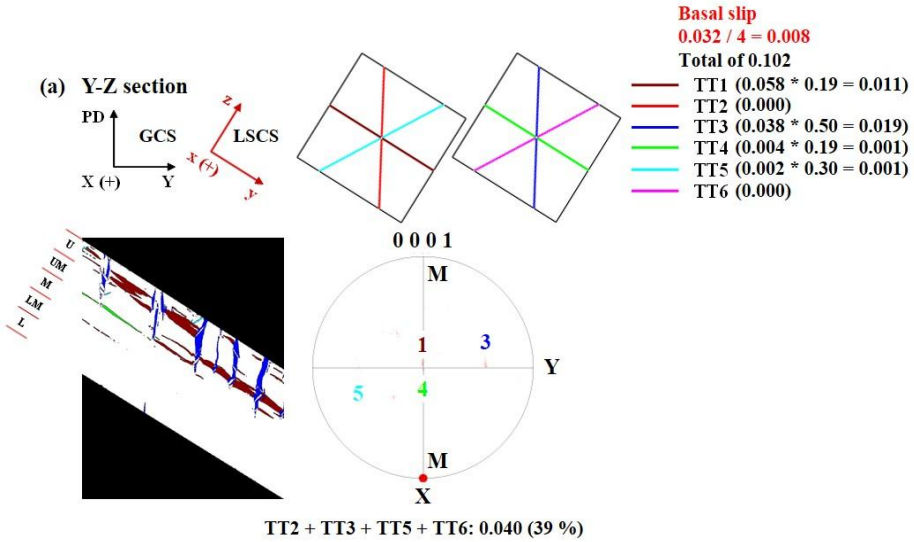

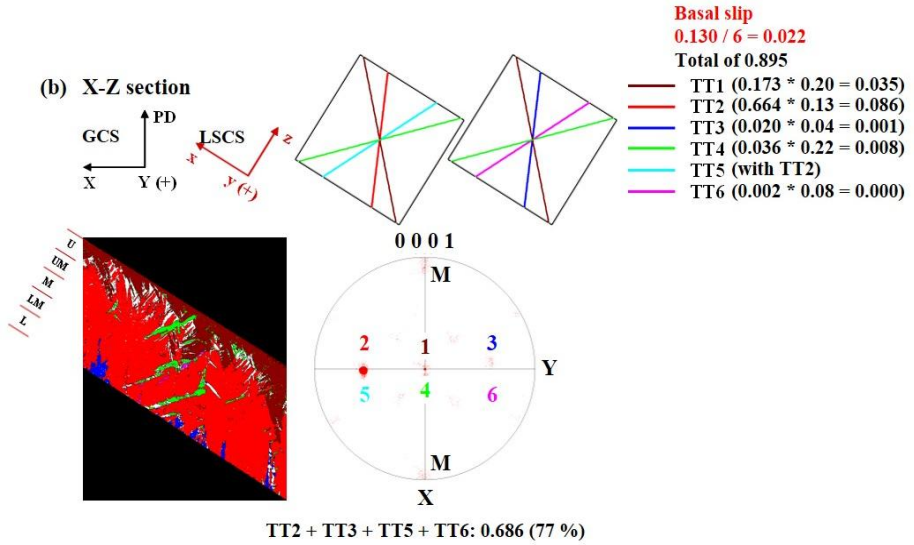

Figure 4.10 Twin analysis of RB2 in the (a) Y-Z and (b) X-Z sections of orientation B (IE = 6.8 mm).

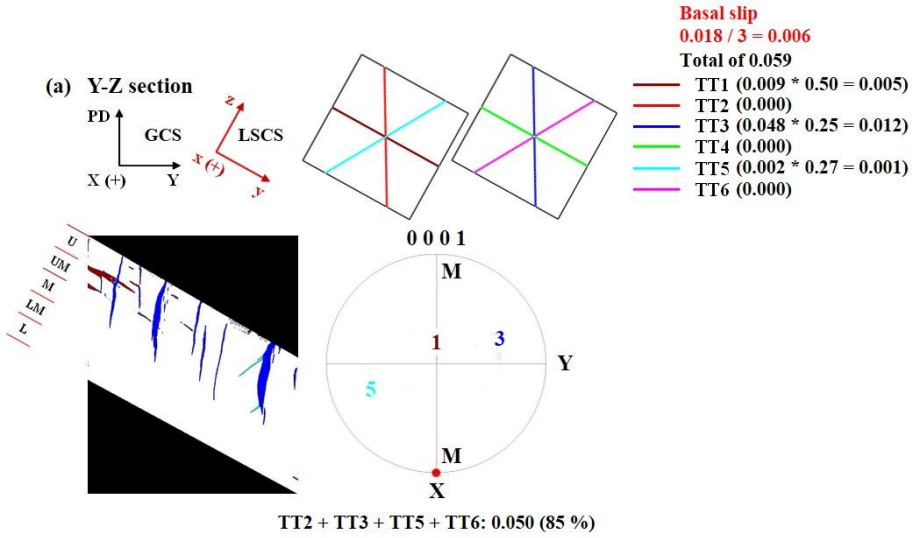

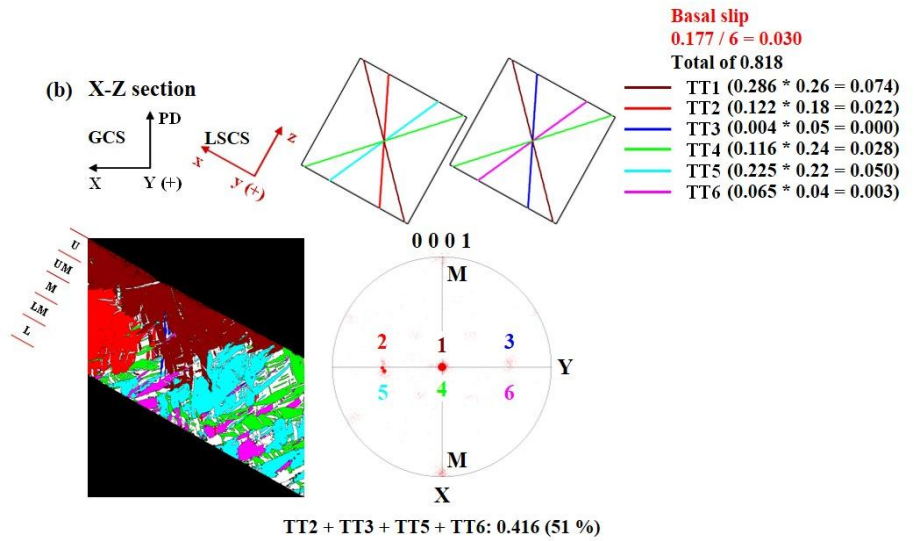

Figure 4.11 Twin analysis of RC1 in the (a) Y-Z and (b) X-Z sections of orientation B (IE = 6.8 mm).

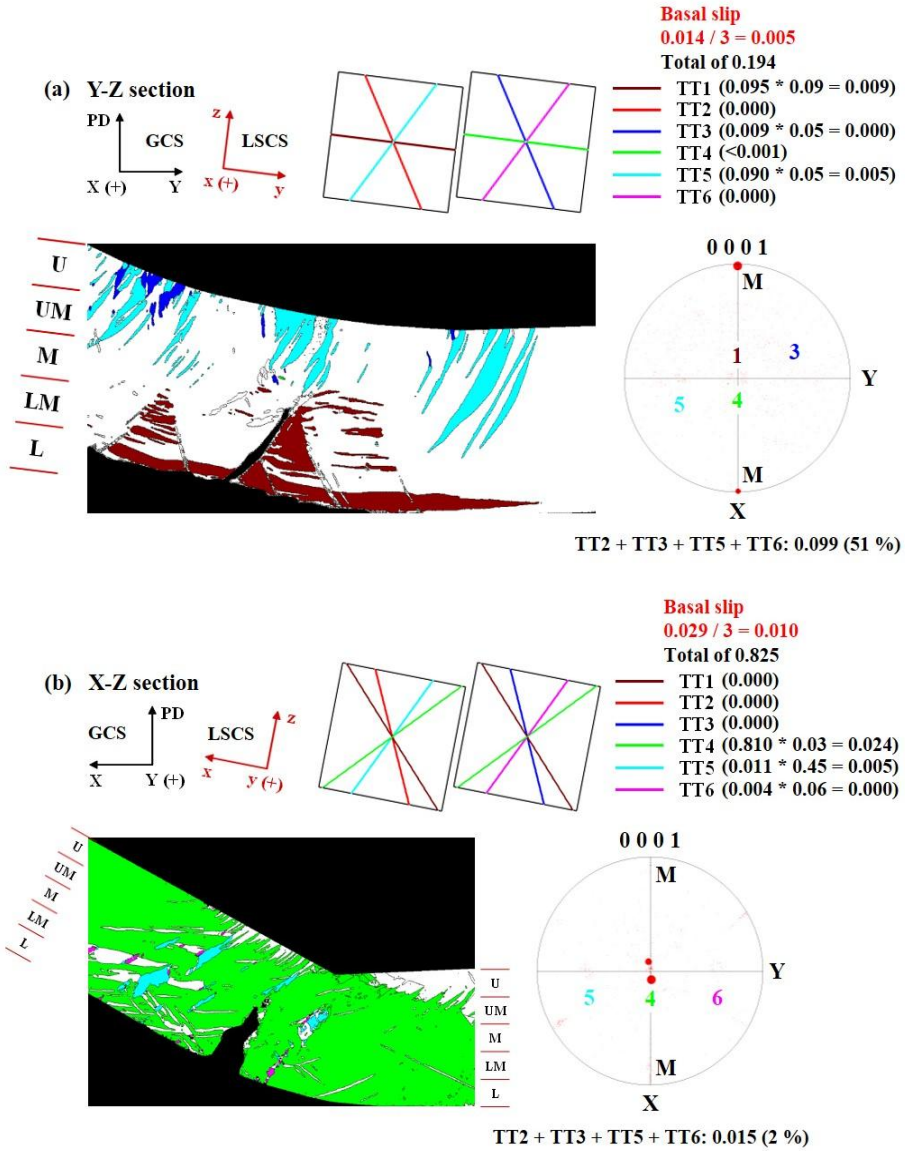

Figure 4.12 Twin analysis of RC2 in the (a) Y-Z and (b) X-Z sections of orientation B (IE = 6.8 mm).

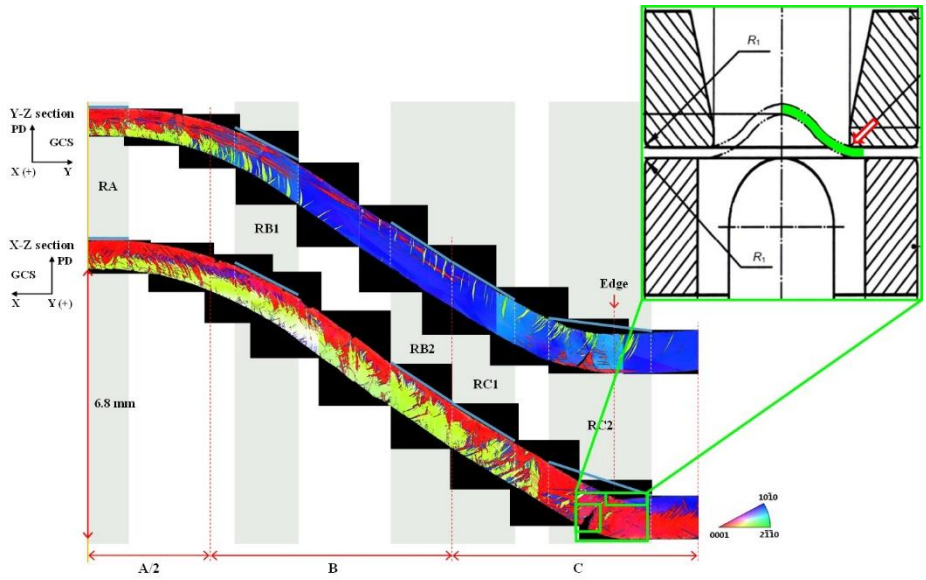

Figure 4.13 Fractures occurred during the Erichsen test due to the geometric shape of the test equipment in the X-Z section of RC2 for orientation B (IE = 6.8 mm).

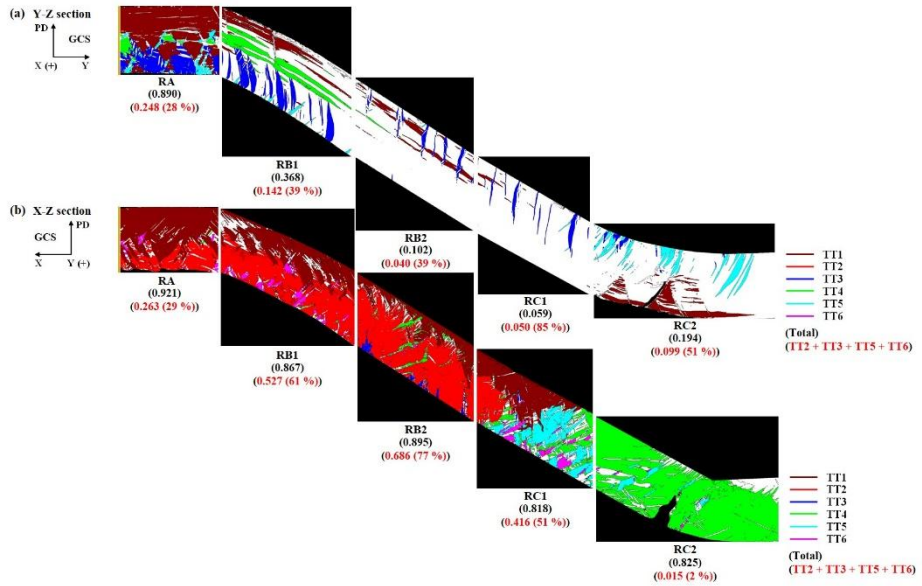

Figure 4.14 A comparison of the five subdivided regions in the (a) Y-Z and (b) X-Z sections of orientation B (IE = 6.8 mm).

4.2 Results and discussion (Orientation B (IE = 4.0 mm))

4.2.1 Erichsen test simulation using CPFEM

In the case of the Erichsen test, the specimen is subjected to a non-uniform deformation history in the plane and thickness directions of the specimen. Furthermore, since the anisotropy of single crystal specimens is so strong, the non-uniformity of deformation in a deformed specimen becomes much more intense, which necessitates an understanding of the non-uniformity of deformation using simulation techniques such as CPFEM. When the PD is parallel to the $[1\ 0\ \bar{1}\ 0]$ direction, the initial crystallographic orientation of a Mg single crystal during the Erichsen test has the orientation relationship of 90° between PD and c-axis, which can be expressed as (ϕ_1, Φ, ϕ_2) = (-90°, 90°, 60°) in Euler space, as described in Figure 4.15(a). The results of the Erichsen test at RT in Figure 4.15(b) show that plastic anisotropy induced an asymmetrically deformed dome shape with respect to the center of both the top and bottom of the deformed specimen under a punch stroke with an IE of 4.0 mm. Furthermore, in order to systematically investigate the twinning behavior and deformation mechanisms during the Erichsen test, the deformed specimen was equally divided into three distinct regions (L_A = L_B = L_C). The three distinct regions are defined as follows. Region A (RA) is the area near the center of the deformed specimen, and is the point at which severe biaxial strain (or stress) occurs during an Erichsen test. Region B (RB) is the intermediate area between the center and the circumference of the deformed specimen. Region C (RC) is the area of the circumference of the deformed specimen, and it the point at which an upper die imposes normal pressure during an Erichsen test.

CPFEM simulation can identify the spatial distribution of strain components, the relative activities of deformation modes and the V^{acc} of the twin variants developed in the three distinct regions during the Erichsen test. Figure 4.16 shows the spatial distribution of the strain components, the relative activities of the deformation modes and the V^{acc} of the twin variants that developed on the top-surface of the deformed specimen. The strain components generated in the Mg single crystal specimen were symmetrically distributed with respect to the center of the specimen, as shown in Figure 4.16(a). In particular, ε_{xx} exhibited a considerable strain gradient in the X direction. It was interesting to note the large difference between maximum ε_{xx} (= 0.122) and maximum ε_{yy} (= 0.033) components at the center of the deformed Mg single crystal. The deformation behavior in this region deviates significantly from equi-biaxial deformation. As shown in Figure 4.16(b), the primary deformation mode in the RA and RB is TTW, and the primary deformation mode in the RC is basal $\langle \boldsymbol{a} \rangle$ slip. It is interesting to note that the V^{acc} of twin variants on the top-surface corresponded mostly to the region of negative ε_{yy}. Among the six twin variants, TT2, TT3, TT5 and TT6 were mainly activated on the circumferential area of the top-surface (Figure 4.16(b)).

Figure 4.17 shows the spatial distribution of strain components, the relative activities of deformation modes, and the V^{acc} of twin variants that had developed on the bottom-surface. The strain components at the bottom-surface of the deformed Mg single crystal were also symmetrically distributed with respect to the center of the specimen, where ε_{xx} and ε_{yy} had positive and negative values, respectively, as shown in Figure 4.17(a). As shown in Figure 4.17(b), the basal $\langle \boldsymbol{a} \rangle$ slip acted as the primary deformation mode,

except for one side from the specimen center parallel to the X-axis, for which the primary deformation mode was TTW. The non-basal slip systems were weakly activated only at the edge of the specimen in the RC parallel to the Y-axis. Figures 4.18 and 4.19 show the CPFEM results for strain components, the relative activity of deformation modes, and the V^{acc} of twin variants that developed on the Y-Z and X-Z sections, respectively. It is recently reported that, due to the orthotropic texture, the stress state through the thickness direction in polycrystalline Mg is also inhomogeneous during the Erichsen test at RT [20]. The spatial distributions of ε_{xx} and ε_{yy} in the RA indicates that biaxial tensile strain is applied along both x and y directions in the upper portion, while tensile and compressive strains are applied in the x and y directions in the lower portion. The spatial distribution of ε_{yy} that developed on the Y-Z section (Figure 4.18(a)) indicated that tensile strain was applied to the upper portion of RA and to the lower portion of RC, while compressive strain was applied to the lower portion of RA and to the upper portion of RC. On the other hand, the spatial distribution of ε_{yy} that developed on the X-Z section (Figure 4.19(a)) indicates that tensile strain was applied to the upper portion of RA while compressive strain was mostly applied to the lower portions of both RA and RB. It is noteworthy that the ε_{yy} that had developed on the X-Z section was almost zero through the thickness direction at the dome edge of RC, meaning that this geometrically approximated plain-strain conditions. On the other hand, considering the strain components observed with the Y-Z section at the dome edge of the RC, the deformation behavior of this region seemed similar to that obtained in the V-bending test [18]. In other words, the outer and inner portions of RC are considered as tension and compression zones, respectively. Figures 4.18(b) and 4.19(b) show the V^{acc}

of the TTW variants in the Y-Z and X-Z sections, respectively. In the RA, regardless of section, the values for V^{acc} of the TT1 and TT4 in the upper portion were relatively higher than those in the lower portion, while the values for V^{acc} of the TT2, TT3, TT5 and TT6 in the lower portion were relatively higher than those in the upper portion. This behavior can be attributed to tensile deformation in the y direction in this portion during the Erichsen test. Based on the experimental results, this will be discussed in more detail in Section 4.2.2. In the RB, the V^{acc} of the TT2 and TT5 was negligible in the Y-Z section, and the V^{acc} of the TT2, TT3, TT5 and TT6 at the bottom of the specimen in the X-Z section was relatively higher than that of the other twin variants. This behavior seemed due to the tensile strain in the x direction and to the compressive strain in the y direction in the lower portion of the X-Z section. In the RC, the V^{acc} at the upper portion of the specimen in the Y-Z section was relatively higher than that at the lower portion because the strain was small in the x direction but compressive strain was acting in the y direction in this portion. On the other hand, the value for V^{acc} was low at the center of the specimen in the X-Z section despite a high relative activity of twin, which can be attributed to a relatively low level of deformation in RC during the Erichsen test compared with that in both RA and RB.

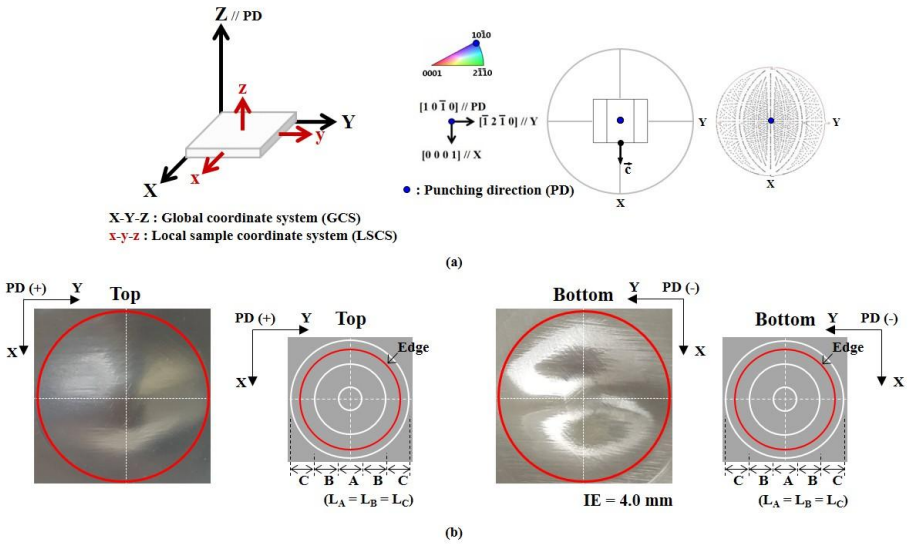

Figure 4.15 (a) Initial crystallographic orientation and (b) Erichsen test results of orientation B (IE = 4.0 mm).

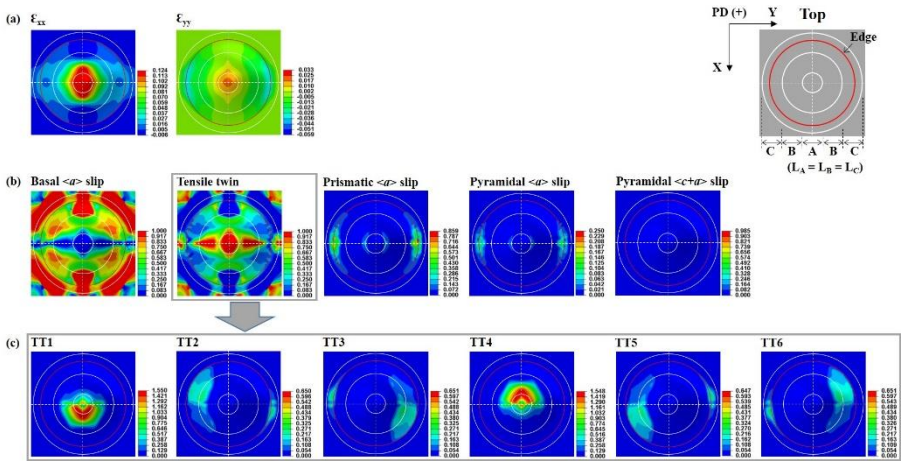

Figure 4.16 CPFEM results for the top-surface of orientation B (IE = 4.0 mm) after the Erichsen simulation: spatial distribution of (a) strain components, (b) relative activities of deformation modes, and (c) accumulated volume fraction of TTW variants.

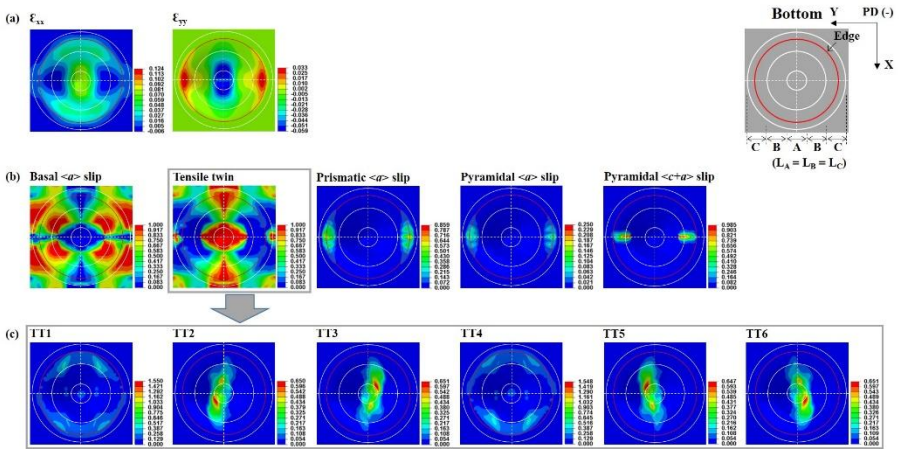

Figure 4.17 CPFEM results for the bottom-surface of orientation B (IE = 4.0 mm) after the Erichsen simulation: spatial distribution of (a) strain components, (b) relative activities of deformation modes, and (b) accumulated volume fraction of TTW variants.

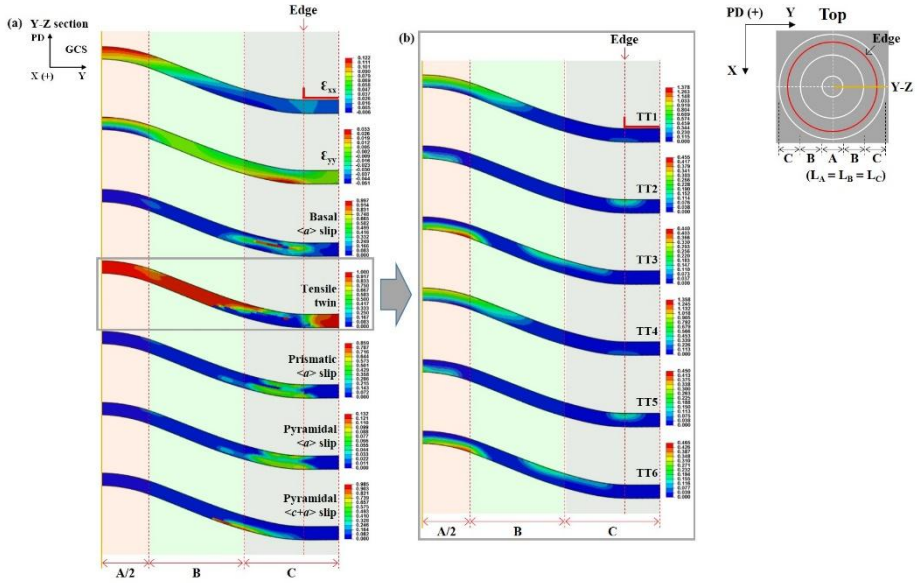

Figure 4.18 CPFEM results for the Y-Z section of orientation B (IE = 4.0 mm) after the Erichsen simulation: spatial distribution of (a) strain components, relative activities of deformation modes, and (b) accumulated volume fraction of TTW variants.

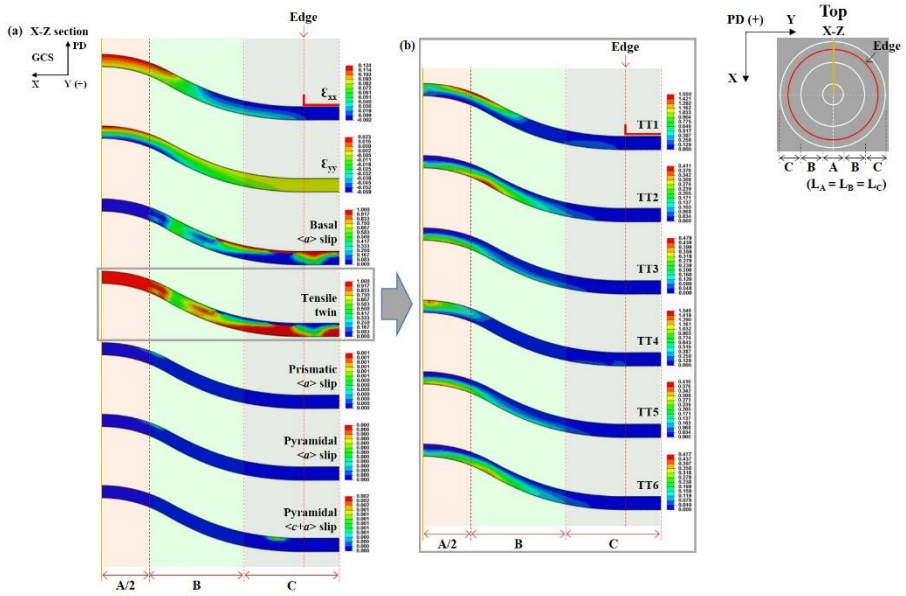

Figure 4.19 CPFEM results for the X-Z section of orientation B (IE = 4.0 mm) after the Erichsen simulation: spatial distribution of (a) strain components, relative activities of deformation modes and (b) accumulated volume fraction of TTW variants.

4.2.2 Characterization of TBs using EBSD analysis

Figure 4.20(a) is a schematic representation of the Y-Z and X-Z sections after the Erichsen test. Analysis of the microtexture evolutions in RB was divided into two portions: RB1 adjacent to RA and RB2 adjacent to RC. The microtexture evolution in RC were also analyzed in two portions: RC1 adjacent to RB and RC2 adjacent to the dome edge. The PD(//Z)-inverse pole figure (PD-IPF) maps of the two cross-sections appear in Figure 4.20(b), and corresponds to the right-half of the schematic representation in Figure 4.20(a). The crystal orientation of the deformed specimen was corrected by rotation, which was based on the GCS to ease analysis. Microtexture analysis of the cross-sections revealed that the heterogeneous evolution of deformation twinning was developed in a heterogeneous manner throughout the deformed specimen, exhibiting the differences in surface slopes along X and Y directions.

Microtexture analysis combined with the TTW traces effectively explained the twinning behavior occurring in a deformed Mg single crystal during the Erichsen test. LSCS was used to describe the spatial morphology and variant type of TBs developed in the Y-Z and X-Z sections. Moreover, the thickness of the observation area was equally divided into five portions to explain the twinning behavior based on LSCS: upper (U), upper-middle (UM), middle (M), lower-middle (LM), and lower (L). The color used to draw the TTW traces was also applied to the TBs to more easily identify the corresponding variants.

Figure 4.21 shows the results of the twin analysis for RA. In the Y-Z section, four variants of TTW (TT1, TT3, TT4 and TT5) occurred unevenly through the thickness direction of the deformed specimen with a total twin

area fraction of 0.510. TT1 with the largest fraction of twinned area (0.368) was formed throughout the specimen (from the U portion to the L portion) along the y-axis. TT3 was formed from the L portion to the M portion in an inclining state at a specific tilt angle (~ 60° cw) with respect to the y-axis. TT4 was formed throughout the specimen (from the U portion to the L portion) along the y-axis. TT5 was formed from the L portion to the M portion in an inclining state at a specific tilt angle (~ 60° ccw) with respect to the y-axis. In the X-Z section, four variants of TTW (TT1, TT2, TT4 and TT6) were activated unevenly through the thickness direction of the specimen with a total twin area fraction of 0.514. TT1 with the largest fraction of twinned area (0.285) was formed throughout the specimen (from the U portion to the L portion) in an inclining state at a specific tilt angle (~ 47° cw) with respect to the x-axis. TT2 was formed from the L portion to the M portion in an inclining state at a specific tilt angle (~ 65° cw) with respect to the x-axis. TT4 was formed throughout the specimen (from the U portion to the L portion) in an inclining state at a specific tilt angle (~ 47° ccw) with respect to the x-axis. TT6 was formed from the L portion to the M portion in an inclining state at a specific tilt angle (~ 65° ccw) with respect to the x-axis. The commonly observed twin variants in the Y-Z and X-Z sections of RA were TT1 and TT4.

Figure 4.22 shows the results of the twin analysis for RB1. It is found that the deformed specimen observed on the Y-Z section is placed in a state with a ~ 14° surface slope relative to the Y-axis, whereas the deformed specimen on the X-Z section has a surface slope of ~ 20° with respect to the X-axis. In the Y-Z section, only TT1 occurred unevenly through the thickness direction of the deformed specimen with a twin area fraction of 0.022. TT1 was formed from the U portion to the LM portion along the y-axis. In the X-Z section, five variants of TTW (TT1, TT2, TT4, TT5 and TT6) were activated

unevenly through the thickness direction of the specimen with a total twin area fraction of 0.528. TT1 was formed throughout the specimen (from the U portion to the L portion) in an inclining state at a specific tilt angle (~ 47° cw) with respect to the x-axis. TT2 with the largest fraction of twinned area (0.273) was formed throughout the specimen (from the L portion to the U portion) in an inclining state at a specific tilt angle (~ 65° cw) with respect to the x-axis. TT4 was formed from the L portion to the UM portion in an inclining state at a specific tilt angle (~ 47° ccw) with respect to the x-axis. TT5 was formed from the L portion to the M portion in an inclining state at a specific tilt angle (~ 65° ccw) with respect to the x-axis. TT6 was formed throughout the specimen (from the L portion to the U portion) in an inclining state at a specific tilt angle (~ 65° ccw) with respect to the x-axis. TT1 was the commonly observed twin variant in the Y-Z and X-Z sections of RB1.

Figure 4.23 shows the results of the twin analysis for RB2. It is found that the deformed specimen observed on the Y-Z section is placed in a state with a ~ 16° surface slope relative to the Y-axis, whereas the deformed specimen on the X-Z section has a surface slope of ~ 12° with respect to the X-axis. In the Y-Z section, two variants of TTW (TT3 and TT5) occurred unevenly through the thickness direction of the deformed specimen with a total twin area fraction of 0.005. TT3 with the largest fraction of twinned area (0.005) was formed from the U portion to the UM portion in an inclining state at a specific tilt angle (~ 60° cw) with respect to the y-axis. TT5 with a very small fraction of twinned area (< 0.001) was formed in the U portion in an inclining state at a specific tilt angle (~ 60° ccw) with respect to the y-axis. In the X-Z section, all the six variants of TTW were activated unevenly through the thickness direction of the specimen with a total twin area fraction of 0.198. TT1 was formed throughout the specimen (from the L portion to the U portion)

in an inclining state at a specific tilt angle (~ 47° cw) with respect to the x-axis. TT2 with the largest fraction of twinned area (0.131) was formed throughout the specimen (from the L portion to the U portion) in an inclining state at a specific tilt angle (~ 65° cw) with respect to the x-axis. TT3 with a very small fraction of twinned area (~ 0.001) was formed in the L portion in an inclining state at a specific tilt angle (~ 65° cw) with respect to the x-axis. TT4 was formed throughout the specimen (from both the U portion and the L portion) in an inclining state at a specific tilt angle (~ 47° ccw) with respect to the x-axis. TT5 was formed from the L portion to the M portion in an inclining state at a specific tilt angle (~ 65° ccw) with respect to the x-axis. TT6 with a very small fraction of twinned area (~ 0.001) was formed in the L portion in an inclining state at a specific tilt angle (~ 65° ccw) with respect to the x-axis. The commonly observed twin variants in the Y-Z and X-Z sections of RB2 were TT3 and TT5.

Figure 4.24 shows the results of the twin analysis for RC1. The Y-Z section exhibited a surface slope of ~ 15° based on the Y-axis, whereas the X-Z section has a surface slope of ~ 3° based on the X-axis. In the Y-Z section, only TT3 occurred unevenly through the thickness direction of the deformed specimen with a twin area fraction of 0.008. TT3 was formed from the U portion to the UM portion in an inclining state at a specific tilt angle (~ 60° cw) with respect to the y-axis. In the X-Z section, four variants of TTW (TT1, TT2, TT4 and TT6) were activated unevenly through the thickness direction of the specimen with a total twin area fraction of 0.271. TT1 with the largest fraction of twinned area (0.140) was formed throughout the specimen (from both the U portion and the L portion) in an inclining state at a specific tilt angle (~ 47° cw) with respect to the x-axis. TT2 with a very small fraction of twinned area (~ 0.001) was formed from the L portion to the LM portion in an

inclining state at a specific tilt angle (~ 65° cw) with respect to the x-axis. TT4 was formed from the L portion to the UM portion in an inclining state at a specific tilt angle (~ 47° ccw) with respect to the x-axis. TT6 was formed from the L portion to the M portion in an inclining state at a specific tilt angle (~ 65° ccw) with respect to the x-axis. No twin variant was commonly observed in the Y-Z and X-Z sections of RC1.

Figure 4.25 shows the results of twin analysis for RC2. In the Y-Z section, it was analyzed that four variants of TTW (TT1, TT3, TT4 and TT5) occurred unevenly through the thickness direction of the specimen with a total twin area fraction of 0.062. TT1 was formed from the L portion to the M portion along the y-axis. TT3 was formed from the U portion to the M portion in an inclining state at a specific tilt angle (~ 60° cw) with respect to the y-axis. TT4 was formed from the L portion to the LM portion as well as in the U portion along the y-axis. TT5 with the largest fraction of twinned area (0.042) was formed from the U portion to the M portion in an inclining state at a specific tilt angle (~ 60° ccw) with respect to the y-axis.

Furthermore, two double twins (DTs), $\{10\bar{1}1\}-\{10\bar{1}2\}$, were observed within the TBs of CT5 which was nucleated and grew from the L portion to the M portion. The difference in the stress state of the L portion was responsible for the activation of CT5 and the subsequent DTs under the deformation similar to that of V-bending that is induced by an upper die. The development of DTs correlates with immediate cracking that causes premature failure in Mg [57]. The spatial distribution of the relative activity near DTs reveals that pyramidal $\langle \boldsymbol{c}+\boldsymbol{a} \rangle$ slip as well as prismatic $\langle \boldsymbol{a} \rangle$ slip is mainly observed despite a substantially high CRSS value in the plastic deformation at RT. This result indicates that pyramidal $\langle \boldsymbol{c}+\boldsymbol{a} \rangle$ slip releases the localized stress concentration that occurs at the boundaries of DTs, which

delays the formation of cracks.

In the X-Z section, four variants of TTW (TT1, TT3, TT4 and TT6) were activated unevenly through the thickness direction of the specimen with a total twin area fraction of 0.165. TT1 was formed from the L portion to the LM portion as well as from the U portion to the UM portion in an inclining state at a specific tilt angle (~ 47° cw) with respect to the x-axis. TT3 with a very small fraction of twinned area (< 0.001) was formed in the L portion in an inclining state at a specific tilt angle (~ 65° cw) with respect to the x-axis. TT4 with the largest fraction of twinned area (0.149) was formed throughout the specimen (from the L portion to the U portion) in an inclining state at a specific tilt angle (~ 47° ccw) with respect to the x-axis. TT6 with a very small fraction of twinned area (< 0.001) was formed in the L portion in an inclining state at a specific tilt angle (~ 65° ccw) with respect to the x-axis. The commonly observed twin variants in the Y-Z and X-Z sections of RC2 were TT1, TT3 and TT4.

Figure 4.26 compares the twinning behaviors that occurred in the five subdivided regions of the (a) Y-Z and (b) X-Z sections for orientation B (IE = 4.0 mm). A majority of the TTW variants in the Y-Z section existed throughout RA, RB1 and RC2. This result seemed due to the opposite strain gradient through the thickness direction. In other words, the TTWs were concentrated in the regions where the ε_{xx} component was positive and the ε_{yy} component was negative. The most important observation here is that most TBs were nucleated at the free surface of deformed specimen and tended to propagate into the matrix. In order to accommodate the initial external strain of the Erichsen test, shear deformation occurred in the basal $\langle \boldsymbol{a} \rangle$ slip system as well as in the TTW system. Accumulation of shear deformation tended to create small irregularities in the free surface of deformed specimen.

As a result, it is believed that the stress concentration occurring at these small irregularities during deformation provided the nucleation site for the TBs. Analysis of the TTW behavior in the X-Z section quantitatively shows that the TBs in RA, RB, and RC1 developed mainly in the lower portion of the deformed specimen and the TBs in RC2 developed mainly in the upper portion of the deformed specimen. This result can be explained by the distribution of the strain components, as demonstrated in the Y-Z section. The ε_{yy} component in a region where TBs are observed has a positive value that is favorable for the nucleation of TBs, while the ε_{xx} component has a very low value in the same region of a deformed specimen. The spatial distribution of the relative activity of the TTW provided a good explanation for the location of the TTW that is observed experimentally in the deformed specimen.

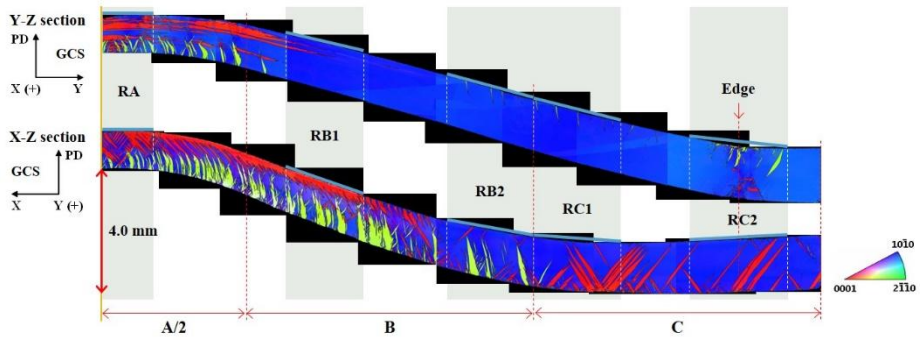

Figure 4.20 The PD(//Z)-inverse pole figure (PD-IPF) maps in the Y-Z and X-Z sections (corresponding to the right half of the schematic diagram) of orientation B (IE = 4.0 mm).

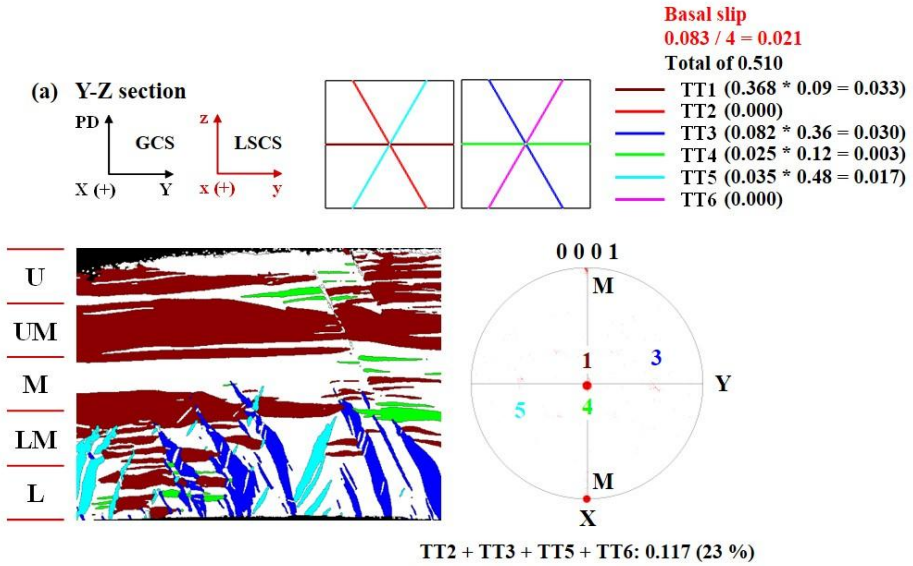

Figure 4.21 Twin analysis of RA in the (a) Y-Z and (b) X-Z sections of orientation B (IE = 4.0 mm).

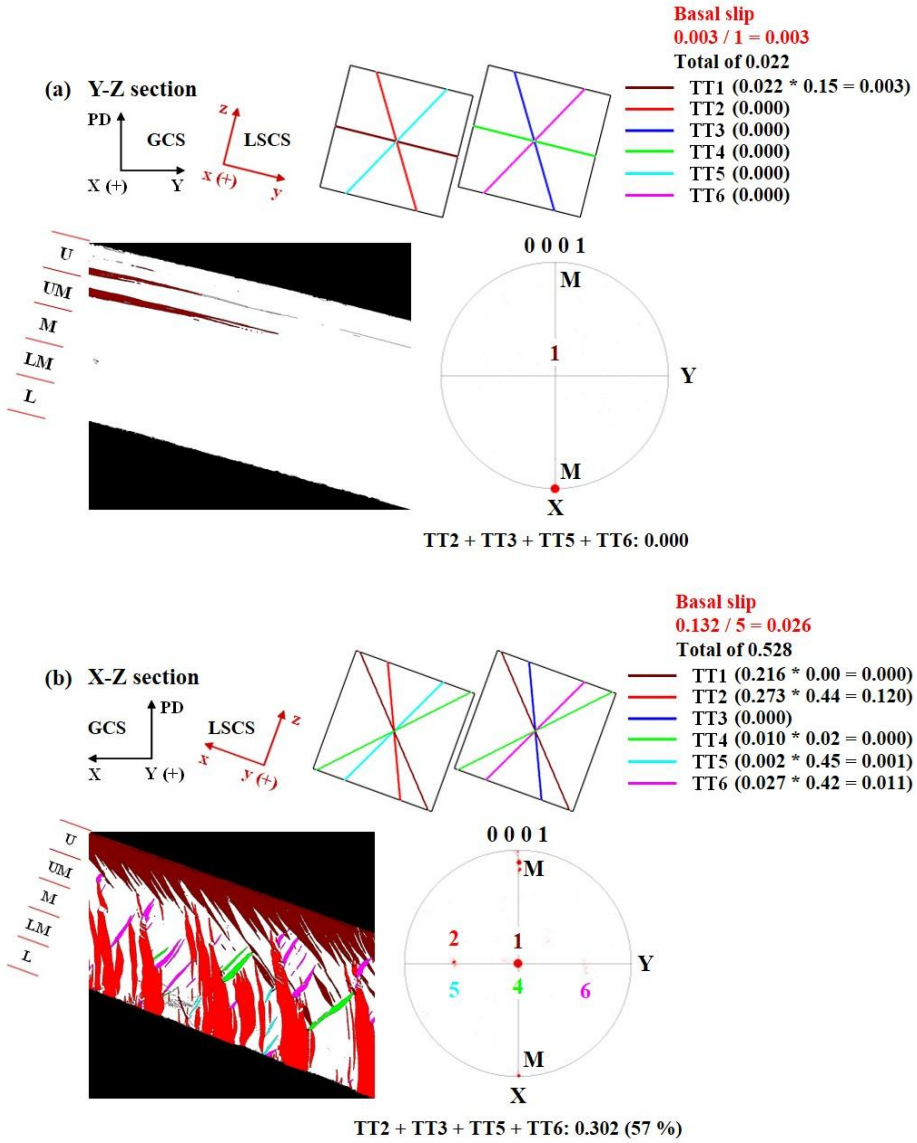

Figure 4.22 Twin analysis of RB1 in the (a) Y-Z and (b) X-Z sections of orientation B (IE = 4.0 mm).

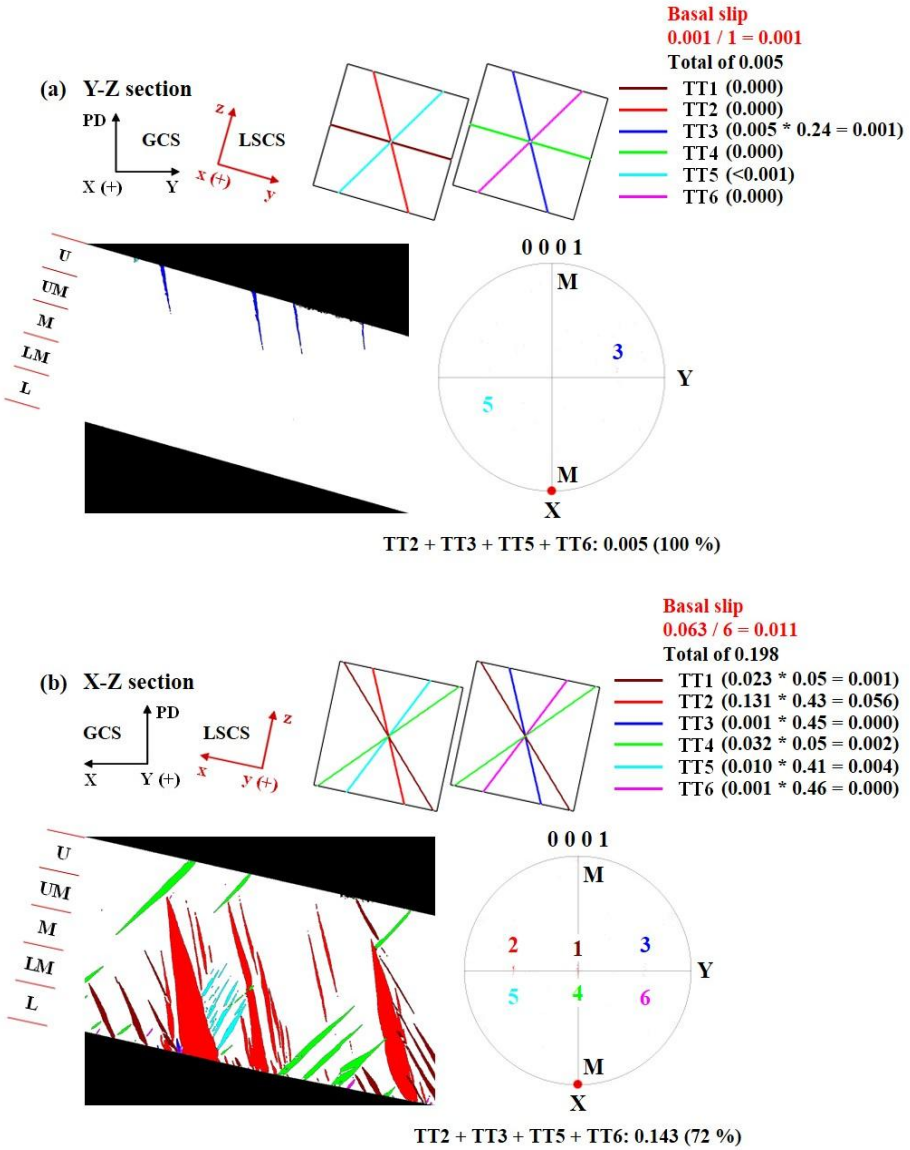

Figure 4.23 Twin analysis of RB2 in the (a) Y-Z and (b) X-Z sections of orientation B (IE = 4.0 mm).

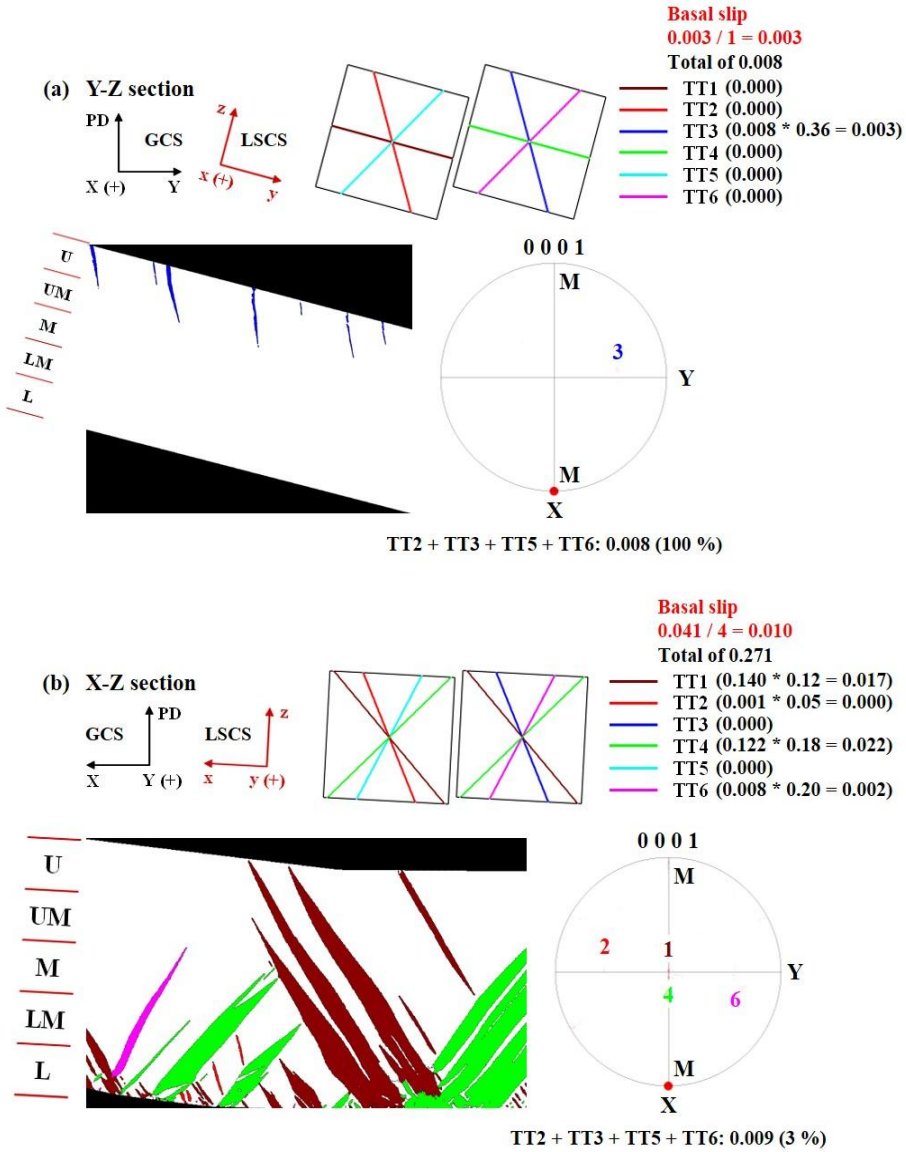

Figure 4.24 Twin analysis of RC1 in the (a) Y-Z and (b) X-Z sections of orientation B (IE = 4.0 mm).

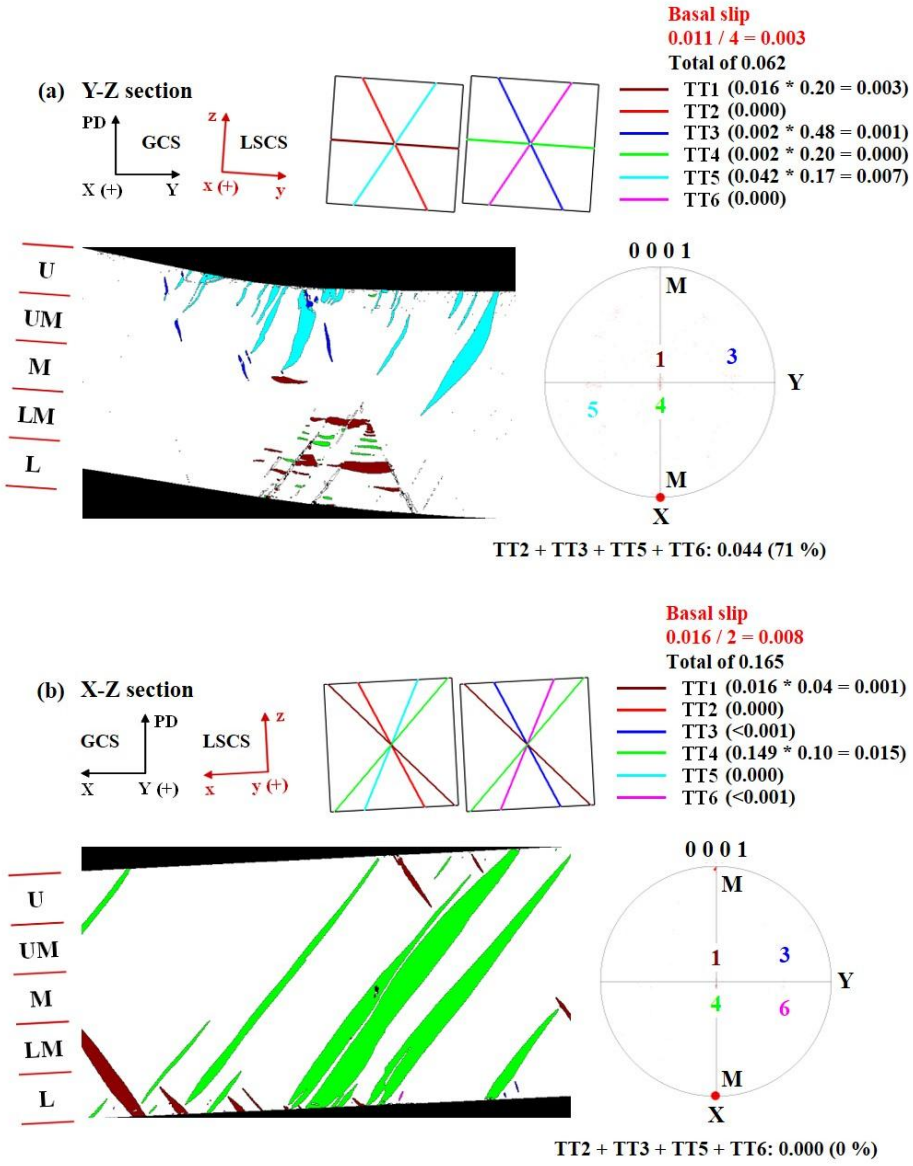

Figure 4.25 Twin analysis of RC2 in the (a) Y-Z and (b) X-Z sections of orientation B (IE = 4.0 mm).

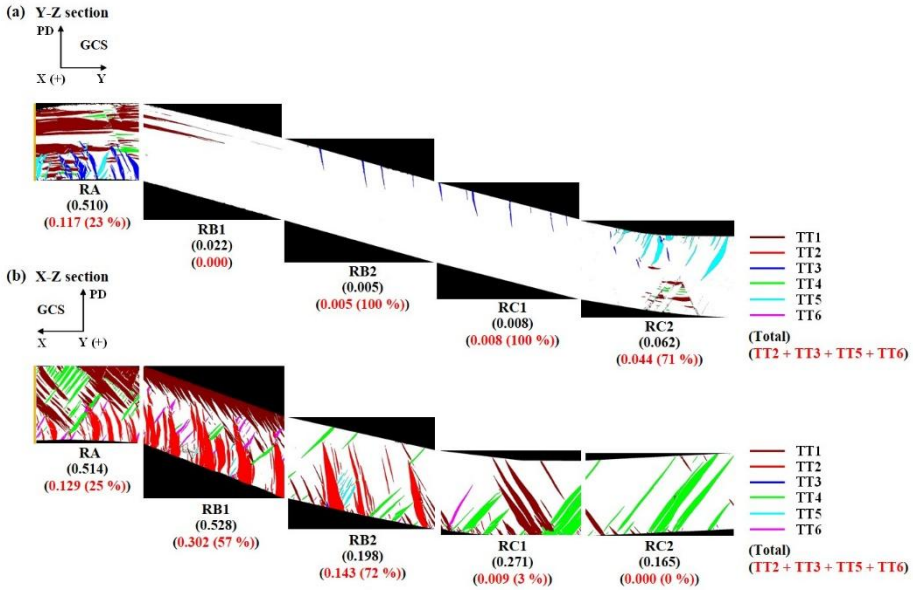

Figure 4.26 A comparison of the five subdivided regions in the (a) Y-Z and (b) X-Z sections of orientation B (IE = 4.0 mm).

4.3 Results and discussion (Orientation B (IE = 2.0 mm))

4.3.1 Erichsen test simulation using CPFEM

In the case of the Erichsen test, the specimen is subjected to a non-uniform deformation history in the plane and thickness directions of the specimen. Furthermore, since the anisotropy of single crystal specimens is so strong, the non-uniformity of deformation in a deformed specimen becomes much more intense, which necessitates an understanding of the non-uniformity of deformation using simulation techniques such as CPFEM. When the PD is parallel to the $[1\ 0\ \bar{1}\ 0]$ direction, the initial crystallographic orientation of a Mg single crystal during the Erichsen test has the orientation relationship of 90° between PD and c-axis, which can be expressed as (ϕ_1, Φ, ϕ_2) = (-90°, 90°, 60°) in Euler space, as described in Figure 4.27(a). The results of the Erichsen test at RT in Figure 4.27(b) show that plastic anisotropy induced an asymmetrically deformed dome shape with respect to the center of both the top and bottom of the deformed specimen under a punch stroke with an IE of 2.0 mm. Furthermore, in order to systematically investigate the twinning behavior and deformation mechanisms during the Erichsen test, the deformed specimen was equally divided into three distinct regions (L_A = L_B = L_C). The three distinct regions are defined as follows. Region A (RA) is the area near the center of the deformed specimen, and is the point at which severe biaxial strain (or stress) occurs during an Erichsen test. Region B (RB) is the intermediate area between the center and the circumference of the deformed specimen. Region C (RC) is the area of the circumference of the deformed specimen, and it the point at which an upper die imposes normal pressure during an Erichsen test.

CPFEM simulation can identify the spatial distribution of strain components, the relative activities of deformation modes and the V^{acc} of the twin variants developed in the three distinct regions during the Erichsen test. Figure 4.28 shows the spatial distribution of the strain components, the relative activities of the deformation modes and the V^{acc} of the twin variants that developed on the top-surface of the deformed specimen. The strain components generated in the Mg single crystal specimen were symmetrically distributed with respect to the center of the specimen, as shown in Figure 4.28(a). In particular, ε_{xx} exhibited a considerable strain gradient in the X direction. It was interesting to note the large difference between maximum ε_{xx} (= 0.070) and maximum ε_{yy} (= 0.026) components at the center of the deformed Mg single crystal. The deformation behavior in this region deviates significantly from equi-biaxial deformation. As shown in Figure 4.28(b), the primary deformation mode in the RA and RB is TTW, and the primary deformation mode in the RC is basal $\langle \boldsymbol{a} \rangle$ slip. It is interesting to note that the V^{acc} of twin variants on the top-surface corresponded mostly to the region of negative ε_{yy}. Among the six twin variants, TT2, TT3, TT5 and TT6 were mainly activated on the circumferential area of the top-surface (Figure 4.28(b)).

Figure 4.29 shows the spatial distribution of strain components, the relative activities of deformation modes, and the V^{acc} of twin variants that had developed on the bottom-surface. The strain components at the bottom-surface of the deformed Mg single crystal were also symmetrically distributed with respect to the center of the specimen, where ε_{xx} and ε_{yy} had positive and negative values, respectively, as shown in Figure 4.29(a). As shown in Figure 4.29(b), the basal $\langle \boldsymbol{a} \rangle$ slip acted as the primary deformation mode,

except for one side from the specimen center parallel to the X-axis, for which the primary deformation mode was TTW. The non-basal slip systems were weakly activated only at the edge of the specimen in the RC parallel to the Y-axis. Figures 4.30 and 4.31 show the CPFEM results for strain components, the relative activity of deformation modes, and the V^{acc} of twin variants that developed on the Y-Z and X-Z sections, respectively. It is recently reported that, due to the orthotropic texture, the stress state through the thickness direction in polycrystalline Mg is also inhomogeneous during the Erichsen test at RT [20]. The spatial distributions of ε_{xx} and ε_{yy} in the RA indicates that biaxial tensile strain is applied along both x and y directions in the upper portion, while tensile and compressive strains are applied in the x and y directions in the lower portion. The spatial distribution of ε_{yy} that developed on the Y-Z section (Figure 4.30(a)) indicated that tensile strain was applied to the upper portion of RA and to the lower portion of RC, while compressive strain was applied to the lower portion of RA and to the upper portion of RC. On the other hand, the spatial distribution of ε_{yy} that developed on the X-Z section (Figure 4.31(a)) indicates that tensile strain was applied to the upper portion of RA while compressive strain was mostly applied to the lower portion of RA. It is noteworthy that the ε_{yy} that had developed on the X-Z section was almost zero through the thickness direction at the dome edge of RC, meaning that this geometrically approximated plain-strain conditions. On the other hand, considering the strain components observed with the Y-Z section at the dome edge of the RC, the deformation behavior of this region seemed similar to that obtained in the V-bending test [18]. In other words, the outer and inner portions of RC are considered as tension and compression zones, respectively. Figures 4.30(b) and 4.31(b) show the V^{acc} of the TTW

variants in the Y-Z and X-Z sections, respectively. In the RA, regardless of section, the values for V^{acc} of the TT1 and TT4 in the upper portion were relatively higher than those in the lower portion, while the values for V^{acc} of the TT2, TT3, TT5 and TT6 in the lower portion were relatively higher than those in the upper portion. This behavior can be attributed to tensile deformation in the y direction in this portion during the Erichsen test. Based on the experimental results, this will be discussed in more detail in Section 4.3.2. In the RB, the V^{acc} of the TT2 and TT5 was negligible in the Y-Z section, and the V^{acc} of the TT2 and TT6 at the bottom of the specimen in the X-Z section was relatively higher than that of the other twin variants. This behavior seemed due to the tensile strain in the x direction and to the compressive strain in the y direction in the lower portion of the X-Z section. In the RC, the V^{acc} at the upper portion of the specimen in the Y-Z section was relatively higher than that at the lower portion because the strain was small in the x direction but compressive strain was acting in the y direction in this portion. On the other hand, the value for V^{acc} was low at the center of the specimen in the X-Z section despite a high relative activity of twin, which can be attributed to a relatively low level of deformation in RC during the Erichsen test compared with that in both RA and RB.

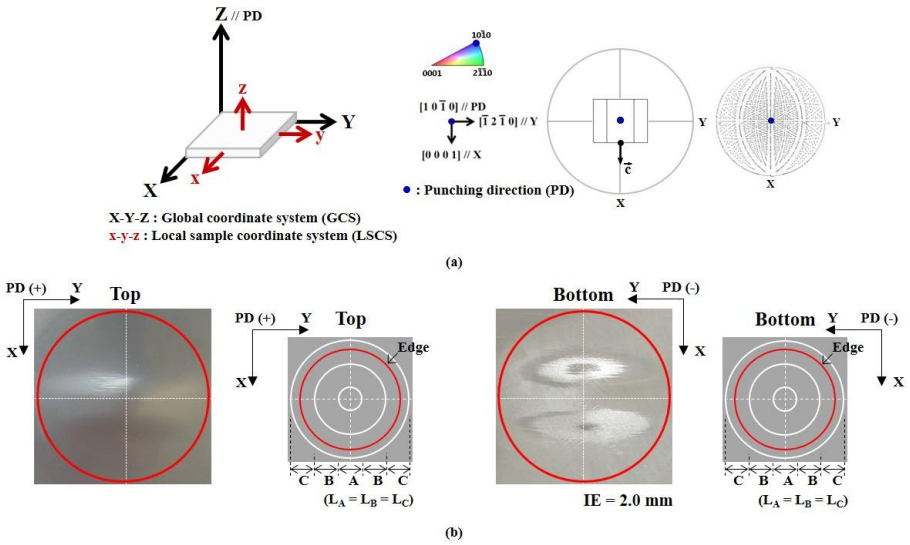

Figure 4.27 (a) Initial crystallographic orientation and (b) Erichsen test results of orientation B (IE = 2.0 mm).

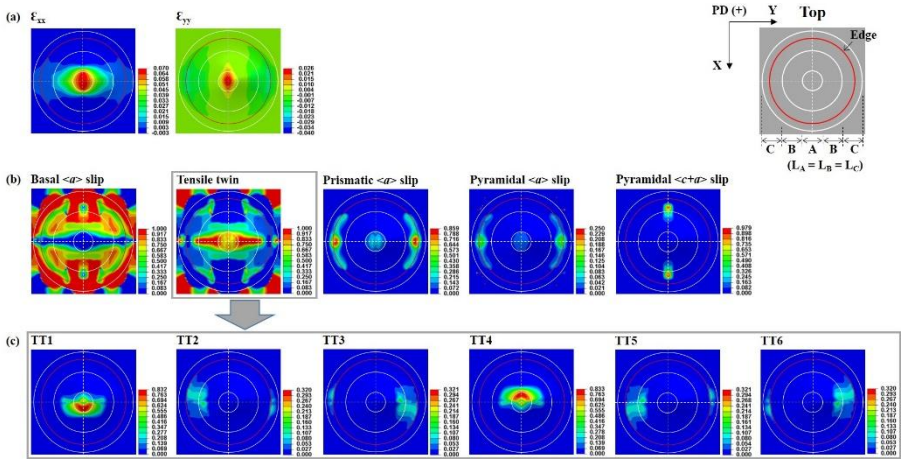

Figure 4.28 CPFEM results for the top-surface of orientation B (IE = 2.0 mm) after the Erichsen simulation: spatial distribution of (a) strain components, (b) relative activities of deformation modes, and (c) accumulated volume fraction of TTW variants.

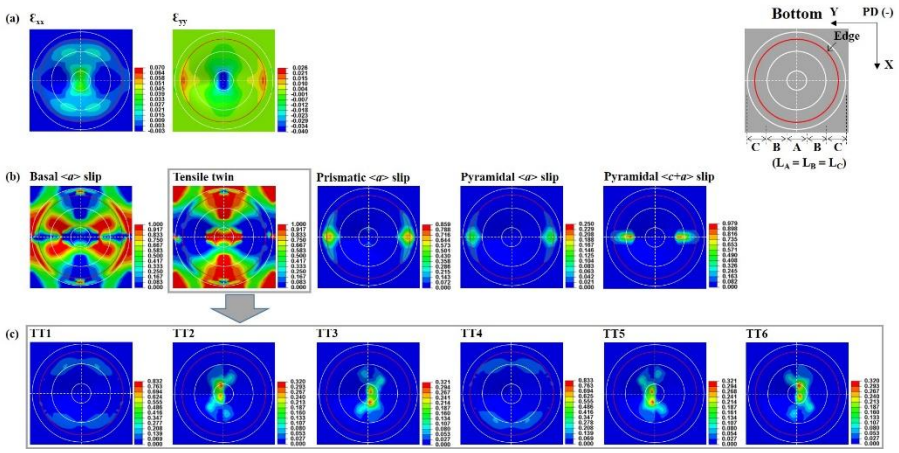

Figure 4.29 CPFEM results for the bottom-surface of orientation B (IE = 2.0 mm) after the Erichsen simulation: spatial distribution of (a) strain components, (b) relative activities of deformation modes, and (b) accumulated volume fraction of TTW variants.

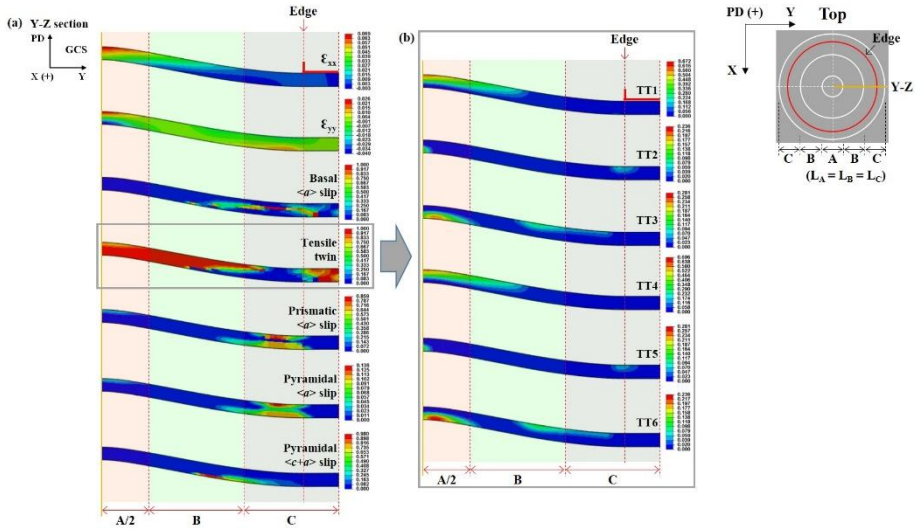

Figure 4.30 CPFEM results for the Y-Z section of orientation B (IE = 2.0 mm) after the Erichsen simulation: spatial distribution of (a) strain components, relative activities of deformation modes, and (b) accumulated volume fraction of TTW variants.

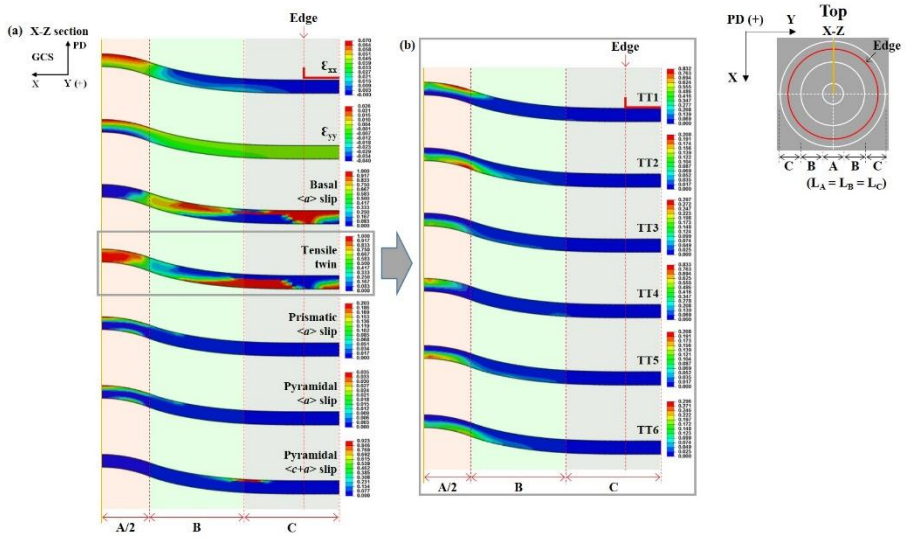

Figure 4.31 CPFEM results for the X-Z section of orientation B (IE = 2.0 mm) after the Erichsen simulation: spatial distribution of (a) strain components, relative activities of deformation modes and (b) accumulated volume fraction of TTW variants.

4.3.2 Characterization of TBs using EBSD analysis

Figure 4.32(a) is a schematic representation of the Y-Z and X-Z sections after the Erichsen test. Analysis of the microtexture evolutions in RB was divided into two portions: RB1 adjacent to RA and RB2 adjacent to RC. The microtexture evolution in RC were also analyzed in two portions: RC1 adjacent to RB and RC2 adjacent to the dome edge. The PD(//Z)-inverse pole figure (PD-IPF) maps of the two cross-sections appear in Figure 4.32(b), and corresponds to the right-half of the schematic representation in Figure 4.32(a). The crystal orientation of the deformed specimen was corrected by rotation, which was based on the GCS to ease analysis. Microtexture analysis of the cross-sections revealed that the heterogeneous evolution of deformation twinning was developed in a heterogeneous manner throughout the deformed specimen, exhibiting the differences in surface slopes along X and Y directions.

Microtexture analysis combined with the TTW traces effectively explained the twinning behavior occurring in a deformed Mg single crystal during the Erichsen test. LSCS was used to describe the spatial morphology and variant type of TBs developed in the Y-Z and X-Z sections. Moreover, the thickness of the observation area was equally divided into five portions to explain the twinning behavior based on LSCS: upper (U), upper-middle (UM), middle (M), lower-middle (LM), and lower (L). The color used to draw the TTW traces was also applied to the TBs to more easily identify the corresponding variants.

Figure 4.33 shows the results of the twin analysis for RA. In the Y-Z section, four variants of TTW (TT1, TT3, TT4 and TT5) occurred unevenly through the thickness direction of the deformed specimen with a total twin

area fraction of 0.105. TT1 with the largest fraction of twinned area (0.070) was formed from the U portion to the UM portion as well as in the LM portion along the y-axis. TT3 was formed from the L portion to the LM portion in an inclining state at a specific tilt angle (~ 60° cw) with respect to the y-axis. TT4 was formed from the U portion to the LM portion along the y-axis. TT5 with a very small fraction of twinned area (~ 0.001) was formed from the LM portion to the M portion in an inclining state at a specific tilt angle (~ 60° ccw) with respect to the y-axis. In the X-Z section, all the six variants of TTW were activated unevenly through the thickness direction of the specimen with a total twin area fraction of 0.134. TT1 with the largest fraction of twinned area (0.097) was formed throughout the specimen (from the U portion to the L portion) in an inclining state at a specific tilt angle (~ 47° cw) with respect to the x-axis. TT2 with a very small fraction of twinned area (~ 0.001) was formed in the L portion in an inclining state at a specific tilt angle (~ 65° cw) with respect to the x-axis. TT3 was formed from the L portion to the LM portion in an inclining state at a specific tilt angle (~ 65° cw) with respect to the x-axis. TT4 was formed throughout the specimen (from the L portion to the U portion) in an inclining state at a specific tilt angle (~ 47° ccw) with respect to the x-axis. TT5 was formed from the L portion to the LM portion in an inclining state at a specific tilt angle (~ 65° ccw) with respect to the x-axis. TT6 was formed from the L portion to the M portion in an inclining state at a specific tilt angle (~ 65° ccw) with respect to the x-axis. The commonly observed twin variants in the Y-Z and X-Z sections of RA were TT1, TT3, TT4 and TT5.

Figure 4.34 shows the results of the twin analysis for RB1. It is found that the deformed specimen observed on the Y-Z section is placed in a state with a ~ 7° surface slope relative to the Y-axis, whereas the deformed

specimen on the X-Z section has a surface slope of ~ 10° with respect to the X-axis. The Y-Z section displayed no evidence of twin variants. In the X-Z section, five variants of TTW (TT1, TT2, TT4, TT5 and TT6) were activated unevenly through the thickness direction of the specimen with a total twin area fraction of 0.045. TT1 was formed from the U portion to the UM portion as well as in the L portion in an inclining state at a specific tilt angle (~ 47° cw) with respect to the x-axis. TT2 was formed from the L portion to the M portion in an inclining state at a specific tilt angle (~ 65° cw) with respect to the x-axis. TT4 was formed from the L portion to the LM portion in an inclining state at a specific tilt angle (~ 47° ccw) with respect to the x-axis. TT5 with the largest fraction of twinned area (0.029) was formed from the L portion to the UM portion in an inclining state at a specific tilt angle (~ 65° ccw) with respect to the x-axis. TT6 with a very small fraction of twinned area (< 0.001) was formed from the L portion to the M portion in an inclining state at a specific tilt angle (~ 65° ccw) with respect to the x-axis.

Figure 4.35 shows the results of the twin analysis for RB2. The Y-Z section exhibited a surface slope of ~ 4° based on the Y-axis, whereas the X-Z section has a surface slope that was almost parallel to the X-axis. In the Y-Z section, only TT3 occurred unevenly through the thickness direction of the deformed specimen with a twin area fraction of 0.002. TT3 was formed from the U portion to the UM portion in an inclining state at a specific tilt angle (~ 60° cw) with respect to the y-axis. In the X-Z section, three variants of TTW (TT2, TT4 and TT5) were activated unevenly through the thickness direction of the specimen with a total twin area fraction of 0.034. TT2 was formed from the L portion to the M portion in an inclining state at a specific tilt angle (~ 65° cw) with respect to the x-axis. TT4 with the largest fraction of twinned area (0.017) was formed from the L portion to the M portion in an inclining state at

a specific tilt angle (~ 47° ccw) with respect to the x-axis. TT5 was formed throughout the specimen (from the L portion to the U portion) in an inclining state at a specific tilt angle (~ 65° ccw) with respect to the x-axis. No twin variant was commonly observed in the Y-Z and X-Z sections of RB2.

Figure 4.36 shows the results of the twin analysis for RC1. In the Y-Z section, only TT3 occurred unevenly through the thickness direction of the deformed specimen with a twin area fraction of 0.002. TT3 was formed from the U portion to the UM portion in an inclining state at a specific tilt angle (~ 60° cw) with respect to the y-axis. In the X-Z section, only TT4 occurred unevenly through the thickness direction of the deformed specimen with a twin area fraction of 0.034. TT4 was formed from the L portion to the M portion in an inclining state at a specific tilt angle (~ 47° ccw) with respect to the x-axis. No twin variant was commonly observed in the Y-Z and X-Z sections of RC1.

Figure 4.37 shows the results of twin analysis for RC2. In the Y-Z section, it was analyzed that two variants of TTW (TT3 and TT5) occurred unevenly through the thickness direction of the specimen with a total twin area fraction of 0.007. TT3 with a very small fraction of twinned area (~ 0.001) was formed from the U portion to the UM portion in an inclining state at a specific tilt angle (~ 60° cw) with respect to the y-axis. TT5 with the largest fraction of twinned area (0.006) was formed from the U portion to the M portion in an inclining state at a specific tilt angle (~ 60° ccw) with respect to the y-axis. The X-Z section displayed no evidence of twin variants.

Figure 4.38 compares the twinning behaviors that occurred in the five subdivided regions of the (a) Y-Z and (b) X-Z sections for orientation B (IE = 2.0 mm). A majority of the TTW variants in the Y-Z section existed throughout RA, RB1 and RC2. This result seemed due to the opposite strain

gradient through the thickness direction. In other words, the TTWs were concentrated in the regions where the ε_{xx} component was positive and the ε_{yy} component was negative. The most important observation here is that most TBs were nucleated at the free surface of deformed specimen and tended to propagate into the matrix. In order to accommodate the initial external strain of the Erichsen test, shear deformation occurred in the basal $\langle \boldsymbol{a} \rangle$ slip system as well as in the TTW system. Accumulation of shear deformation tended to create small irregularities in the free surface of deformed specimen. As a result, it is believed that the stress concentration occurring at these small irregularities during deformation provided the nucleation site for the TBs. Analysis of the TTW behavior in the X-Z section quantitatively shows that the TBs in RA, RB, and RC1 developed mainly in the lower portion of the deformed specimen and the TBs in RC2 developed mainly in the upper portion of the deformed specimen. This result can be explained by the distribution of the strain components, as demonstrated in the Y-Z section. The ε_{yy} component in a region where TBs are observed has a positive value that is favorable for the nucleation of TBs, while the ε_{xx} component has a very low value in the same region of a deformed specimen. The spatial distribution of the relative activity of the TTW provided a good explanation for the location of the TTW that is observed experimentally in the deformed specimen.

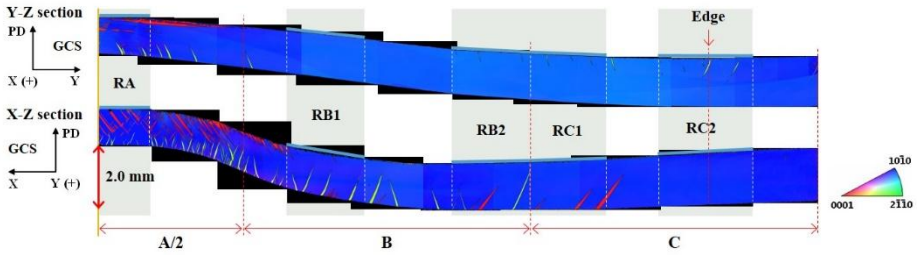

Figure 4.32 The PD(//Z)-inverse pole figure (PD-IPF) maps in the Y-Z and X-Z sections (corresponding to the right half of the schematic diagram) of orientation B (IE = 2.0 mm).

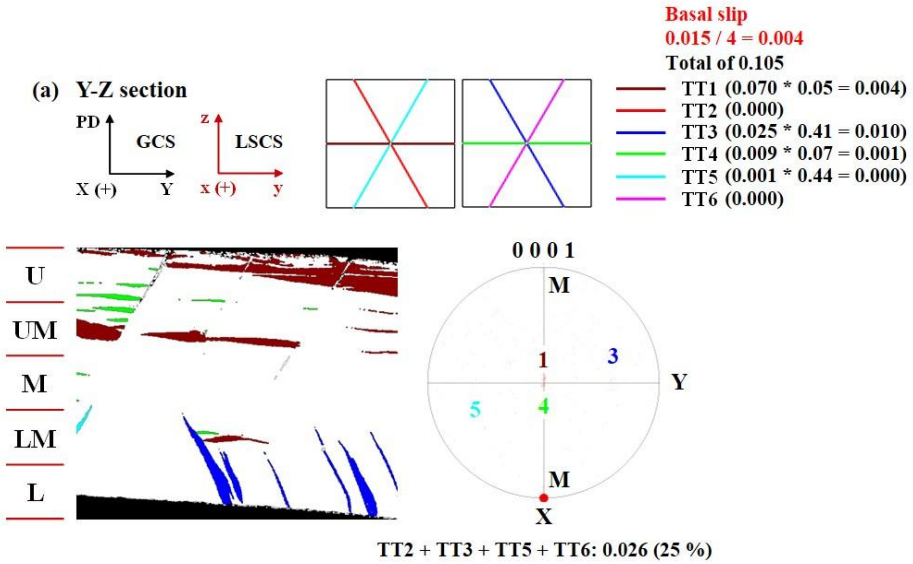

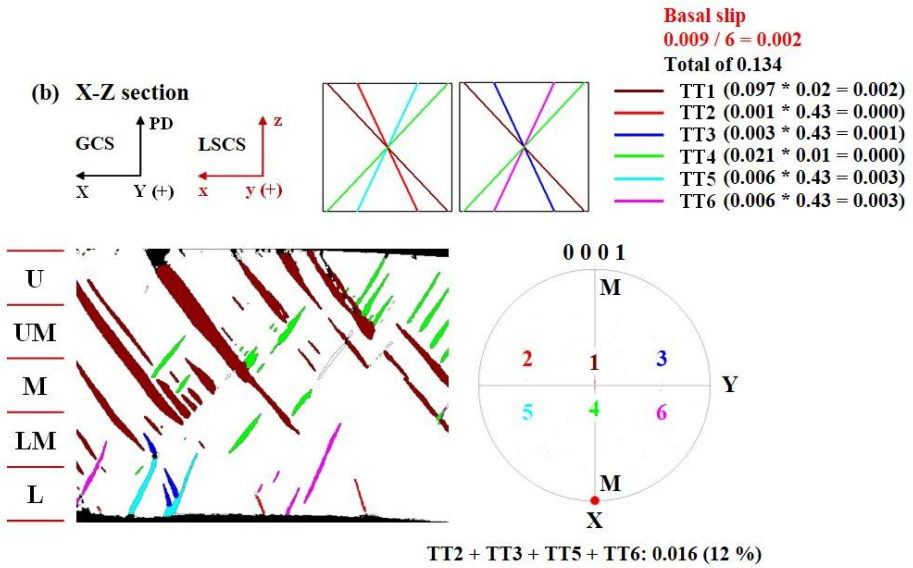

Figure 4.33 Twin analysis of RA in the (a) Y-Z and (b) X-Z sections of orientation B (IE = 2.0 mm).

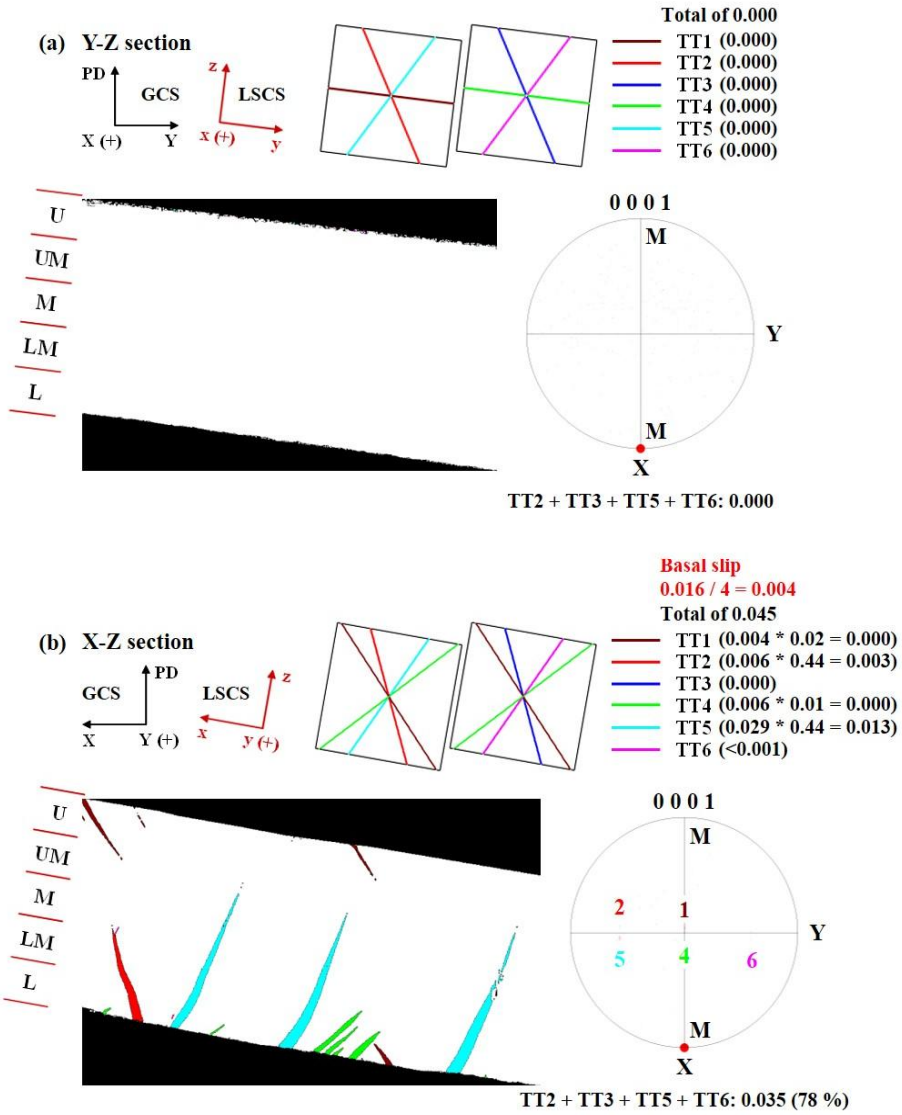

Figure 4.34 Twin analysis of RB1 in the (a) Y-Z and (b) X-Z sections of orientation B (IE = 2.0 mm).

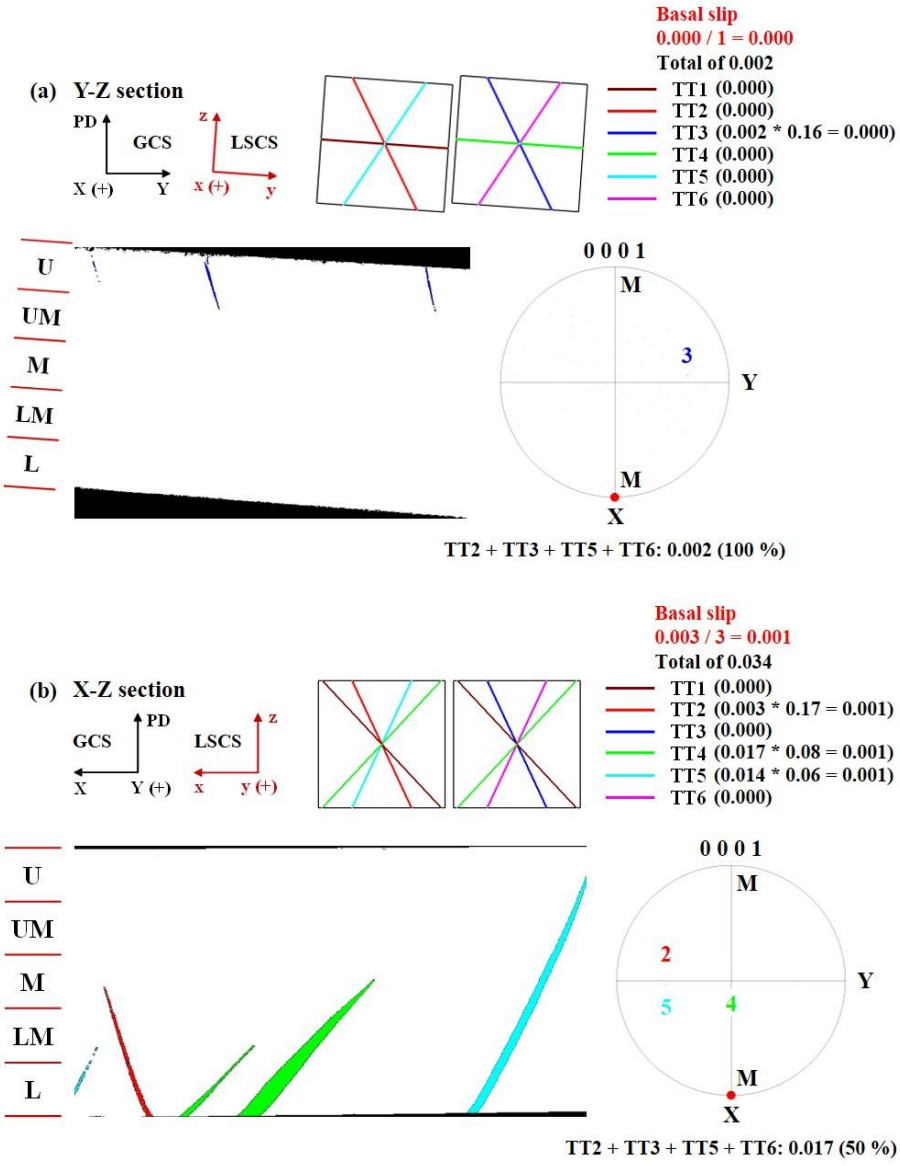

Figure 4.35 Twin analysis of RB2 in the (a) Y-Z and (b) X-Z sections of orientation B (IE = 2.0 mm).

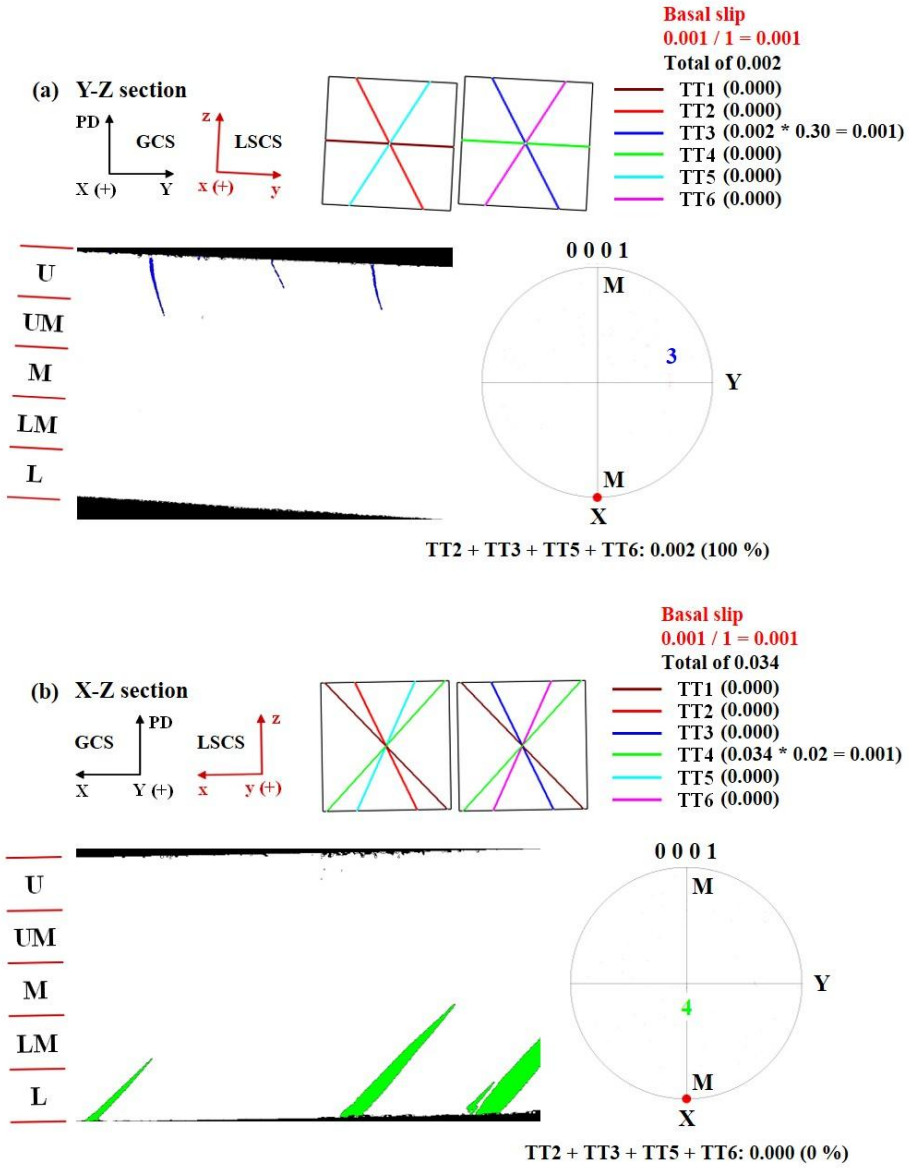

Figure 4.36 Twin analysis of RC1 in the (a) Y-Z and (b) X-Z sections of orientation B (IE = 2.0 mm).

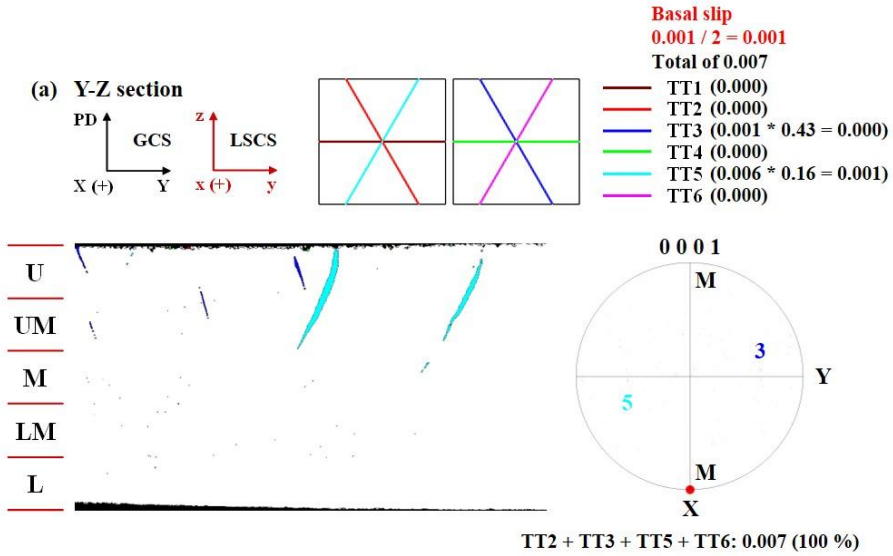

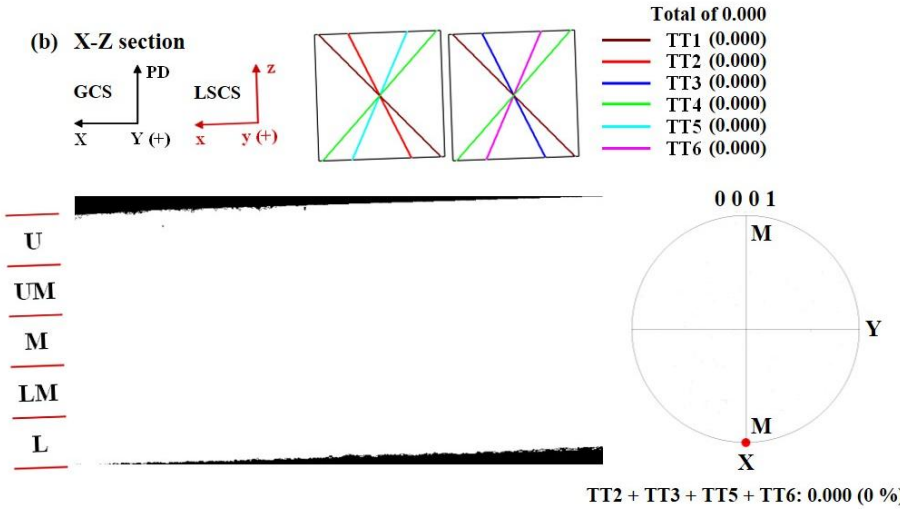

Figure 4.37 Twin analysis of RC2 in the (a) Y-Z and (b) X-Z sections of orientation B (IE = 2.0 mm).

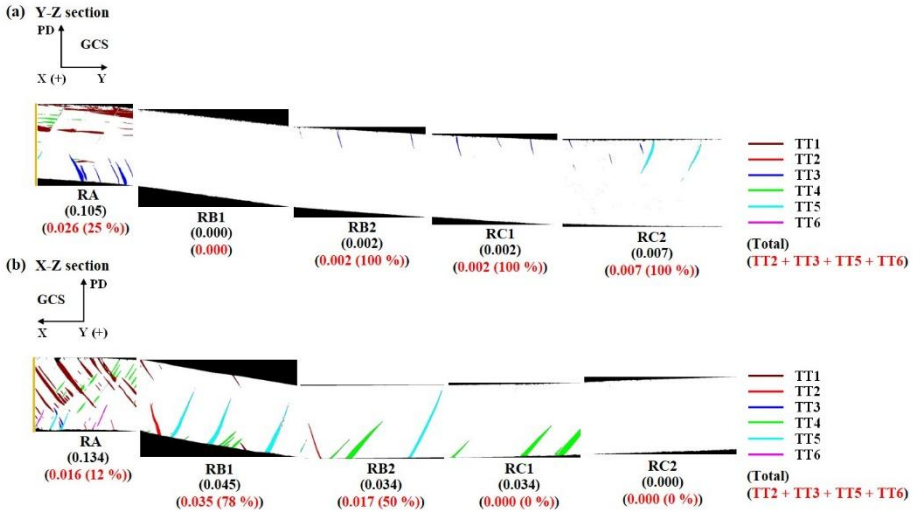

Figure 4.38 A comparison of the five subdivided regions in the (a) Y-Z and (b) X-Z sections of orientation B (IE = 2.0 mm).

Figure 4.39 shows the values for basal slip activation as a function of the five subdivided regions in the Y-Z and X-Z sections of orientation B. The results indicate that the values for basal slip activation systematically increases with increasing the punch stroke. Interestingly, the values in the five distinct regions of the X-Z section are relatively higher than those of the Y-Z section. This phenomenon can be supported the relative activities of deformation modes for the bottom-surface of orientation B (Figure 4.40). As the punch stroke increases, it becomes more favorable for tensile twinning to be activated especially along the X direction. Therefore, the newly formed orientation with the c-axis tilted toward Y direction makes the basal slip be activated along the corresponding direction. Figure 4.41 depicts the mechanism for improving RT stretch formability of orientation B. It clearly explains that the major role of TT2, TT3, TT5 and TT6 is to assist in making favorable orientation for additional basal slip activation by crystallographic reorientation and consequently basal slip occurs along the reoriented directions. As a result, the IE of 6.8 mm at RT was successfully achieved only controlling crystallographic reorientation without adding alloying element.

Figure 4.42 experimentally show the texture evolution of the PD(//Z)-inverse pole figure (PD-IPF) maps in the X-Z section of orientation B. It was found that the color of tensile twins nucleated from the bottom surface systematically changed from light green (IE = 2.0 mm) to light yellow (IE = 6.8 mm) as the punch stroke increased. The results imply the crystal rotation after basal slip, which means that a considerable amount of basal slip was activated during the Erichsen test. Figure 4.43(a) systematically shows the texture evolution in the X-Z section of orientation B. It was also found that the color of tensile twins nucleated from the bottom surface systematically changed from orange (IE = 2.0 mm) to light orange (IE = 6.8 mm) as the

punch stroke increased. In addition, # 5 of 2.0 mm, # 7 of 4.0 mm and # 9 of 6.8 mm among 10 respective inverse pole figure maps have the initial points of twinned poles tilted from 28° ~ 37° from $[\bar{1}2\bar{1}0]$ (Figure 4.43(b)). These twinned poles correspond to the orange (or light orange)-colored tensile twins (Figure 4.43(a)) which are nucleated from the bottom surface and enable the specimen to be deformed by making favorable orientation for additional basal slip activation by crystallographic reorientation.

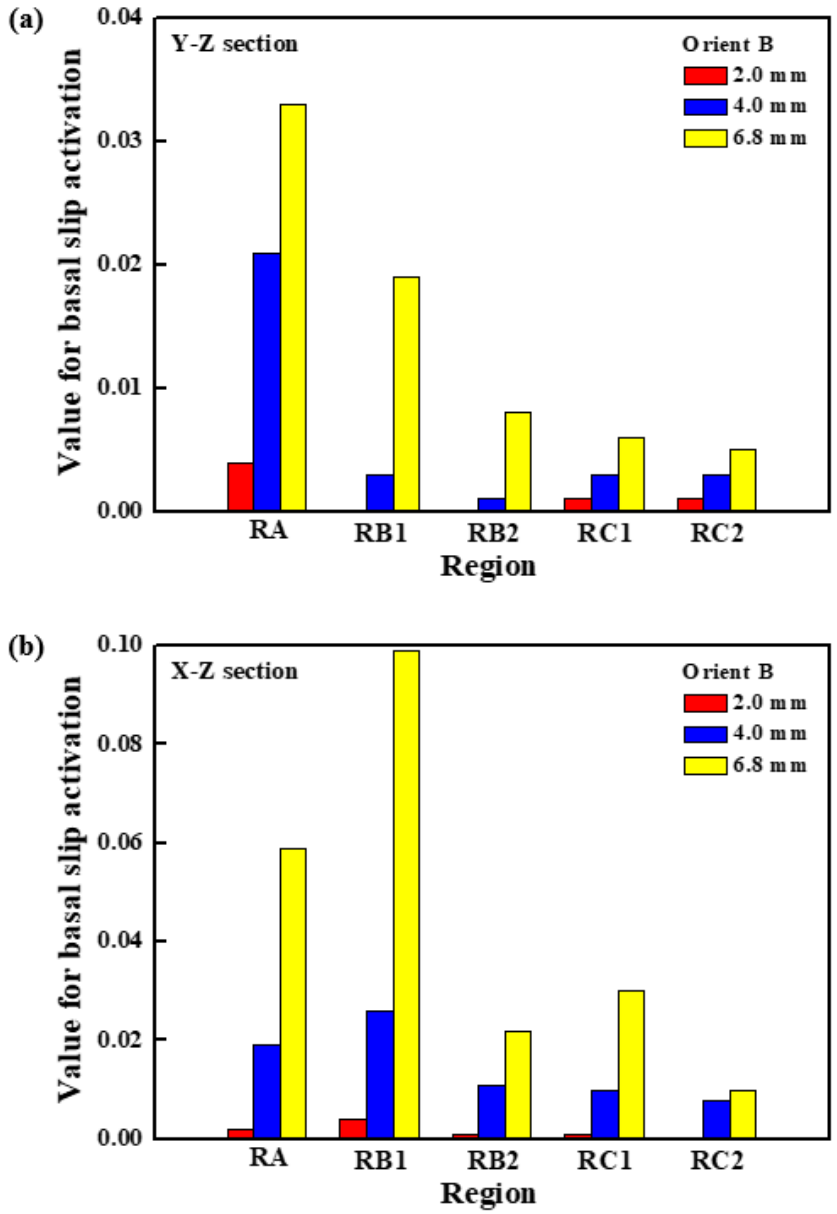

Figure 4.39 Values for basal slip activation as a function of the five subdivided regions in the (a) Y-Z and (b) X-Z sections of orientation B (IE = 2.0, 4.0 and 6.8 mm).

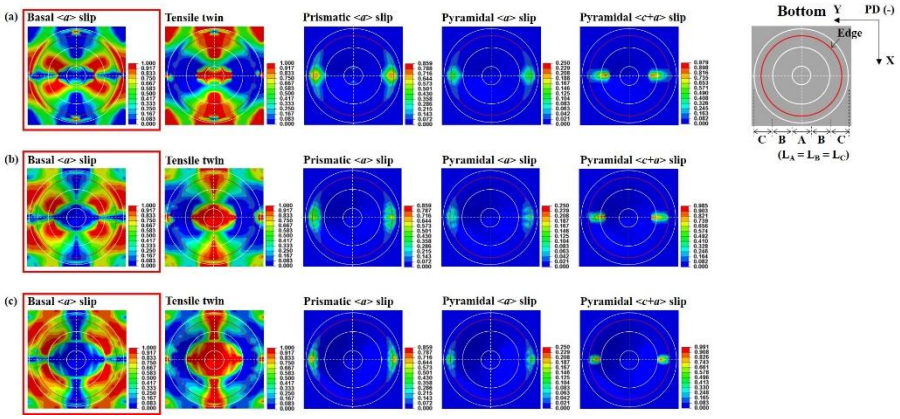

Figure 4.40 A comparison of the relative activities of deformation modes for the bottom-surface of orientation B: spatial distribution of (a) IE = 2.0 mm, (b) IE = 4.0 mm and (c) IE = 6.8 mm.

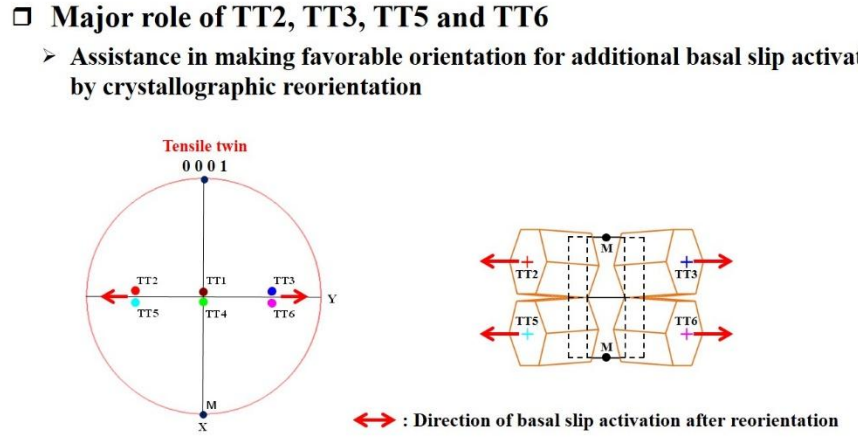

Figure 4.41 A mechanism for improving RT stretch formability of orientation B (IE = 2.0, 4.0 and 6.8 mm).

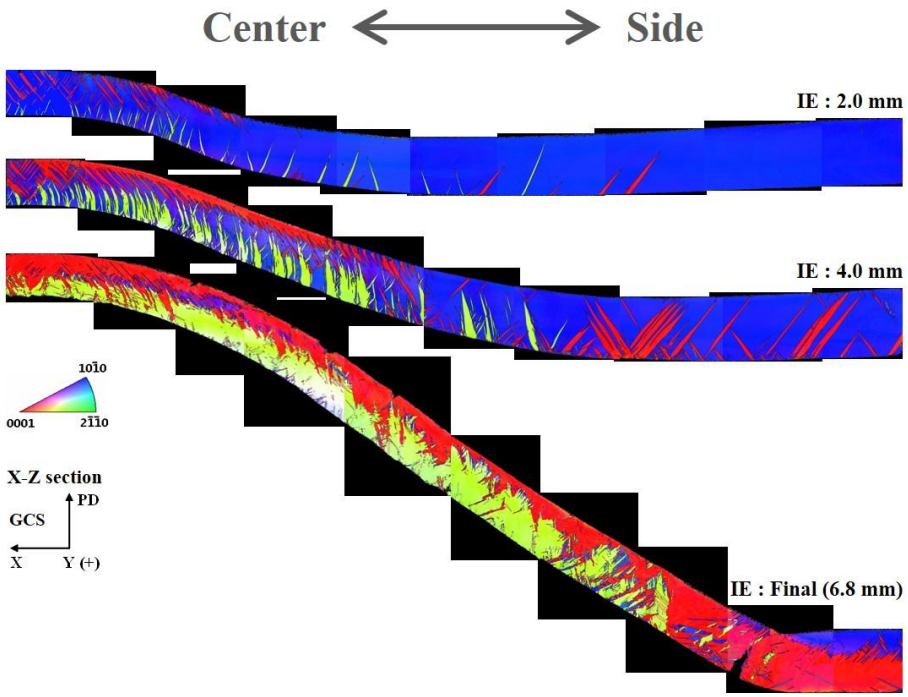

Figure 4.42 Texture evolution of the PD(//Z)-inverse pole figure (PD-IPF) maps in the X-Z section of orientation B (IE = 2.0, 4.0 and 6.8 mm).

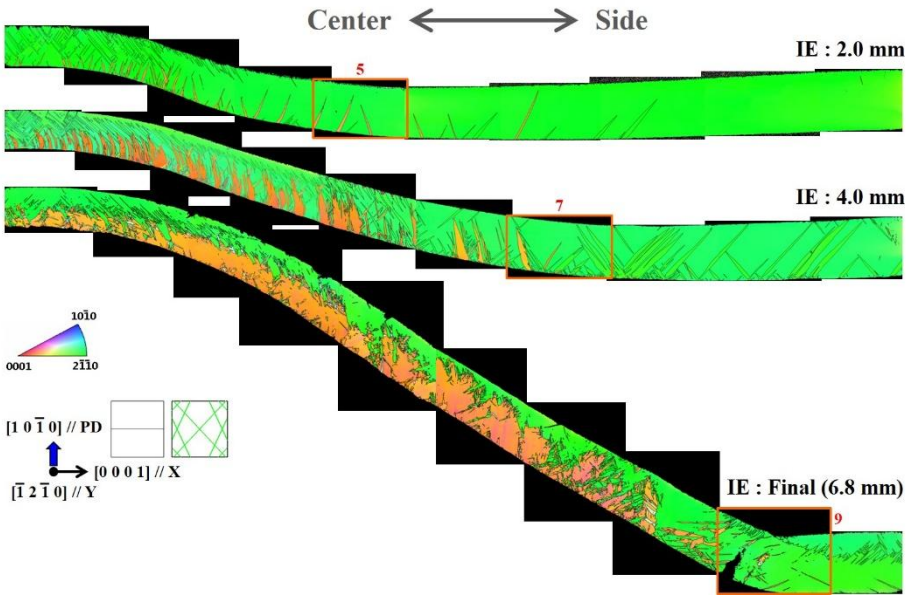

(a)

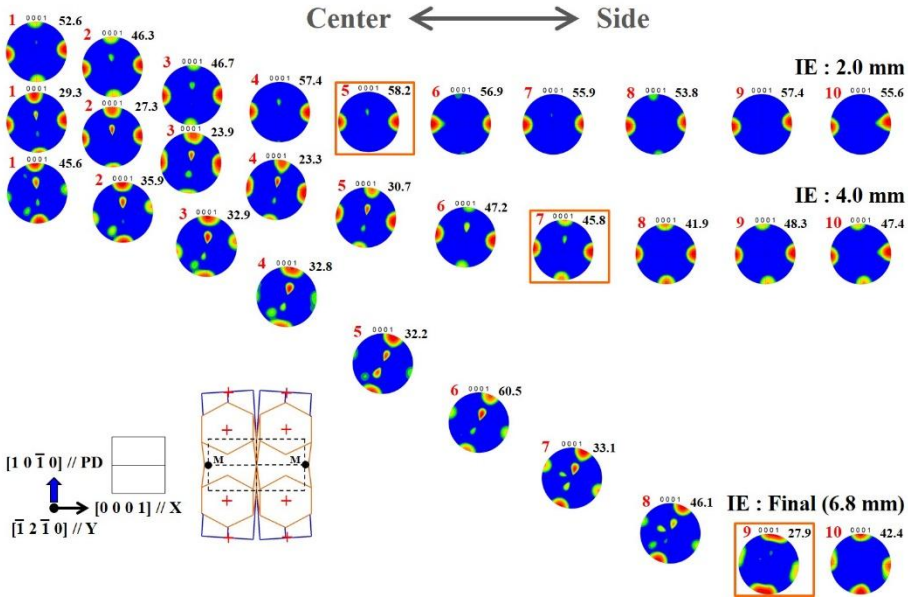

(b)

Figure 4.43 Texture evolution ((a) inverse pole figure maps and (b) their pole figures) in the X-Z section of orientation B (IE = 2.0, 4.0 and 6.8 mm).

4.4 Results and discussion (Orientation C)

4.4.1 Erichsen test simulation using CPFEM

In the case of the Erichsen test, the specimen is subjected to a non-uniform deformation history in the plane and thickness directions of the specimen. Furthermore, since the anisotropy of single crystal specimens is so strong, the non-uniformity of deformation in a deformed specimen becomes much more intense, which necessitates an understanding of the non-uniformity of deformation using simulation techniques such as CPFEM. When the PD is parallel to the $[1\ \bar{2}\ 1\ 0]$ direction, the initial crystallographic orientation of a Mg single crystal during the Erichsen test has the orientation relationship of 90° between PD and c-axis, which can be expressed as (ϕ_1, Φ, ϕ_2) = (-90°, 90°, 90°) in Euler space, as described in Figure 4.44(a). The results of the Erichsen test at RT in Figure 4.44(b) show that plastic anisotropy induced an asymmetrically deformed dome shape with respect to the center of both the top and bottom of the deformed specimen. As a consequence, fracture occurred near the dome center parallel to the X-axis under a punch stroke with an IE of 2.0 mm. Furthermore, in order to systematically investigate the twinning behavior and deformation mechanisms during the Erichsen test, the deformed specimen was equally divided into three distinct regions ($L_A = L_B = L_C$). The three distinct regions are defined as follows. Region A (RA) is the area near the center of the deformed specimen, and is the point at which severe biaxial strain (or stress) occurs during an Erichsen test. Region B (RB) is the intermediate area between the center and the circumference of the deformed specimen. Region C (RC) is the area of the circumference of the deformed specimen, and it the point at which an upper

die imposes normal pressure during an Erichsen test.

CPFEM simulation can identify the spatial distribution of strain components, the relative activities of deformation modes and the V^{acc} of the twin variants developed in the three distinct regions during the Erichsen test. Figure 4.45 shows the spatial distribution of the strain components, the relative activities of the deformation modes and the V^{acc} of the twin variants that developed on the top-surface of the deformed specimen. The strain components generated in the Mg single crystal specimen were symmetrically distributed with respect to the center of the specimen, as shown in Figure 4.45(a). In particular, ε_{xx} exhibited a considerable strain gradient in the X direction. It was interesting to note the large difference between maximum ε_{xx} (= 0.046) and maximum ε_{yy} (= 0.016) components at the center of the deformed Mg single crystal. The deformation behavior in this region deviates significantly from equi-biaxial deformation. As shown in Figure 4.45(b), the primary deformation mode in the RA and RB is basal $\langle \boldsymbol{a} \rangle$ slip, and the primary deformation mode in the RC is TTW. It is interesting to note that the V^{acc} of twin variants on the top-surface corresponded mostly to the region of negative ε_{yy}. Among the six twin variants, TT1, TT3, TT4 and TT6 were mainly activated on the area near the center of the top-surface (Figure 4.45(b)).

Figure 4.46 shows the spatial distribution of strain components, the relative activities of deformation modes, and the V^{acc} of twin variants that had developed on the bottom-surface. The strain components at the bottom-surface of the deformed Mg single crystal were also symmetrically distributed with respect to the center of the specimen, where ε_{xx} and ε_{yy} had positive and negative values, respectively, as shown in Figure 4.46(a). As shown in Figure 4.46(b), the basal $\langle \boldsymbol{a} \rangle$ slip acted as the primary deformation mode,

except for one side from the specimen center parallel to the X-axis, for which the primary deformation mode was TTW. The non-basal slip systems were weakly activated only at the edge of the specimen in the RC parallel to the Y-axis. Figures 4.47 and 4.48 show the CPFEM results for strain components, the relative activity of deformation modes, and the V^{acc} of twin variants that developed on the Y-Z and X-Z sections, respectively. It is recently reported that, due to the orthotropic texture, the stress state through the thickness direction in polycrystalline Mg is also inhomogeneous during the Erichsen test at RT [20]. The spatial distributions of ε_{xx} and ε_{yy} in the RA indicates that biaxial tensile strain is applied along both x and y directions in the upper portion, while tensile and compressive strains are applied in the x and y directions in the lower portion. The spatial distribution of ε_{yy} that developed on the Y-Z section (Figure 4.47(a)) indicated that tensile strain was applied to the upper portion of RA and to the lower portion of RC, while compressive strain was applied to the lower portion of RA and to the upper portion of RC. On the other hand, the spatial distribution of ε_{yy} that developed on the X-Z section (Figure 4.48(a)) indicates that tensile strain was applied to the upper portion of RA while compressive strain was mostly applied to the lower portion of RA. It is noteworthy that the ε_{yy} that had developed on the X-Z section was almost zero through the thickness direction at the dome edge of RC, meaning that this geometrically approximated plain-strain conditions. On the other hand, considering the strain components observed with the Y-Z section at the dome edge of the RC, the deformation behavior of this region seemed similar to that obtained in the V-bending test [18]. In other words, the outer and inner portions of RC are considered as tension and compression zones, respectively. Interestingly, the RB in the Y-Z section did not effectively

contribute to the deformation, which indicated that it was difficult to deform the specimen in the y direction during the Erichsen test, and the V-bending effect that occurred in the RC enabled the dome to deform. Figures 4.47(b) and 4.48(b) show the V^{acc} of the TTW variants in the Y-Z and X-Z sections, respectively. In the RA, regardless of section, the values for V^{acc} of the TT1, TT3, TT4 and TT6 in the upper portion were relatively higher than those in the lower portion, while the values for V^{acc} of the TT2 and TT5 in the lower portion were relatively higher than those in the upper portion. This behavior can be attributed to tensile deformation in the y direction in this portion during the Erichsen test. Based on the experimental results, this will be discussed in more detail in Section 4.4.2. In the RB, the V^{acc} of the TT1 and TT4 was negligible in the Y-Z section, and the V^{acc} of the TT2 and TT5 at the bottom of the specimen in the X-Z section was relatively higher than that of the other twin variants. This behavior seemed due to the tensile strain in the x direction and to the compressive strain in the y direction in the lower portion of the X-Z section. In the RC, the V^{acc} at the upper portion of the specimen in the Y-Z section was relatively higher than that at the lower portion because the strain was small in the x direction but compressive strain was acting in the y direction in this portion. On the other hand, the value for V^{acc} was low at the center of the specimen in the X-Z section despite a high relative activity of twin, which can be attributed to a relatively low level of deformation in RC during the Erichsen test compared with that in both RA and RB.

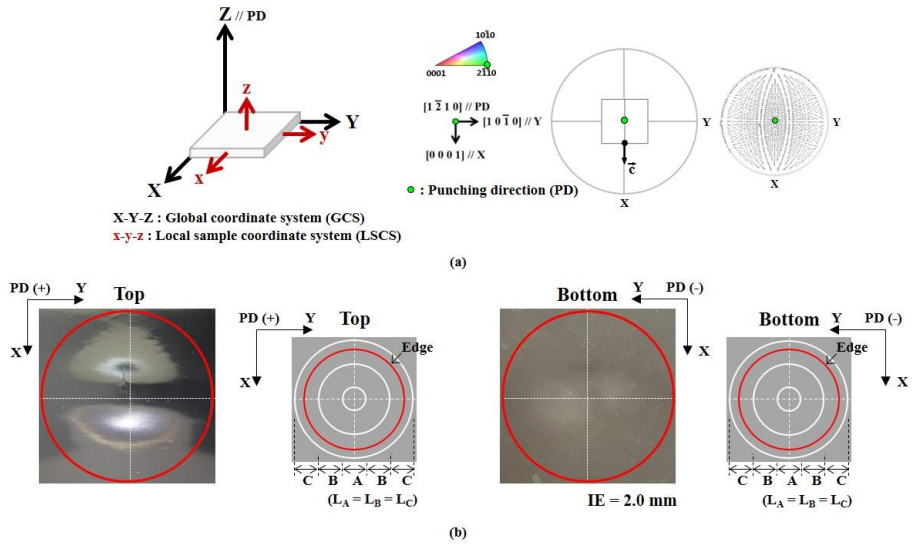

Figure 4.44 (a) Initial crystallographic orientation and (b) Erichsen test results of orientation C (IE = 2.0 mm).

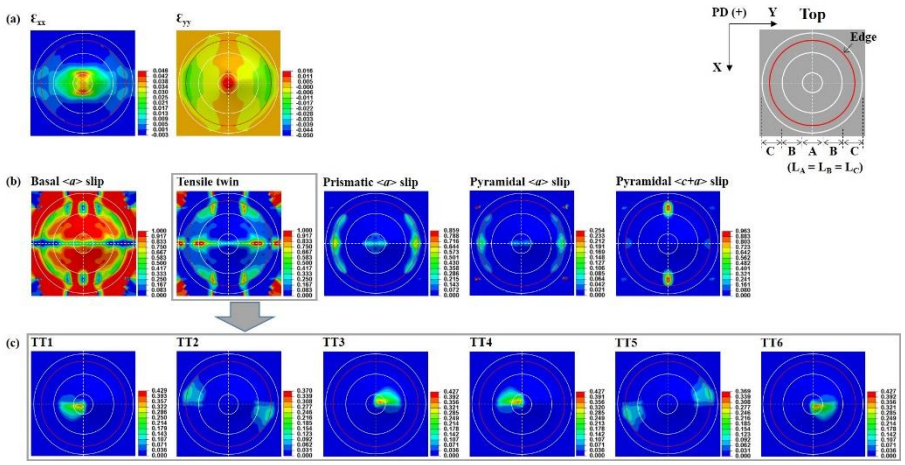

Figure 4.45 CPFEM results for the top-surface of orientation C (IE = 2.0 mm) after the Erichsen simulation: spatial distribution of (a) strain components, (b) relative activities of deformation modes, and (c) accumulated volume fraction of TTW variants.

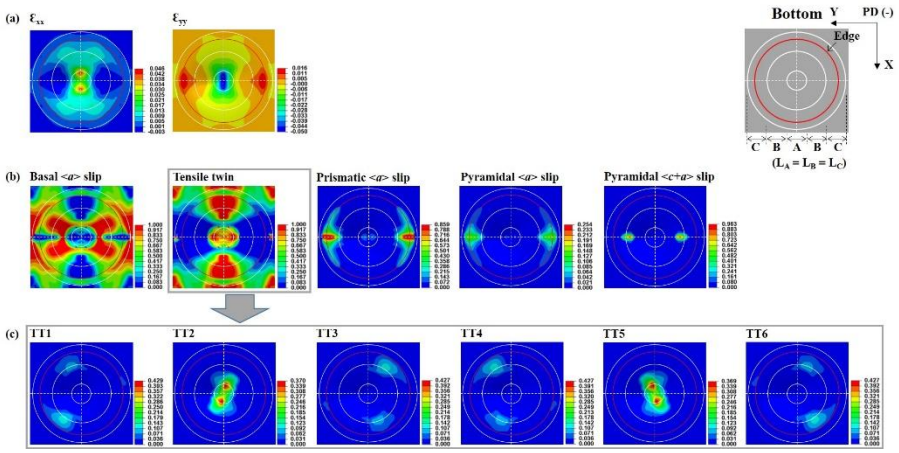

Figure 4.46 CPFEM results for the bottom-surface of orientation C (IE = 2.0 mm) after the Erichsen simulation: spatial distribution of (a) strain components, (b) relative activities of deformation modes, and (b) accumulated volume fraction of TTW variants.

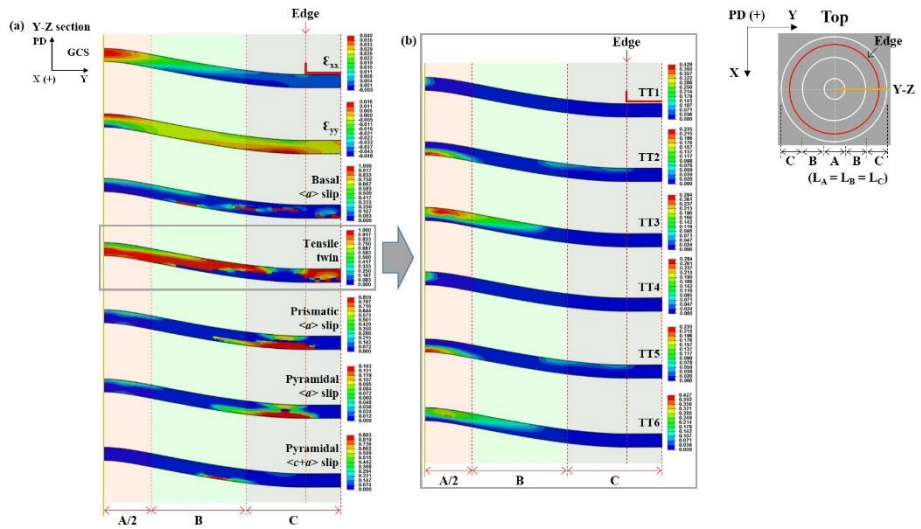

Figure 4.47 CPFEM results for the Y-Z section of orientation C (IE = 2.0 mm) after the Erichsen simulation: spatial distribution of (a) strain components, relative activities of deformation modes, and (b) accumulated volume fraction of TTW variants.

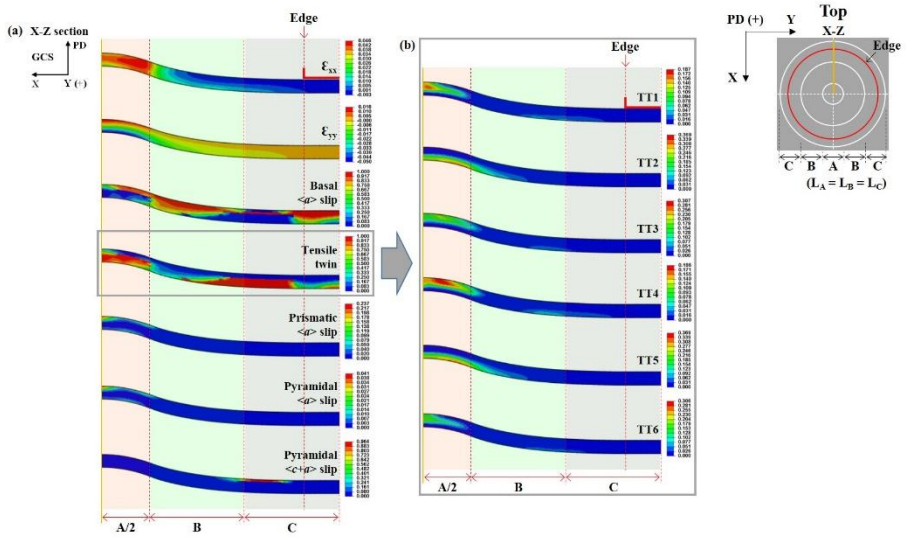

Figure 4.48 CPFEM results for the X-Z section of orientation C (IE = 2.0 mm) after the Erichsen simulation: spatial distribution of (a) strain components, relative activities of deformation modes and (b) accumulated volume fraction of TTW variants.

4.4.2 Characterization of TBs using EBSD analysis

Figure 4.49(a) demonstrates the TTW and compression twin (CTW) variants that can be activated from the initial crystallographic orientation of Mg single crystal during the Erichsen test. In some areas, CTW was experimentally observed and thus considered together in the twin orientation analysis. Six variants of CTW were additionally considered as follows: CT1— $(10\bar{1}1)[10\bar{1}\bar{2}]$, CT2— $(\bar{1}011)[\bar{1}01\bar{2}]$, CT3— $(01\bar{1}1)[01\bar{1}\bar{2}]$, CT4— $(0\bar{1}01)[0\bar{1}1\bar{2}]$, CT5— $(1\bar{1}01)[1\bar{1}0\bar{2}]$, and CT6— $(\bar{1}\bar{1}01)[\bar{1}10\bar{2}]$. Figure 4.49(b) depicts the geometrical calculation of TTW traces that had occurred in the Y-Z and X-Z sections during the Erichsen test. Interestingly, TT2 and TT5 were parallel to the vertical direction, whereas TT1, TT3, TT4 and TT6 were analyzed to grow in a state of being inclined across the thickness of the specimen. In the Y-Z section, TT1/TT6 and TT3/TT4 were tilted 60° clockwise (cw) and 60° counterclockwise (ccw) respectively based on the z-axis. In the X-Z section, TT1/TT6 and TT3/TT4 were inclined by 39° cw and 39° ccw respectively based on the z-axis.

Figure 4.50(a) is a schematic representation of the Y-Z and X-Z sections after the Erichsen test. Analysis of the microtexture evolutions in RB was divided into two portions: RB1 adjacent to RA and RB2 adjacent to RC. The microtexture evolution in RC were also analyzed in two portions: RC1 adjacent to RB and RC2 adjacent to the dome edge. The PD(//Z)-inverse pole figure (PD-IPF) maps of the two cross-sections appear in Figure 4.50(b), and corresponds to the right-half of the schematic representation in Figure 4.50(a). The crystal orientation of the deformed specimen was corrected by rotation, which was based on the GCS to ease analysis. Microtexture analysis of the cross-sections revealed that the heterogeneous evolution of deformation

twinning was developed in a heterogeneous manner throughout the deformed specimen, exhibiting the differences in surface slopes along X and Y directions.

Microtexture analysis combined with the TTW traces effectively explained the twinning behavior occurring in a deformed Mg single crystal during the Erichsen test. LSCS was used to describe the spatial morphology and variant type of TBs developed in the Y-Z and X-Z sections. Moreover, the thickness of the observation area was equally divided into five portions to explain the twinning behavior based on LSCS: upper (U), upper-middle (UM), middle (M), lower-middle (LM), and lower (L). The color used to draw the TTW traces was also applied to the TBs to more easily identify the corresponding variants.

Figure 4.51 shows the results of the twin analysis for RA. In the Y-Z section, three variants of TTW (TT2, TT3 and TT5) occurred unevenly through the thickness direction of the deformed specimen with a total twin area fraction of 0.127. TT2 was formed from the L portion to the UM portion along the z-axis. TT3 with a very small fraction of twinned area (< 0.001) was formed from the M portion to the LM portion in an inclining state at a specific tilt angle (~ 60° ccw) with respect to the z-axis. TT5 with the largest fraction of twinned area (0.098) was formed from the L portion to the UM portion along the z-axis. In the X-Z section, three variants of TTW (TT1, TT2 and TT5) were activated unevenly through the thickness direction of the specimen with a total twin area fraction of 0.269. TT1 was formed from the L portion to the UM portion in an inclining state at a specific tilt angle (~ 39° cw) with respect to the z-axis. TT2 with the largest fraction of twinned area (0.147) was formed throughout the specimen (from both the U portion and the L portion) along the z-axis. TT5 was formed throughout the specimen (from both the U

portion and the L portion) along the z-axis. The commonly observed twin variants in the Y-Z and X-Z sections of RA were TT2 and TT5.

Figure 4.52 shows the results of the twin analysis for RB1. The Y-Z section exhibited a surface slope of ~ 3° based on the Y-axis, whereas the X-Z section has a surface slope of ~ 16° based on the X-axis. In the Y-Z section, only TT2 occurred unevenly through the thickness direction of the deformed specimen with a very small fraction of twinned area (< 0.001). TT2 was formed in the L portion along the z-axis. In the X-Z section, all the six variants of TTW were activated unevenly through the thickness direction of the specimen with a total twin area fraction of 0.322. TT1 was formed from the L portion to the LM portion as well as from the U portion to the UM portion in an inclining state at a specific tilt angle (~ 39° cw) with respect to the z-axis. TT2 with the largest fraction of twinned area (0.214) was formed throughout the specimen (from both the U portion and the L portion) along the z-axis. TT3 was formed from the L portion to the LM portion in an inclining state at a specific tilt angle (~ 39° ccw) with respect to the z-axis. TT4 with a very small fraction of twinned area (< 0.001) was formed in the U portion in an inclining state at a specific tilt angle (~ 39° ccw) with respect to the z-axis. TT5 was formed throughout the specimen (from both the U portion and the L portion) along the z-axis. TT6 was formed from the L portion to the LM portion in an inclining state at a specific tilt angle (~ 39° cw) with respect to the z-axis. TT2 was the commonly observed twin variant in the Y-Z and X-Z sections of RB1.

Figure 4.53 shows the results of the twin analysis for RB2. The Y-Z section exhibited a surface slope of ~ 7° based on the Y-axis, whereas the X-Z section has a surface slope that was almost parallel to the X-axis. In the Y-Z section, two variants of TTW (TT2 and TT5) occurred unevenly through the

thickness direction of the deformed specimen with a total twin area fraction of 0.007. TT2 with the largest fraction of twinned area (0.005) was formed from the U portion to the M portion along the z-axis. TT5 was formed from the U portion to the UM portion along the z-axis. In the X-Z section, five variants of TTW (TT1, TT2, TT3, TT4 and TT5) were activated unevenly through the thickness direction of the specimen with a total twin area fraction of 0.111. TT1 was formed from the L portion to the UM portion in an inclining state at a specific tilt angle (~ 39° cw) with respect to the z-axis. TT2 with the largest fraction of twinned area (0.046) was formed throughout the specimen (from both the U portion and the L portion) along the z-axis. TT3 with a very small fraction of twinned area (< 0.001) was formed in the L portion in an inclining state at a specific tilt angle (~ 39° ccw) with respect to the z-axis. TT4 was formed throughout the specimen (from the L portion to the U portion) in an inclining state at a specific tilt angle (~ 39° ccw) with respect to the z-axis. TT5 was formed throughout the specimen (from both the U portion and the L portion) along the z-axis. The commonly observed twin variants in the Y-Z and X-Z sections of RB2 were TT2 and TT5.

Figure 4.54 shows the results of the twin analysis for RC1. The Y-Z section exhibited a surface slope of ~ 7° based on the Y-axis, whereas the X-Z section has a surface slope that was almost parallel to the X-axis. In the Y-Z section, only TT2 occurred unevenly through the thickness direction of the deformed specimen with a twin area fraction of 0.004. TT2 was formed from the U portion to the M portion along the z-axis. In the X-Z section, three variants of TTW (TT1, TT2 and TT5) occurred unevenly through the thickness direction of the deformed specimen with a total twin area fraction of 0.343. TT1 was formed from the L portion to the LM portion as well as from the UM portion to the U portion in an inclining state at a specific tilt angle (~

39° cw) with respect to the z-axis. TT2 with the largest fraction of twinned area (0.226) was formed throughout the specimen (from both the U portion and the L portion) along the z-axis. TT5 was formed throughout the specimen (from both the U portion and the L portion) along the z-axis. TT2 was the commonly observed twin variant in the Y-Z and X-Z sections of RC1.

Figure 4.55 shows the results of the twin analysis for RC2. In the Y-Z section, four variants of TTW (TT1, TT2, TT3 and TT5) occurred unevenly through the thickness direction of the deformed specimen with a total twin area fraction of 0.008. TT1 with a very small fraction of twinned area (< 0.001) was formed in the M portion in an inclining state at a specific tilt angle (~ 60° cw) with respect to the z-axis. TT2 with the largest fraction of twinned area (0.007) was formed from the U portion to the UM portion along the z-axis. TT3 with a very small fraction of twinned area (< 0.001) was formed from the M portion to the LM portion in an inclining state at a specific tilt angle (~ 60° ccw) with respect to the z-axis. TT5 was formed from the U portion to the UM portion along the z-axis. In the X-Z section, three variants of TTW (TT2, TT4 and TT5) were activated unevenly through the thickness direction of the specimen with a total twin area fraction of 0.394. TT2 was formed throughout the specimen (from both the U portion and the L portion) along the z-axis. TT4 was formed from the L portion to the LM portion in an inclining state at a specific tilt angle (~ 39° ccw) with respect to the z-axis. TT5 with the largest fraction of twinned area (0.210) was formed throughout the specimen (from both the U portion and the L portion) along the z-axis. The commonly observed twin variants in the Y-Z and X-Z sections of RC2 were TT2 and TT5.

Figure 4.56 compares the twinning behaviors that occurred in the five subdivided regions of the (a) Y-Z and (b) X-Z sections for orientation C (IE =

2.0 mm). A majority of the TTW variants in the Y-Z section existed throughout RA, RB1 and RC2. This result seemed due to the opposite strain gradient through the thickness direction. In other words, the TTWs were concentrated in the regions where the ε_{xx} component was positive and the ε_{yy} component was negative. The most important observation here is that most TBs were nucleated at the free surface of deformed specimen and tended to propagate into the matrix. In order to accommodate the initial external strain of the Erichsen test, shear deformation occurred in the basal $\langle \boldsymbol{a} \rangle$ slip system as well as in the TTW system. Accumulation of shear deformation tended to create small irregularities in the free surface of deformed specimen. As a result, it is believed that the stress concentration occurring at these small irregularities during deformation provided the nucleation site for the TBs. Analysis of the TTW behavior in the X-Z section quantitatively shows that the TBs in RA, RB, and RC1 developed mainly in the lower portion of the deformed specimen and the TBs in RC2 developed mainly in the upper portion of the deformed specimen. This result can be explained by the distribution of the strain components, as demonstrated in the Y-Z section. The ε_{yy} component in a region where TBs are observed has a positive value that is favorable for the nucleation of TBs, while the ε_{xx} component has a very low value in the same region of a deformed specimen. The spatial distribution of the relative activity of the TTW provided a good explanation for the location of the TTW that is observed experimentally in the deformed specimen.

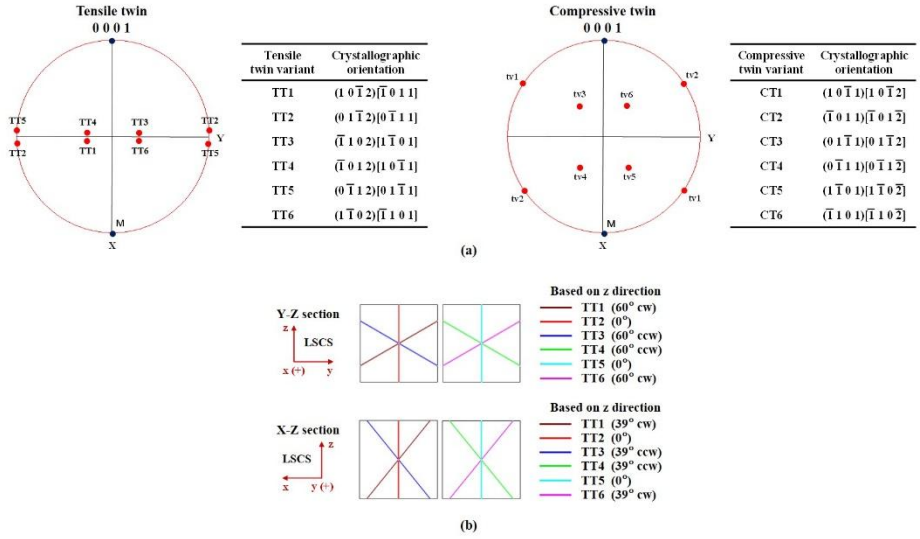

Figure 4.49 (a) TTW and CTW variants with their corresponding Miller indices for the initial crystallographic orientation and (b) geometrical calculation of TTW traces occurring in the Y-Z and X-Z sections of orientation C (IE = 2.0 mm).

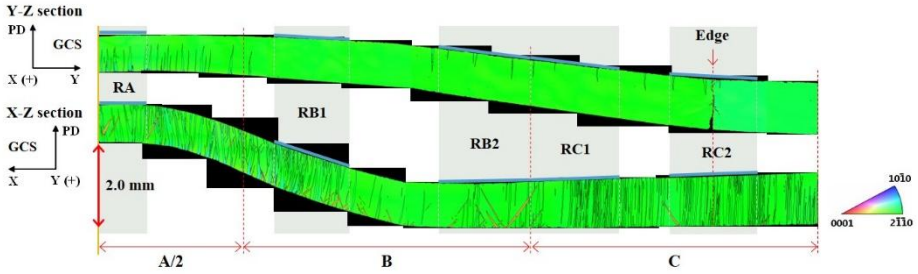

Figure 4.50 The PD(//Z)-inverse pole figure (PD-IPF) maps in the Y-Z and X-Z sections (corresponding to the right half of the schematic diagram) of orientation C (IE = 2.0 mm).

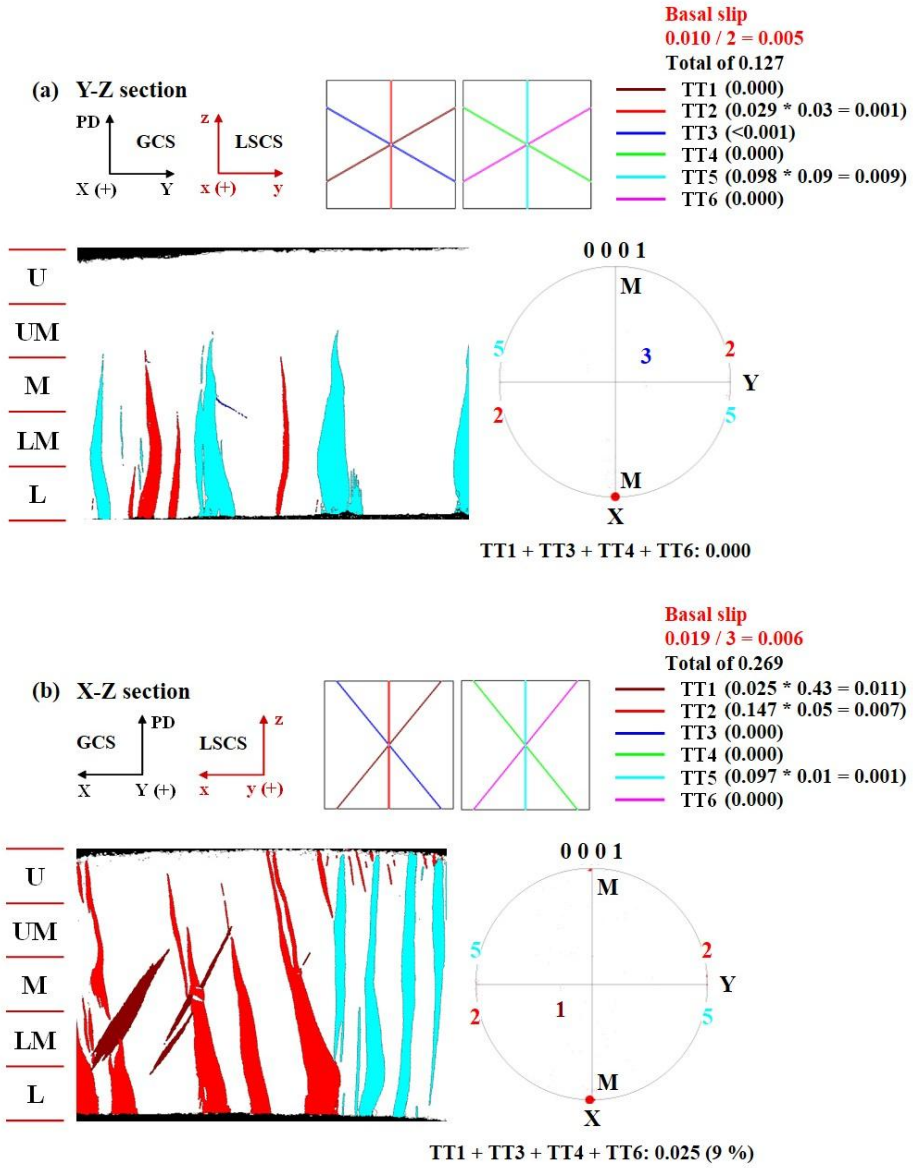

Figure 4.51 Twin analysis of RA in the (a) Y-Z and (b) X-Z sections of orientation C (IE = 2.0 mm).

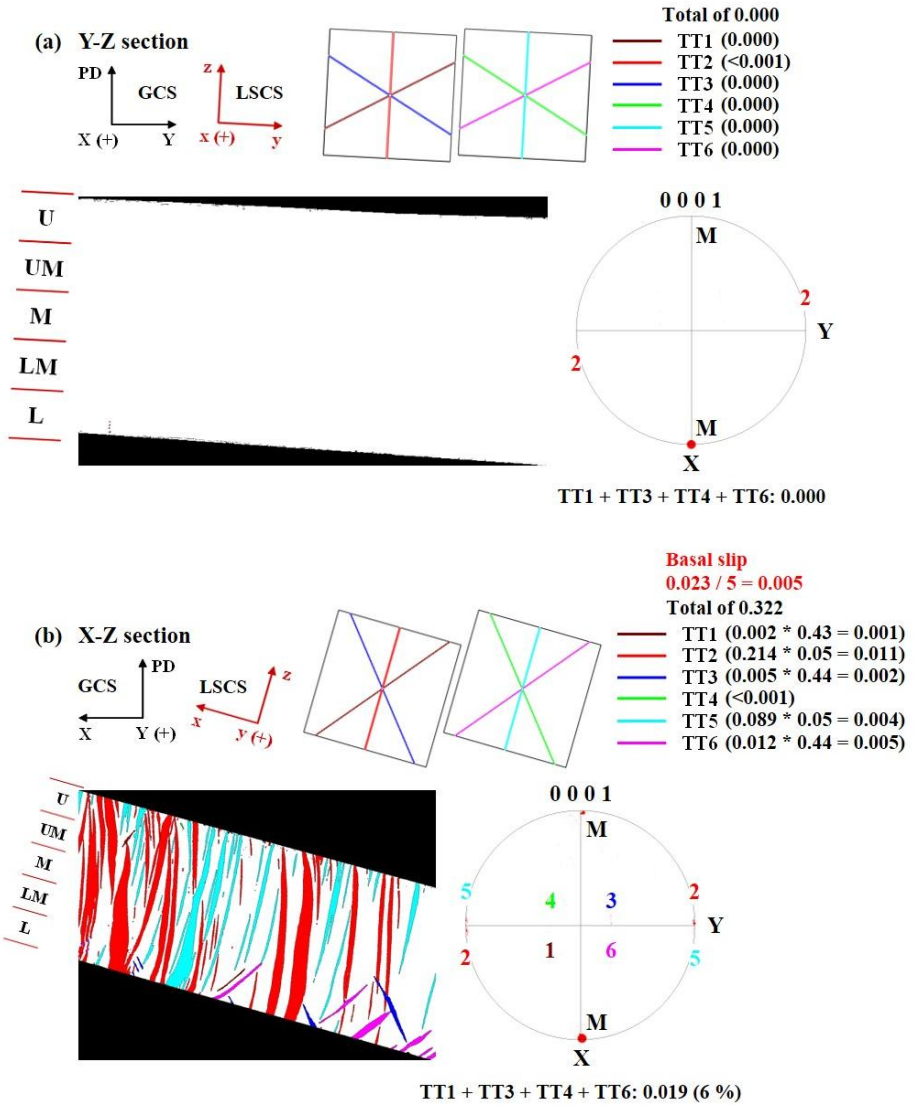

Figure 4.52 Twin analysis of RB1 in the (a) Y-Z and (b) X-Z sections of orientation C (IE = 2.0 mm).

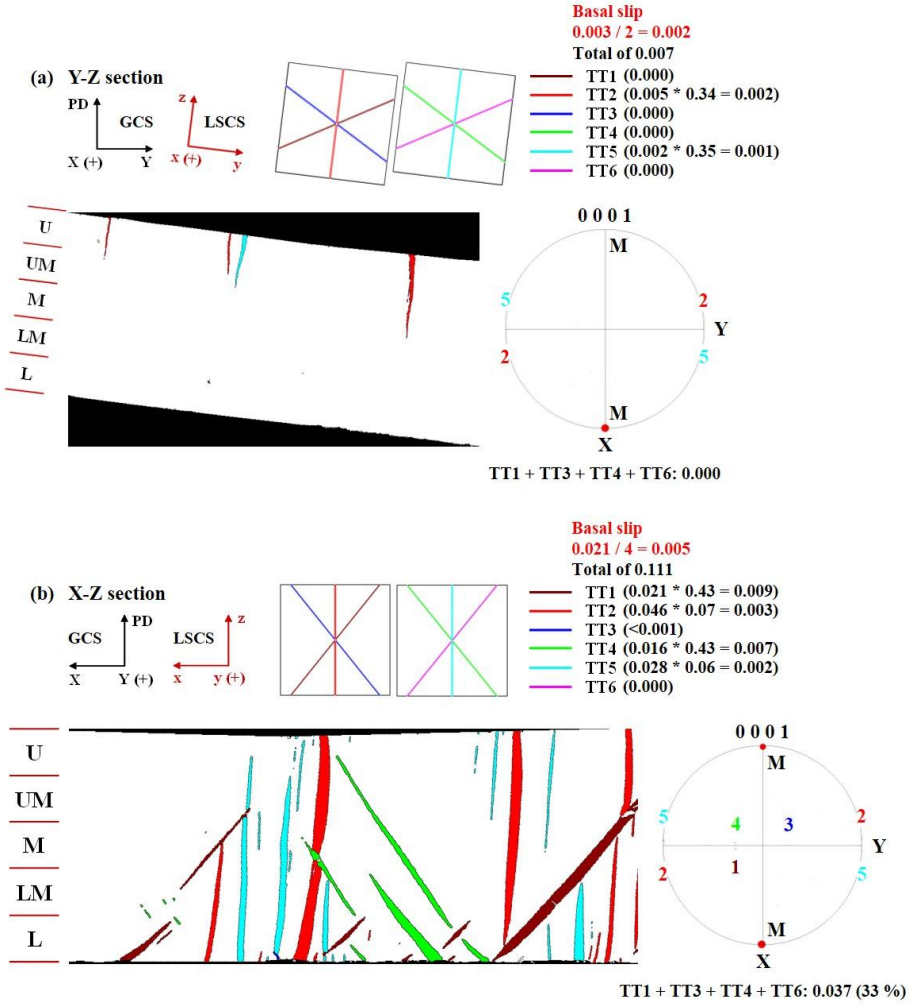

Figure 4.53 Twin analysis of RB2 in the (a) Y-Z and (b) X-Z sections of orientation C (IE = 2.0 mm).

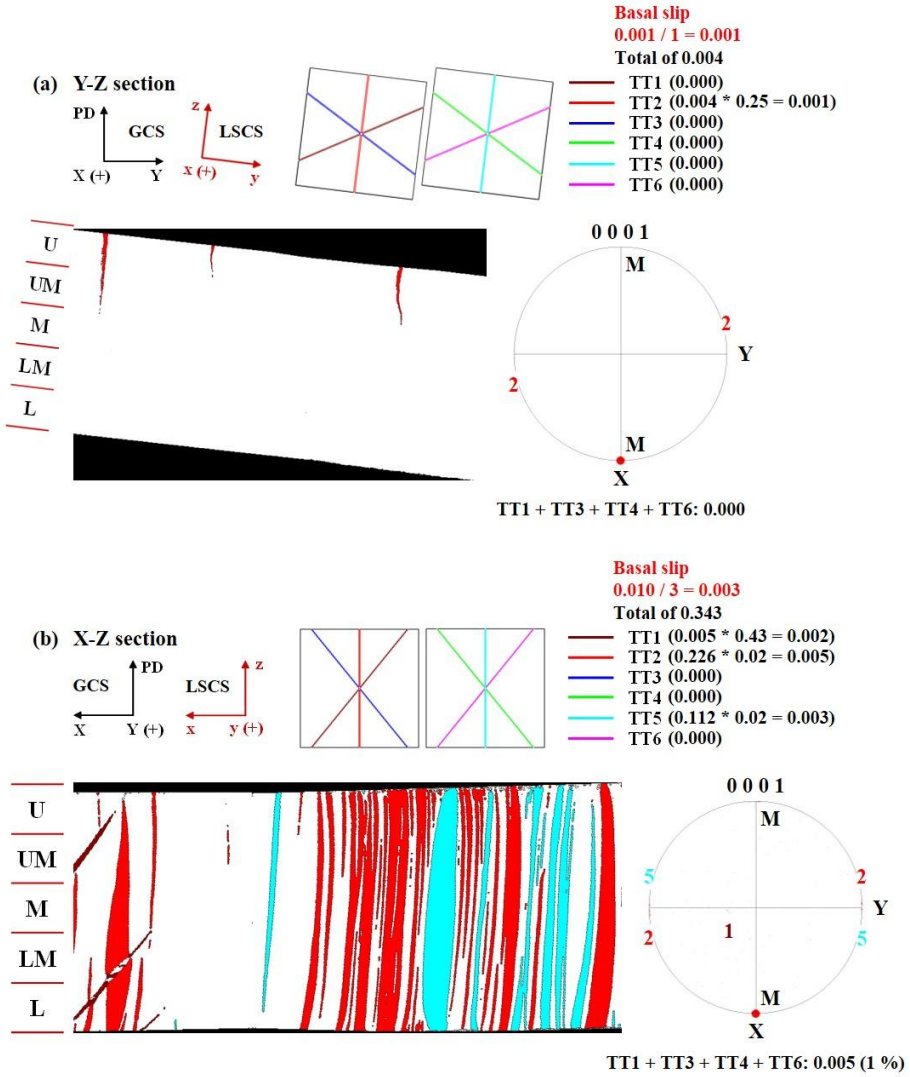

Figure 4.54 Twin analysis of RC1 in the (a) Y-Z and (b) X-Z sections of orientation C (IE = 2.0 mm).

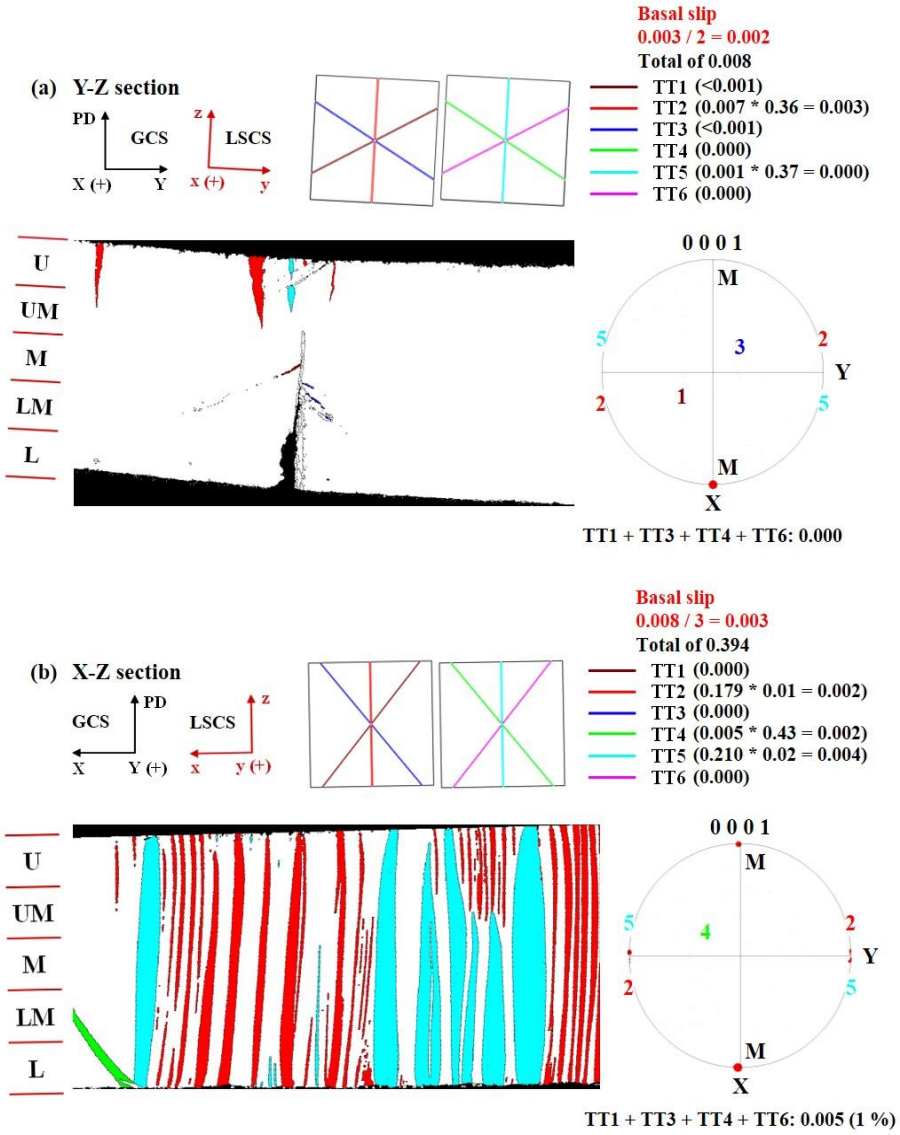

Figure 4.55 Twin analysis of RC2 in the (a) Y-Z and (b) X-Z sections of orientation C (IE = 2.0 mm).

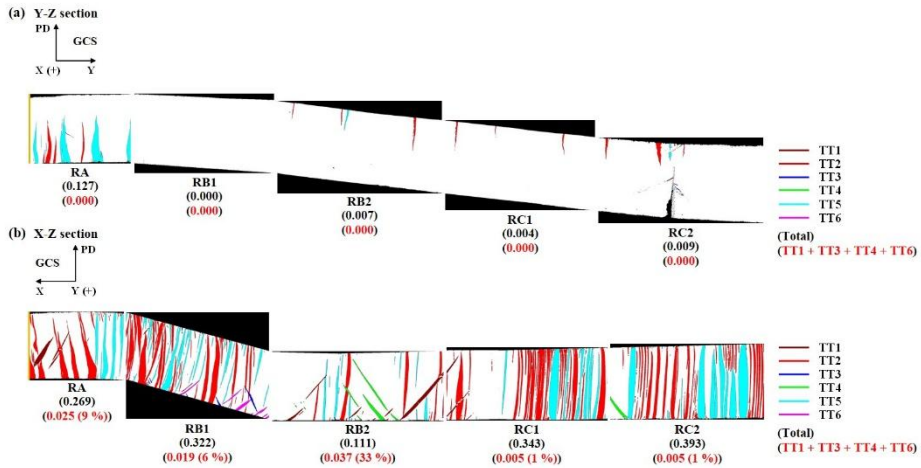

Figure 4.56 A comparison of the five subdivided regions in the (a) Y-Z and (b) X-Z sections of orientation C (IE = 2.0 mm).

Figure 4.57 shows the values for basal slip activation as a function of the five subdivided regions in the Y-Z and X-Z sections of both orientation B and orientation C. The result show that the values for basal slip activation of orientation B are higher than those for orientation C throughout the deformed specimen. Interestingly, orientation C exhibited the Erichsen value of 2.0 mm, even though there are a considerable number of tensile twins. The results show that only the rotation angle of 30° based on the c-axis caused the significant difference and this was attributed to the existence of tensile twins which assist in making favorable orientation for additional basal slip activation by crystallographic reorientation and consequently basal slip occurs along the reoriented directions, as shown in orientation B.

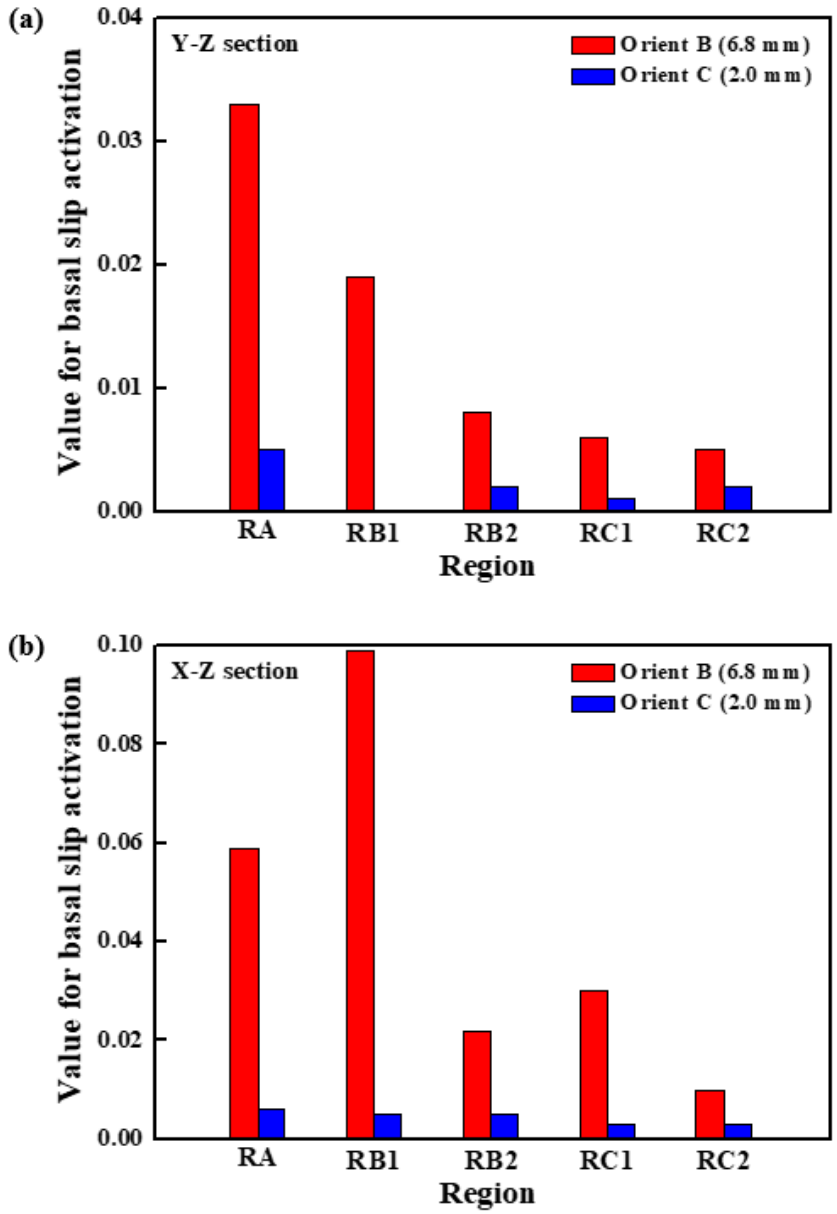

Figure 4.57 Values for basal slip activation as a function of the five subdivided regions in the (a) Y-Z and (b) X-Z sections of both orientation B (IE = 6.8 mm) and orientation C (IE = 2.0 mm).

4.5 Comparison

4.5.1 Room temperature vs. elevated temperature

The respective five subdivided regions in the X-Z section of three orientation conditions were compared in Figure 4.58. Unlike orientation A, it was found that a large amount of tensile twins was observed in both orientation B and C due to the geometry of their initial crystallographic orientations. Interestingly, the angle difference of prismatic planes by 30° based on the c-axis can cause a large difference with respect to the stretch formability at RT. In Figure 4.59, the spatial distribution for the bottom surface of three orientation conditions also depicts that the relative activities of tensile twins in both orientation B and C along X direction were higher than orientation A. However, the results in the present study exhibit that the tensile twins in orientation B, especially nucleated from the bottom surface of the deformed specimen inducing the activation of additional basal slip toward the newly oriented direction, are favorable for improving RT stretch formability, while those in orientation C are not. Therefore, orientation B can be defined as the twinning-induced soft orientation, while orientation C can be defined as twinning-induced hard orientation.

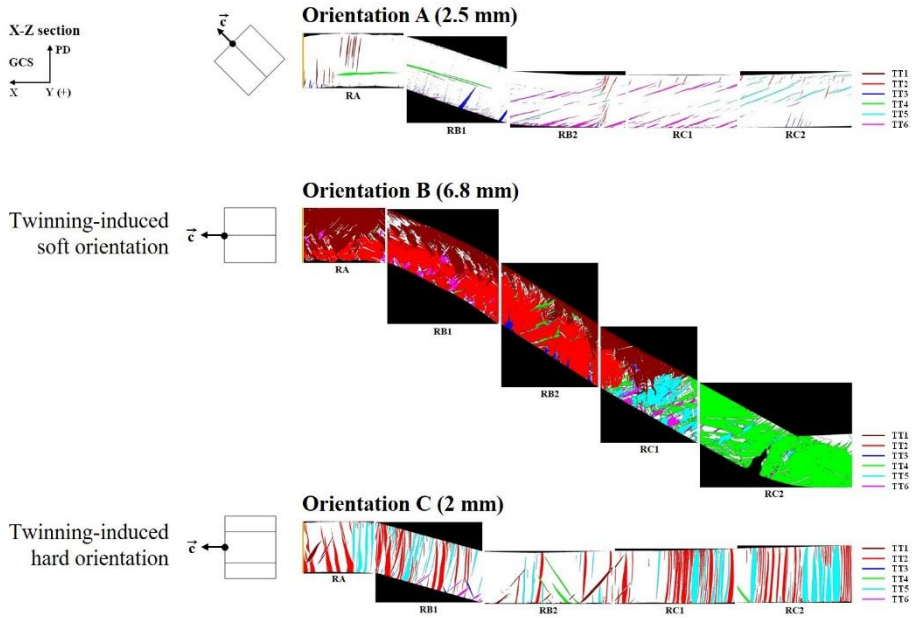

Figure 4.58 A comparison of the five subdivided regions in the X-Z section: (a) orientation A (IE = 2.5 mm), (b) orientation B (IE = 6.8 mm) and (c) orientation C (IE = 2.0 mm).

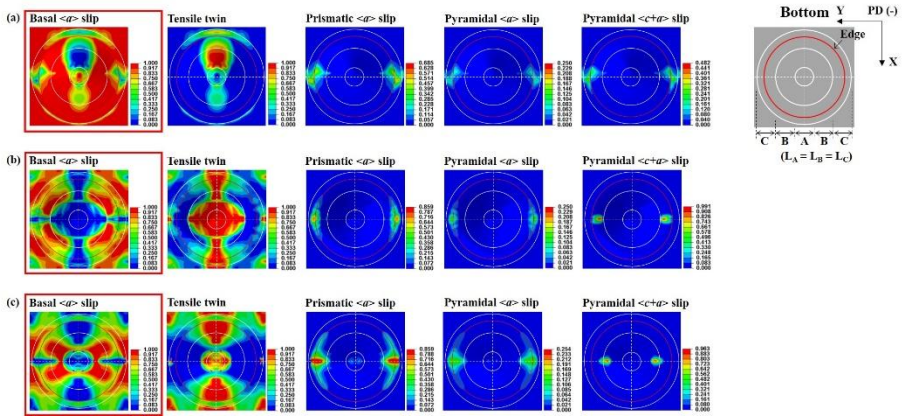

Figure 4.59 A comparison of the relative activities of deformation modes for the bottom-surface: spatial distribution of (a) orientation A (IE = 2.5 mm), (b) orientation B (IE = 6.8 mm) and (c) orientation C (IE = 2.0 mm).

Figure 4.60 exhibits the Erichsen test results for five representative crystallographic orientations at RT, 140°C and 220°C, respectively. The orientation conditions need to systematically distinguish as follows: Firstly, the crystallographic orientation A and B are considered based on the loading direction along <10$\bar{1}$0>. The condition of 45° between the loading direction and c-axis is denoted as orientation A. Likewise, the condition of 90° between the loading direction and c-axis is denoted as orientation B. Secondly, the crystallographic orientation C and D are considered based on the loading direction along <11$\bar{2}$0>. The condition of 90° between the loading direction and c-axis is denoted as orientation C. Likewise, the condition of 45° between the loading direction and c-axis is denoted as orientation D. Lastly, based on the loading direction along <0001>, the condition of 90° between the loading direction and c-axis is denoted as orientation E.

During the plastic deformation in Mg, the CRSSs of non-basal slip modes decrease with increasing temperature. Thermally activated non-basal slip modes compete with twinning and it results in diminishing twinning with increasing temperature, therefore, non-basal slip modes can easily activate at elevated temperature. Figure 4.61 shows the inverse pole figure maps and their pole figures in the X-Z section of orientation B at RT and 220°C. A comparison between RT and 220°C with respect to the relative activities of deformation modes the X-Z section of orientation B is also shown in Figure 4.62. It was found that the main deformation mode at RT was tensile twin, while the pyramidal $\langle \boldsymbol{c}+\boldsymbol{a} \rangle$ slip were mainly activated at 220°C. It is interesting to note that the Erichsen value of 6.8 mm at RT for orientation B is a considerable number to the other conditions, even the non-basal slip modes were activated at elevated temperatures.

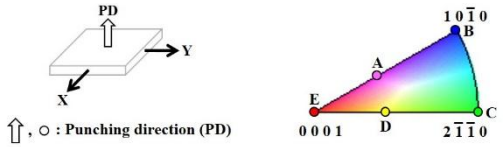

		A	B	C	D	E
Orientation						
PD section		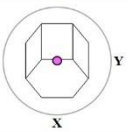	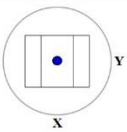	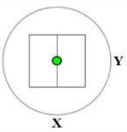	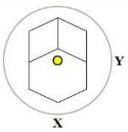	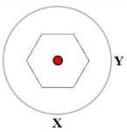
PD		[777 0 $\overline{777}$ 829]	[1 0 $\bar{1}$ 0]	[1 $\bar{2}$ 1 0]	[897 $\overline{449}$ $\overline{449}$ 829]	[0 0 0 1]
Angle between PD & c-axis		45°	90°	90°	45°	0°
IE (mm)	RT	2.5	6.8	2.0	1.9	1.5
	140°C	5.6	7.1	4.7	3.7	1.7
	220°C	7.7	7.7	8.0	7.9	2.9

Figure 4.60 Erichsen test results for five representative crystallographic orientations at RT, 140°C and 220°C, respectively.

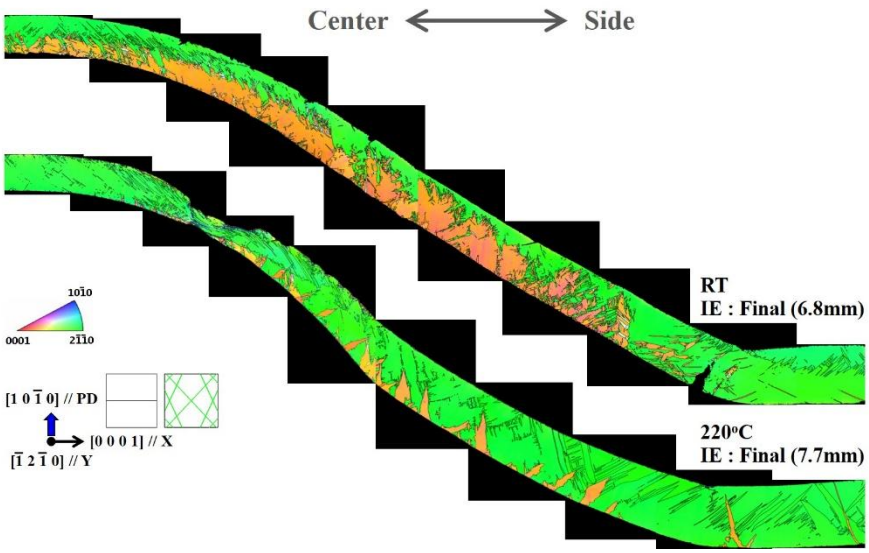

(a)

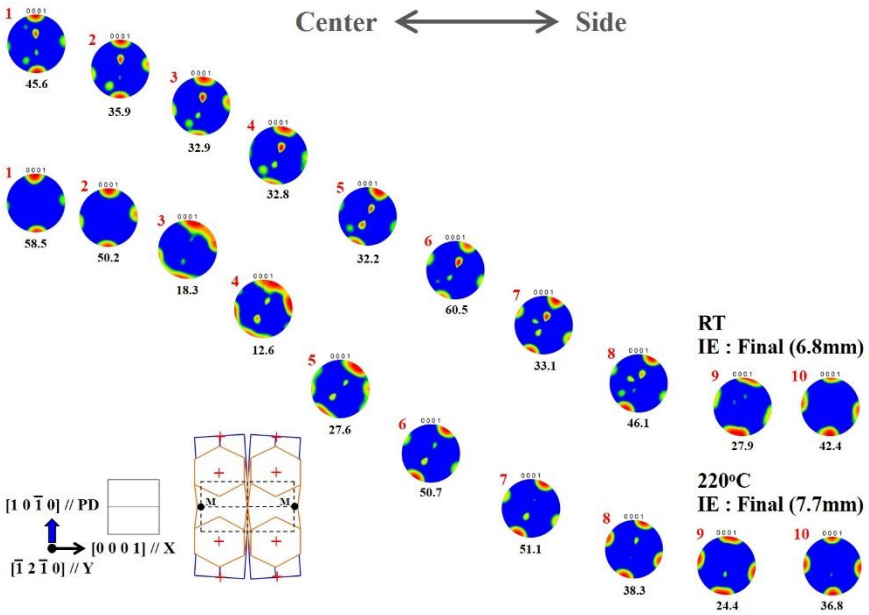

(b)

Figure 4.61 (a) Inverse pole figure maps and (b) their pole figures in the X-Z section of orientation B at RT (IE = 6.8 mm) and 220°C (IE = 7.7 mm).

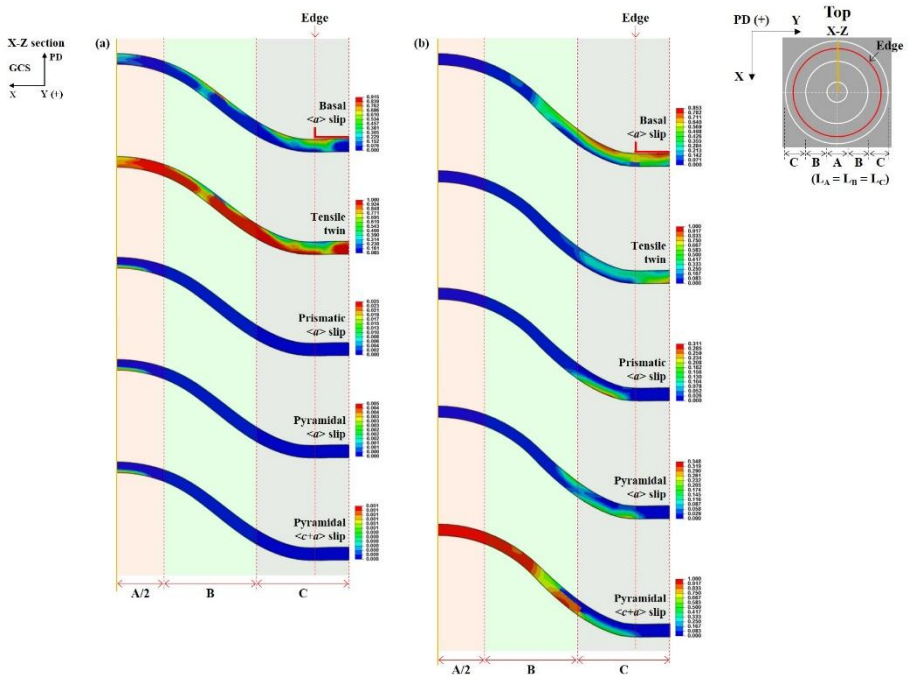

Figure 4.62 A comparison of the relative activities of deformation modes in the X-Z section of orientation B: (a) RT (IE = 6.8 mm) and (b) 220°C (IE = 7.7 mm).

4.5.2 Single crystal vs. poly crystal

An as-rolled AZ31 sheet with the thickness of 55 mm was used to in order to systematically examine the effect of initial texture on RT stretch formability in Mg poly crystal. The specimens for microstructure, texture measurement and tensile test were obtained at the mid-thickness of the 55t rolled AZ31 sheet. Figure 4.63(a) exhibits the representative microstructure of the plane parallel to the normal direction (ND) and the initial textures with three distinct angles of 0°, 45° and 90° with respect to the ND. Based on the three distinct initial textures, tensile test was conducted at room temperature with the initial strain rate of 1×10^{-4}/s.

Orientation F whose initial texture has the basal poles mostly parallel to the ND, similar to orientation E, can be typically obtained after rolling. Orientation G has the initial texture with the basal poles tilted about 45° from the ND to the rolling direction (RD), similar to orientation A and D. Due to the initial texture favorable for the basal slip activation, orientation G exhibited the highest elongation with the lowest yield and ultimate tensile strengths among the three orientations in Figure 4.63. Orientation H has the initial texture with the basal poles mostly parallel to the RD, similar to orientation B and C. The stress-strain curve of orientation H exhibited the relatively low yield strength but the highest ultimate tensile strength due to the significant work hardening, which was ascribed to the initial texture favorable for tensile twinning. Therefore, the highest n-value was achieved among the three conditions. Interestingly, the yield strength values in both orientation G and H are similar to each other. Moreover, the stress-strain curve of orientation G nearly corresponds to that of orientation H within the strain of 6% and still has the distinct work hardening. The results indicate that tensile

twinning can additionally occur to accommodate the strain during the tensile deformation.

Figure 4.63(b) shows the Erichsen values of AZ31 poly crystal for three representative initial textures at RT, 140°C and 220°C, respectively. The temperature conditions were the same as those for pure Mg single crystal. Due to the initial textures similar to the crystallographic orientations of single crystal, the Erichsen values for three initial textures of poly crystal are expected to have a similar tendency. Based on the single crystal study with respect to the orientation A, B, C, D and E, relatively high Erichsen value at RT is expected on orientation H by activating a large amount of tensile twins due to the geometry of its initial texture. However, unlike the result for orientation A and D for single crystal, orientation G exhibited the highest Erichsen value. The results imply that the dominant basal slip in combination with tensile twinning for strain accommodation is effective to improve RT stretch formability of AZ31 poly crystal.

Furthermore, the Erichsen values of orientation G and H at 220°C are close to 8.0 mm, which is similar to those of orientation A, B, C and D for single crystal. It was found that the Erichsen values among the eight orientation conditions in the present study, irrespective of whether the material is a poly crystal or not, cannot exceed 8.0 mm, even at the temperature of 220°C. Another interesting point to note is that the Erichsen values show that 6.8 mm in orientation B is a considerable number with respect to RT stretch formability by only controlling the initial crystallographic orientation of Mg single crystal. Further in-depth study will be conducted in the near future to fine out the mechanism with experimental evidence to understand the correlation between single crystal and poly crystal.

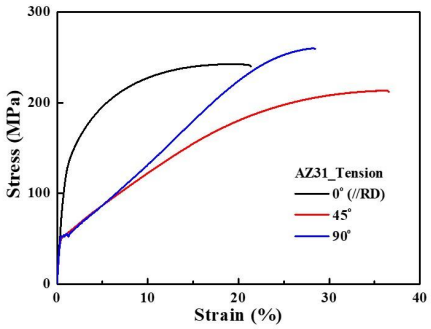

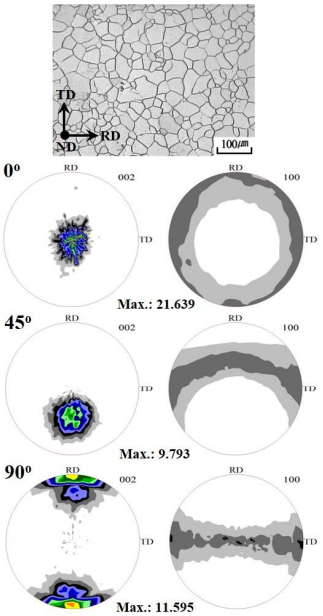

Orientation	Inclination of basal poles from ND	Y.S. (Mpa)	U.T.S. (Mpa)	El. (%)	Unif. El. (%)	S.H.E. (n)
F	0°	96.7	242.4	20.2	18.0	0.298
G	45°	49.6	213.1	35.5	35.1	0.553
H	90°	52.2	259.8	27.3	26.9	0.648

(a)

Orientation (Initial texture)		F	G	H
		Max.: 21.639	Max.: 9.793	Max.: 11.595
Inclination of basal poles from ND		0°	45°	90°
IE (mm)	RT	2.3	5.5	5.4
	140°C	3.4	6.9	6.5
	220°C	5.4	8.0	7.7

(b)

Figure 4.63 Experimental results of AZ31 poly crystal: (a) tensile properties with its microstructure and initial textures and (b) Erichsen values for three representative initial textures at RT, 140°C and 220°C, respectively.

4.6 Conclusion

In the present work, the influences of strain path on twinning behavior in Mg single crystal during Erichsen test have been investigated by experimental and theoretical approaches. The conclusions are summarized as follows:

1. Plastic anisotropy in Mg single crystal induces an anisotropically deformed dome shape along a certain direction during Erichsen testing.
2. The single crystal study and CPFEM result revealed that the heterogeneous twinning evolution throughout the deformed specimen is attributed to the non-uniform distribution of strain components due to geometric shape of the test equipment and anisotropic nature of the material itself.
3. Since the applied stress state in the Erichsen test at RT is found to be more complex compared to that in other plastic deformations, the crystallographic orientation favorable for the basal slip activation cannot guarantee the enhanced stretch formability.
4. The proper deformation in X-Z section was ascribed to the tensile twin variants induced by the compressive strain path, which provides a direction on how to improve RT stretch formability.
5. The results suggest that designing the texture favorable for activating tensile twins which can release the anisotropic nature of Mg is essential to enhanced stretch formability at RT.

Bibliography

[1] M.H. Yoo, S.R. Agnew, J.R. Morris, K.M. Ho, Non-basal slip systems in HCP metals and alloys: Source mechanisms, Mater. Sci. Eng. A. 319–321 (2001) 87–92. doi:10.1016/S0921-5093(01)01027-9.

[2] E.C. Burke, Plastic Deformation of Magnesium Single Crystals-Transactions AIME 194 (1952) 295-303.

[3] P. Taylor, F. Stohr, J.P. Poirier, Etude en microscopie electronique du glissement pyramidal { 1122 } 〈 1123 〉 dans le magnesium, (2006) 37–41.

[4] T. Obara, H. Yoshinga, S. Morozumi, {11$\bar{2}$2}〈1123〉 Slip system in magnesium, Acta Metall. 21 (1973) 845–853. doi:10.1016/0001-6160(73)90141-7.

[5] S. Ando, N. Harada, M. Tsushida, H. Kitahara, H. Tonda, Temperature Dependence of Deformation Behavior in Magnesium and Magnesium Alloy Single Crystals, Key Eng. Mater. 345–346 (2007) 101–104. doi:10.4028/www.scientific.net/KEM.345-346.101.

[6] M.H. Yoo, Slip, twinning, and fracture in hexagonal close-packed metals, Metall. Trans. A. 12 (1981) 409–418. doi:10.1007/BF02648537.

[7] J. Koike, Enhanced deformation mechanisms by anisotropic plasticity in polycrystalline Mg alloys at room temperature, Metall. Mater. Trans. A. 36 (2005) 1689–1696. doi:10.1007/s11661-005-0032-4.

[8] W.D. Robertson, I. Rosi, Additional modes, 5 (1957).

[9] P.G. Partridge, The Crystallography and Deformation Modes of HCP

Metals-Met Reviews 12 (1967) 169-194.

[10] S.H. Park, S.G. Hong, C.S. Lee, In-plane anisotropic deformation behavior of rolled Mg-3Al-1Zn alloy by initial {10-12} twins, Mater. Sci. Eng. A. 570 (2013) 149–163. doi:10.1016/j.msea.2013.01.071.

[11] Y. Chino, H. Iwasaki, M. Mabuchi, Stretch formability of AZ31 Mg alloy sheets at different testing temperatures, Mater. Sci. Eng. A. 466 (2007) 90–95. doi:10.1016/j.msea.2007.02.027.

[12] Y. Chino, M. Mabuchi, Enhanced stretch formability of Mg-Al-Zn alloy sheets rolled at high temperature (723 K), Scr. Mater. 60 (2009) 447–450. doi:10.1016/j.scriptamat.2008.11.029.

[13] Y. Chino, K. Kimura, M. Mabuchi, Deformation characteristics at room temperature under biaxial tensile stress in textured AZ31 Mg alloy sheets, Acta Mater. 57 (2009) 1476–1485. doi:10.1016/j.actamat.2008.11.033.

[14] B.C. Suh, M.S. Shim, K.S. Shin, N.J. Kim, Current issues in magnesium sheet alloys: Where do we go from here?, Scr. Mater. 84–85 (2014) 1–6. doi:10.1016/j.scriptamat.2014.04.017.

[15] D. Griffiths, Explaining texture weakening and improved formability in magnesium rare earth alloys, Mater. Sci. Technol. 31 (2015) 10–24. doi:10.1179/1743284714Y.0000000632.

[16] N.J. Kim, Critical Assessment 6: Magnesium sheet alloys: viable alternatives to steels?, Mater. Sci. Technol. 30 (2014) 1925–1928. doi:10.1179/1743284714Y.0000000596.

[17] J.W. Park, K.S. Shin, Improved stretch formability of AZ31 sheet via grain size control, Mater. Sci. Eng. A. 688 (2017) 56–61.

doi:10.1016/j.msea.2017.01.101.

[18] J. Singh, M.-S. Kim, S.-H. Choi, The effect of strain heterogeneity on the deformation and failure behaviors of E-form Mg alloy sheets during a mini-V-bending test, J. Alloys Compd. 708 (2017) 694–705. doi:10.1016/j.jallcom.2017.02.176.

[19] X. Huang, K. Suzuki, N. Saito, Textures and stretch formability of Mg-6Al-1Zn magnesium alloy sheets rolled at high temperatures up to 793 K, Scr. Mater. 60 (2009) 651–654. doi:10.1016/j.scriptamat.2008.12.035.

[20] B.-C. Suh, J.H. Kim, J.H. Hwang, M.-S. Shim, N.J. Kim, Twinning-mediated formability in Mg alloys, Sci. Rep. 6 (2016) 22364. doi:10.1038/srep22364.

[21] T. Zhou, Z. Yang, D. Hu, T. Feng, M. Yang, X. Zhai, Effect of the final rolling speeds on the stretch formability of AZ31 alloy sheet rolled at a high temperature, J. Alloys Compd. 650 (2015) 436–443. doi:10.1016/j.jallcom.2015.08.005.

[22] S.R. Agnew, J.F. Nie, Preface to the viewpoint set on: The current state of magnesium alloy science and technology, Scr. Mater. 63 (2010) 671–673. doi:10.1016/j.scriptamat.2010.06.029.

[23] X. Huang, K. Suzuki, M. Yuasa, Y. Chino, Effects of initial microstructure on the microstructural evolution and stretch formability of warm rolled Mg-3Al-1Zn alloy sheets, Mater. Sci. Eng. A. 587 (2013) 150–160. doi:10.1016/j.msea.2013.08.067.

[24] M.Z. Bian, Z.R. Zeng, S.W. Xu, S.M. Zhu, Y.M. Zhu, C.H.J. Davies, N. Birbilis, J.F. Nie, Improving Formability of Mg-Ca-Zr Sheet Alloy

by Microalloying of Zn, Adv. Eng. Mater. 18 (2016) 1763–1769. doi:10.1002/adem.201600293.

[25] H. Somekawa, A. Kinoshita, A. Kato, Great room temperature stretch formability of fine-grained Mg-Mn alloy, Mater. Sci. Eng. A. 697 (2017) 217–223. doi:10.1016/j.msea.2017.05.012.

[26] X. Huang, K. Suzuki, Y. Chino, M. Mabuchi, Texture and stretch formability of AZ61 and AM60 magnesium alloy sheets processed by higherature rolling, J. Alloys Compd. 632 (2015) 94–102. doi:10.1016/j.jallcom.2015.01.148.

[27] W. He, Q. Zeng, H. Yu, Y. Xin, B. Luan, Q. Liu, Improving the room temperature stretch formability of a Mg alloy thin sheet by pre-twinning, Mater. Sci. Eng. A. 655 (2016) 1–8. doi:10.1016/j.msea.2015.12.070.

[28] K. Hantzsche, J. Bohlen, J. Wendt, K.U. Kainer, S.B. Yi, D. Letzig, Effect of rare earth additions on microstructure and texture development of magnesium alloy sheets, Scr. Mater. 63 (2010) 725–730. doi:10.1016/j.scriptamat.2009.12.033.

[29] M.Z. Bian, T.T. Sasaki, B.C. Suh, T. Nakata, S. Kamado, K. Hono, A heat-treatable Mg–Al–Ca–Mn–Zn sheet alloy with good room temperature formability, Scr. Mater. 138 (2017) 151–155. doi:10.1016/j.scriptamat.2017.05.034.

[30] S.J. Park, H.C. Jung, K.S. Shin, Deformation behaviors of twin roll cast Mg-Zn-X-Ca alloys for enhanced room-temperature formability, Mater. Sci. Eng. A. 679 (2017) 329–339. doi:10.1016/j.msea.2016.10.046.

[31] D.H. Kang, D.W. Kim, S. Kim, G.T. Bae, K.H. Kim, N.J. Kim, Relationship between stretch formability and work-hardening capacity of twin-roll cast Mg alloys at room temperature, Scr. Mater. 61 (2009) 768–771. doi:10.1016/j.scriptamat.2009.06.026.

[32] T. Al-Samman, G. Gottstein, Room temperature formability of a magnesium AZ31 alloy: Examining the role of texture on the deformation mechanisms, Mater. Sci. Eng. A. 488 (2008) 406–414. doi:10.1016/j.msea.2007.11.056.

[33] A. Chapuis, J.H. Driver, Temperature dependency of slip and twinning in plane strain compressed magnesium single crystals, Acta Mater. 59 (2011) 1986–1994. doi:10.1016/j.actamat.2010.11.064.

[34] M.Z. Bian, K.S. Shin, {1012} Twinning Behavior in Magnesium Single Crystal, Met. Mater. Int. 19 (2013) 999–1004. doi:10.1007/s12540-013-5012-4.

[35] S.H. Park, S.G. Hong, C.S. Lee, Enhanced stretch formability of rolled Mg-3Al-1Zn alloy at room temperature by initial {10-12} twins, Mater. Sci. Eng. A. 578 (2013) 271–276. doi:10.1016/j.msea.2013.04.084.

[36] K.D. Molodov, T. Al-Samman, D.A. Molodov, On the diversity of the plastic response of magnesium in plane strain compression, Mater. Sci. Eng. A. 651 (2016) 63–68. doi:10.1016/j.msea.2015.10.108.

[37] K.D. Molodov, T. Al-Samman, D.A. Molodov, G. Gottstein, On the ductility of magnesium single crystals at ambient temperature, Metall. Mater. Trans. A Phys. Metall. Mater. Sci. 45 (2014) 3275–3281. doi:10.1007/s11661-013-2152-6.

[38] K.D. Molodov, T. Al-Samman, D.A. Molodov, G. Gottstein, On the

role of anomalous twinning in the plasticity of magnesium, Acta Mater. 103 (2016) 711–723. doi:10.1016/j.actamat.2015.10.043.

[39] K.D. Molodov, T. Al-Samman, D.A. Molodov, G. Gottstein, Mechanisms of exceptional ductility of magnesium single crystal during deformation at room temperature: Multiple twinning and dynamic recrystallization, Acta Mater. 76 (2014) 314–330. doi:10.1016/j.actamat.2014.04.066.

[40] K.D. Molodov, T. Al-Samman, D.A. Molodov, Deformation-Induced Recrystallization of Magnesium Single Crystals at Ambient Temperature, IOP Conf. Ser. Mater. Sci. Eng. 82 (2015) 12014. doi:10.1088/1757-899X/82/1/012014.

[41] D. Liu, R. Xin, L. Zhao, Y. Hu, Effect of textural variation and twinning activity on fracture behavior of friction stir welded AZ31 Mg alloy in bending tests, J. Alloys Compd. 693 (2017) 808–815. doi:10.1016/j.jallcom.2016.09.187.

[42] L. Wang, G. Huang, T. Han, E. Mostaed, F. Pan, M. Vedani, Effect of twinning and detwinning on the spring-back and shift of neutral layer in AZ31 magnesium alloy sheets during V-bend, Mater. Des. 68 (2015) 80–87. doi:10.1016/j.matdes.2014.12.017.

[43] M. Habibnejad-Korayem, M.K. Jain, R.K. Mishra, Microstructure modification and bendability improvement of AZ31 magnesium sheet by bending-unbending and annealing process, Mater. Sci. Eng. A. 648 (2015) 371–384. doi:10.1016/j.msea.2015.09.047.

[44] L. Jin, J. Dong, J. Sun, A.A. Luo, In-situ investigation on the microstructure evolution and plasticity of two magnesium alloys

during three-point bending, Int. J. Plast. 72 (2015) 218–232. doi:10.1016/j.ijplas.2015.05.010.

[45] D. Steglich, Y. Jeong, Texture-based forming limit prediction for Mg sheet alloys ZE10 and AZ31, Int. J. Mech. Sci. 117 (2016) 102–114. doi:10.1016/j.ijmecsci.2016.08.013.

[46] X. qing CAO, P. ping XU, Q. FAN, W. xian WANG, Theoretical prediction of forming limit diagram of AZ31 magnesium alloy sheet at warm temperatures, Trans. Nonferrous Met. Soc. China (English Ed. 26 (2016) 2426–2432. doi:10.1016/S1003-6326(16)64363-7.

[47] J. Min, J. Lin, J. Li, Forming limits of Mg alloy ZEK100 sheet in preform annealing process, Mater. Des. 53 (2014) 947–953. doi:10.1016/j.matdes.2013.07.082.

[48] G. Venkateswarlu, A.K. Singh, J. Davidson, G.R. Tagore, Effect of microstructure and texture on forming limits in friction stir processed AZ31B Mg alloy, J. Mater. Res. Technol. 2 (2013) 135–140. doi:10.1016/j.jmrt.2013.01.003.

[49] L. Wang, Q. Qiao, Y. Liu, X. Song, Formability of AZ31 Mg alloy sheets within medium temperatures, J. Magnes. Alloy. 1 (2013) 312–317. doi:10.1016/j.jma.2014.01.001.

[50] C. John Neil, S.R. Agnew, Crystal plasticity-based forming limit prediction for non-cubic metals: Application to Mg alloy AZ31B, Int. J. Plast. 25 (2009) 379–398. doi:10.1016/j.ijplas.2008.05.003.

[51] S.-H. Choi, D.H. Kim, S.S. Park, B.S. You, Simulation of stress concentration in Mg alloys using the crystal plasticity finite element method, Acta Mater. 58 (2010) 320–329.

doi:10.1016/j.actamat.2009.09.010.

[52] S.-H. Choi, D.H. Kim, H.W. Lee, E.J. Shin, Simulation of texture evolution and macroscopic properties in Mg alloys using the crystal plasticity finite element method, Mater. Sci. Eng. A. 527 (2010) 1151–1159. doi:10.1016/j.msea.2009.09.055.

[53] S.-H. Choi, D.W. Kim, B.S. Seong, A.D. Rollett, 3-D simulation of spatial stress distribution in an AZ31 Mg alloy sheet under in-plane compression, Int. J. Plast. 27 (2011) 1702–1720. doi:10.1016/j.ijplas.2011.05.014.

[54] S.-H. Choi, Simulation of stored energy and orientation gradients in cold-rolled interstitial free steels, Acta Mater. 51 (2003) 1775–1788. doi:10.1016/S1359-6454(02)00576-1.

[55] S.R. Kalidindi, C.A. Bronkhorst, L. Anand, Crystallographic texture evolution in bulk deformation processing of FCC metals, J. Mech. Phys. Solids. 40 (1992) 537–569. doi:10.1016/0022-5096(92)80003-9.

[56] C.N. Tomé, R.A. Lebensohn, U.F. Kocks, A model for texture development dominated by deformation twinning: Application to zirconium alloys, Acta Metall. Mater. 39 (1991) 2667–2680. doi:10.1016/0956-7151(91)90083-D.

[57] M. Lentz, M. Risse, N. Schaefer, W. Reimers, I.J. Beyerlein, Strength and ductility with {10-11}-{10-12} double twinning in a magnesium alloy, Nat. Commun. 7 (2016) 1–7. doi:10.1038/ncomms11068.

[58] J.W. Christian, S. Mahajant, DEFORMATION TWINNING, Prog. Mater. Sci. 39 (1995) 1–157.

[59] Y.F. Guo, S. Xu, X.Z. Tang, Y.S. Wang, S. Yip, Twinnability of hcp

metals at the nanoscale, J. Appl. Phys. 115 (2014) 224902. doi:10.1063/1.4881756.

[60] T. Tang, S. Kim, M.F. Horstemeyer, Molecular dynamics simulations of void growth and coalescence in single crystal magnesium, Acta Mater. 58 (2010) 4742–4759. doi:10.1016/j.actamat.2010.05.011.

[61] J. Wang, Q. Yu, Y. Jiang, I.J. Beyerlein, Twinning-associated boundaries in hexagonal close-packed metals, Jom. 66 (2014) 95–101. doi:10.1007/s11837-013-0803-0.

[62] J. Wang, I.J. Beyerlein, C.N. Tomé, An atomic and probabilistic perspective on twin nucleation in Mg, Scr. Mater. 63 (2010) 741–746. doi:10.1016/j.scriptamat.2010.01.047.

[63] C. Lou, J. Yu, L. Liu, Y. Ren, X. Zhang, {1 0 −1 2} twin nucleation induced by FIB micro-stress in magnesium single crystal, Mater. Lett. 210 (2018) 139–142. doi:10.1016/j.matlet.2017.09.031.

Acknowledgments

This Ph.D. project would not have been possible without the help of numerous individuals. First and foremost, I would like to thank my supervisor, Prof. Kwang-Seon Shin, for his many contributions to my life and for his unending patience with me when my progress wanted. He provided remarkable opportunities and supports as I pursued my Ph.D., and for this I will be ever grateful.

I am grateful to my dissertation committee: Prof. Heung-Nam Han, Prof. Nack-Joon Kim, and Dr. Kyung-Hoon Lee. They offered me so much advice, patiently supervising me. I want to express my gratitude but still do not know how I will ever repay them.

I would especially like to thank Prof. Shi-Hoon Choi. As my teacher and friendly mentor, he advised me more than I could ever give him credit for here. His endless support has enabled me to concentrate on my research and attain my Ph.D.

MML is the place where I have grown up as a researcher. I want to mention MML members. I will never forget their sincere support and precious memories with them. Our strong bond will go on for the rest of our lives.

I would also like to thank my teacher in high school, Sang-Gi Kim, for encouraging me all the way and making me what I am today. He has inspired me to do better in life. I will always remember what he has guided.

And finally, nobody has been more important to me during my studies than the members of my family. I would like to give my cordial appreciation to my parents, Sang-Jin Hyun & Kyung-Ja Lee, whose love and guidance are always with me in whatever I pursue. They are ultimate role models. I am also

greatly indebted to my brother, Gwang-Suk Hyun, for his endless support. I cannot imagine trying to accomplish such a task without them next to me. Therefore, I dedicate this thesis to my family.

February, 2018

Cheol-Seung Hyun